THE EFFECT OF THE CAST STRUCTURE ON THE EVOLUTION OF TEXTURE DURING PROCESSING OF AISI 433 FERRITIC STAINLESS STEEL

By

Mbavhalelo Maumela

Supervised by

Prof. C. W Siyasiya and Prof .W. E Stumpf

Dissertation submitted in partial fulfilment of the requirement for the degree

Master of Science: Applied Science (Metallurgy)

In the
Department of Materials Science and Metallurgical Engineering

Faculty of Engineering, Built Environment & Information Technology

University of Pretoria

Pretoria

Republic of South Africa

March 2017

Preface:

This dissertation is submitted for the degree of Master of Science at the University of Pretoria. The investigation was conducted under the supervision of Prof C.W. Siyasiya and Prof W.E. Stumpf in the department of Materials Science and Metallurgical Engineering at the University of Pretoria, South Africa.

The text contained herein is to the best of my knowledge, the result of my own work, except where acknowledgements and references have been made to previous work done by other researchers. Neither this nor a similar dissertation has been or is being submitted elsewhere for any other degree, diploma or other qualification.

Mbavhalelo Maumela.

Acknowledgements:

Foremost thanks and appreciation to Almighty God for being my steady anchor throughout my studies and life in general, and for still strengthening me.

I would like to extend my sincere gratitude to the following remarkable people:

- Prof W.E. Stumpf and Prof C.W. Siyasiya for the initiation of this project and their constructive advices, guidance, encouragement, life motivation, supervision and valuable inputs into this research project and making it possible to be published. I acquired profound technical and communication skills, professional practice from their experience and insight during this work, with that I thank you a lot.

- The personnel of Columbus Stainless Steel, especially Mr Dave Smith, for proposing this project, and for providing samples, technical and valuable data required for this project. I really appreciate your kindness, patience and understanding when I needed it most.

- Mintek's personnel, especially Dr Jones Papo for supervision and advices; the Human Resource Division's assistance with administrative work, and research and development support, especially Mr Dominic Monama; Advance Material Division (AMD) with laboratory facilities for metallographic work, with special reference to Mr Richard Coperthwaite and Mintek company for financial support and research facilities.

- Department of Materials Science and Metallurgical engineering especially Mrs Gabisille Ngema for assistance with department administrative work and IMMRI for laboratory facilities.

- University of Pretoria, in particular the Material Science and Metallurgical Engineering Department for the provision of facilities that made it possible for this project to see a light.

- Special thanks to my mother, Nndwamato Selinah Maumela, for unstinting efforts to ensure that I pursue, fulfil my dreams and aspirations.

- My siblings (Mpho, Shayi, Rofhiwa), family (brothers, sisters and cousins) and my partner Rofhiwa Muthige for their constructive support and words of encouragement.

- Finally, my colleagues and friends for words of encouragement and support. Much appreciated.

Synopsis:

Ferritic stainless steels (FSSs) are gaining popularity because they are cheaper than austenitic stainless steels (ASS) since they contain almost no nickel. Amongst these FSSs, there is a relatively new grade of steel designated AISI 433 i.e. 430 with added Aluminium (Al) and is produced by Columbus Stainless Steel in South Africa. However, these FSSs are inclined to develop surface-roughness defects during cold rolling or forming operations. The surface roughness defects manifest as series of ridges and valleys that run parallel to the former rolling direction (RD) and spread across the transverse direction (TD) of rolled steel sheet. These defects can be ridging or roping, depending on the type of surface defects. When a majority of ridges have a length of more than a millimetre along the RD as elements of surface roughness, the surface defects are known as ridging, but if they are shorter than a millimetre the term roping is used. The ridging or roping phenomenon is well known in FSS sheets and a lot of work has been done to improve resistance to their formation. The ridges, with a few micrometres amplitude, adversely affect the aesthetics and surface quality of the deep drawn components. The manufacturer is then obliged to perform time-consuming and costly processes such as grinding and polishing operations to remove the ridges in order to restore the smooth and shiny surface of the deep drawn articles. These further processes are objectionable to the manufacturers due to increased costs of production.

It has been shown that forming properties (ridging or roping resistance and formability) are anisotropic, governed by the crystallographic texture and topological arrangement of the preferred grain orientation when a sheet of steel is uniaxial tensile strained along the RD. The homogeneous γ-fibre texture components distribution promotes good forming properties, while heterogeneous texture components distribution with predominance of Cube, Goss and α-fibre components impairs these forming properties.

It is well established that an initial columnar cast structure (ICCS) promotes cube or α-fibre texture while an initial equiaxed cast structure (IECS), promotes γ-fibre texture components. If both structures are present, they promote inhomogeneous texture, which leads to roping or ridging. However, in this work, the cast structures were mechanically separated and processed separately but under the same conditions. This was done in order to see if the results would be different from mixed cast structures. As expected, it has been confirmed that IECS alone enhanced the γ-fibre texture and led to good surface roughness resistance while ICCS alone resulted in inhomogeneous texture components and impaired resistance to surface roughening. In other words, it was not the mixed as cast structure but the presence of columnar structure with cube texture that causes texture inhomogeneity in the final product that impairs resistance to surface roughening. Although at sub-micron level i.e. insignificant roughness, the surface roughness resistance of IECS sample was still better by 30% over an ICCS sample, i.e. the measured R_a-values were found to be 0.52±0.047 µm and 0.74±0.134 µm for IECS and ICCS respectively. The industrially processed FSS 430 with both structures, which was used as a benchmark, exhibited intermediate properties, i.e. the R_a-values were found to be 0.58±0.037 µm. No significant difference in yield strength, UTS and elongation were observed in this steel from both the IECS and ICCS steel strips.

Although the effect of Al addition on texture and surface roughness resistance in 433 was not part of this study, the results suggested that it may have a significant influence on texture and the subsequent surface roughness. It is well known that fine AlN particles promote selective growth of favourable (111)-oriented grains during hot rolling and annealing processes, resulting in strong γ-fibre texture components. Therefore, it was not surprising that there was insignificant difference in surface roughness resistance between ICCS and IECS in Al containing 433. This is recommended for further investigation.

Table of Contents:

List of Figures:

List of Tables:

List of Equations:

List of Abbreviations:

AOD	Argon oxygen decarburization.
ASS	Austenitic Stainless Steel.
BCC	Body centred cubic.
BCT	Body cubic tetragonal.
CSLs	Coincide site lattices
DSS	Duplex Stainless Steel
EAF	Electric arc furnace.
EBSD	Electron backscattering diffraction.
EMS	Electro-magnetic stirrer.
FCC	Face cubic centred.
FSS	Ferritic stainless steel.
GBCD	Grain boundary character distribution
HAGBs	High angle grain boundaries
HB	Hot band.
HBA	Intermediate hot band annealing.
HBA-CR	Hot band intermediate annealed and cold rolled.
HBA-CRA	Hot band intermediate annealed cold rolled and annealed.
HB-CR	Hot band cold rolled.
HB-CRA	Hot band cold rolled annealed.
ICCS	Initial columnar cast structures.
IECS	Initial equiaxed cast structures.
IPF	Inverse pole figures.
LAGBs	Low angle grain boundaries
M_f temperature	Martensite finish temperature.
M_s temperature	Martensite start temperature.
MSS	Martensitic stainless steel.
ND	Normal to the rolling plane.
ODFs	Orientation distribution functions.
OIM	Orientation image mapping.
P-value	Probability value.
RD	Rolling direction.
R_m value	Plastic strain ratio.
ΔR	Plastic anisotropy.
SB	Shear bands.
SEM	Scanning electron microscopy.
TD	Transverse to the rolling direction.
TF	Taylor factor.
XRD	X-ray powered diffraction.

List of Symbols:

γ-fibre	Gamma fibre texture.
α-fibre	Alpha fibre texture.
γ-Fe	Austenite phase.
α-Fe	Ferrite phase.
R_a	Arithmetic mean surface roughness.
$R_{mr(c)}$	Material proportion of the surface profile.
R_{zmax}	Maximum height of the roughness profile.
R_z	Surface roughness depth.
φ_1 , Φ, φ_2	Euler angles in Bunge definition.
ΔG_ε	Strain energy.
ΔG_v	Gibbs free energy per unit volume.
r^*	Critical radius for nucleus formation.
Q	Activation energy.
t	Time.
r_0	Initial average particle radius.
N	Nucleation rate.
N_T	Number of recrystallize textured nuclei.
N_R	Number of recrystallized random textured nuclei.
G_T	Growth rate of nuclei with texture.
G_R	Growth rate of nuclei without texture.
$I_{(hkl)}$	Diffraction intensity of hkl plane.
$G_{\gamma/\alpha}$	Interfacial surface energy per unit area between two phases.
ΔH	Enthalpy formation of new phase.
ΔT	Undercooling temperature.
ΔG^*	Activation energy for formation of new phase.
$\dot{\varepsilon}$	Strain rate.
R	Universal gas constant.
T	Temperature in degree Celsius.
σ_{ss}	Steady state flow stress of material during deformation.
n	Stress sensitivity.
A_1 and α	Material constants.
$\overline{\sigma_0}$	Uniaxial flow stress.
σ_0'	Plane strain flow stress.
Z	Holloman constant.
V	Total volume of sample.
s_n	Surface depth on RD-TD plane.

Chapter 1: Introduction

1.1. Introduction

1.1.1. Scope of the study

The focus of this investigation was the effect of solidification structures i.e. initial equiaxed cast structure (IECS) versus initial columnar cast structure (ICCS), on the evolution of the crystallographic texture during hot rolling, intermediate annealing, cold rolling and annealing processes vis-a-vis the surface roughness resistance and formability of AISI 433 FSS flat sheets. It is well known that as-cast equiaxed grain structure promotes the homogeneous γ-fibre texture in the final rolled and annealed steel sheets, which is good for drawability and surface roughness resistance in ferritic stainless steels (FSS) [1, 2]. In this work, the influence of the starting cast structure on the evolution of microstructure and crystallographic texture was examined separately and compared between IECS and ICCS in Al added 433 FSS.

1.1.2. Background of 433 FSS

The FSS types 433 (430 Al added), 439 and 434 are fairly newly developed grades of stainless steel. Demand for these types in engineering applications is increasing, especially for deep drawing during forming operations. Some applications of expensive ASS grades like 304 are mostly replaced by FSS grades. Therefore, their crystallographic texture after processing is important in forming properties of steel sheets. Hence, the need to understand the influence of as-cast grain structures (IECS versus ICCS) on the evolution of crystallographic texture in subsequent hot and cold rolling and annealing processes.

It is well known that FSS sheets are highly prone to develop ridging and roping during forming operations. The ridges may have an amplitude of up to 50 µm and may cover the entire width and are aligned parallel with the rolling direction (RD) of the sheets. If an article made from such steel sheet has a poor surface finish, it can be rejected in applications for exterior aesthetic reasons [3, 4]. Therefore, surface defects oblige manufacturers to engage in time-consuming and costly grinding and polishing operations to remove surface effects so that the surface quality of the formed article could be restored to the user's satisfaction.

The ridging formation in FSS sheets during metal forming operations has excited interest for decades. The significant role played by the crystallographic texture and topographic arrangement of preferred orientations in the formation of ridging is unanimously agreed upon. It has been noticed that when a heterogeneous texture distribution develops in this steel, such sheets are susceptible to ridging or roping [5, 6]. The heterogeneous texture distribution develops grain clusters of similar orientation, i.e. colonies that may be harder or softer than the matrix. When a principal tensile load is applied along the RD during metal forming operations, colonies that are {111}//ND oriented deform less along the TD than the matrix and result in ridge formation while {100}//ND oriented colonies deform more along the TD direction and form valleys or troughs, therefore ridging or roping [1, 7]. The FSSs are highly alloyed steels. Unlike low carbon steel, they undergo no or limited phase transformation during the thermo-mechanical processes that prevent randomisation of texture by the γ→α-phase transformation and that causes texture heterogeneity in the material [8, 9].

During hot rolling processes, columnar dendrites with an as-cast {001}<uv0> texture transform into elongated bands with sharp texture components, mainly components of a cubic or rotated-cubic texture i.e. {100}<010> or {100}<011> respectively. These bands become colonies during subsequent

cold rolling and final annealing recrystallization with different textures. These colonies or orientation clusters impair forming properties of FSS sheets during forming operations [1, 9].

1.2. Aim of the investigation

The aim of this project was to determine the effect of different starting as-cast grain structures (i.e. IECS versus ICCS) on the evolution of crystallographic texture during the subsequent hot rolling, cold working and annealing processes, and ultimately how the said evolution will affect the forming properties in 433 steel. The outcomes of this study would be used to justify mechanisms that enhance volume fraction of equiaxed structures in steel slab during casting stages of FSS, for example the installation of an Electro-Magnetic Stirrer at the continuous slab casting machine.

Chapter 2: Literature Review

2.1 The history of ferritic stainless steel

An acid resistant steel was first patented in Germany in 1912 by Krupp Engineers, namely Eduard Maurer and Benno Strauss. They found it was rust free amongst other steel scraps lying outside in a corrosive environment, see Fig.2.1.1 below. They took samples from the rust free steel scrap for analysis and discovered that it contained a large amount of the chromium element (Cr) [10, 11]. That was the beginning of the stainless steel journey, particularly ASS grades.

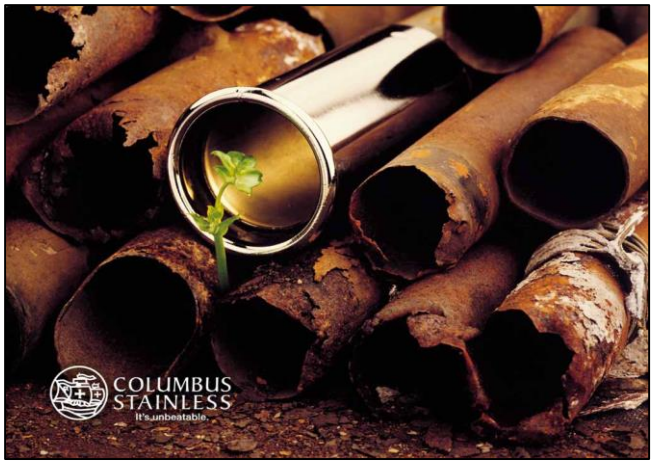

Figure 2.1.1: Steel pipes lying in corrosive environment and one pipe with high chromium which is rust free [12].

Harry Brearley [13, 14] who was born in Sheffield, England in 1871, first commercialised stainless steel in 1913 at Sheffield. He was the manager of the Brown Firth Research Laboratory in Sheffield and his task was to improve the corrosion resistance of steel gun barrels. He then decided to add an uncalculated amount of Cr (about 12%) to the steel. He noticed that this new steel was not etched under acidic conditions, nor did gun barrels made of it rust when left outside (exposed to the oxidising elements). This was the invention of martensitic stainless steel (MSS). The steel was hard, low in ductility and rust free. He recognised the commercial significance of this new MSS grade immediately. The MSS grade was used to manufacture cutlery, blades and other cutting items at the works in the Sheffield town. Unfortunately, the directors of Brearley's company refused to patent this rust-free steel as they did not see the advantage of rust-free knife blades because the knives still had to be washed. Brearley resigned and joined a North American steel producing company in 1915 [15].

Around the same time, Elwood Haynes [15] had also independently invented 12% Cr rust-free steel in the United State of America (USA), but his application for a patent was turned down because of Brearley's patent. However, at the end, Haynes resolved the dispute with Brearley by setting up a company with him, called the American Stainless Steel Company. The company's vision at first was to "promote the knowledge and the use of stainless steel worldwide". The USA took the lead in developing new applications for stainless steels under the American Iron and Steel Institute (AISI).

The development of stainless steel was not fully understood until 1920 when Krupp announced its 1912 patent of ASS to the world. FSS had meanwhile been developed and the duplex stainless steels (dual phase of austenitic and ferritic phases as single matrix phase alloy) were first developed in the 1930s.The duplex stainless steels (DSS) combine the low cost of the FSS properties with the toughness and weldability of the ASS. However, they were not commonly recognised until improved steelmaking

techniques became available in the 1960s. DSS and FSS grades could then be produced cost-effectively with the desired low carbon (C) content and good properties [11].

Several years later, in 1977, the utility FSS grades were invented with minute amounts of nickel (Ni) added as an alloying element in South Africa by Middelburg Steel and Alloys Corporation, now called Columbus Stainless Steel. Columbus Stainless (Pty) Ltd is one of major producer of stainless steel flat products in the African continent. It is based in South Africa in Middelburg, Mpumalanga province. Columbus ships its flat products far and wide across the globe [12].

The development of stainless steel products over the past 100 years has been truly astonishing [15]. Today, the stainless steel family are:

- Ferritic : formable steel
- Austenitic : expensive due to high Ni content but has good weldability and forming : properties
- Duplex : dual (ferritic and austenitic) phase alloy
- Martensitic : containing high C content for hardness

These stainless steels are in service across the globe and their applications are increasingly diverse. In stainless steel, Cr is the primary element that makes the steel "stainless", giving it remarkable corrosion and high temperature oxidation resistance. Cr is readily available and easily recycled as stainless steel scrap, posing no threat to the environment. Ni, another primary element of ASS grade, is subject to price fluctuations, due to stock market factors. This impacts the cost of ASS grades significantly but they have good properties for many applications today. ASS is the currently world's highest consumed grade of all stainless steels. FSS, the second most consumed family of stainless steels after ASS grades, contains small amounts of Ni and is, thereafter, cheaper to produce than ASS grades.

2.2. Classification of stainless steels and the role of alloying elements

Stainless steel is called "stainless" because of its stain-free surface property, which it acquires from the formation of an inert oxide (Cr_2O_3) layer with thickness ranging between 2-3 nm [13, 14]. This layer develops under corrosive oxidising standard atmospheric conditions of oxygen (O_2) which oxidises Cr in the steel. The layer acts as a diffusion barrier between the corrosive environment and the fresh metal underneath to prevent further corrosion. The passive layer is self-healing; any damage by abrasion or scratching is healed immediately by a re-passivation reaction process [14]. The layer contains copious amounts of Cr, at least 11.0% to give it its corrosion resistant property.

Apart from Cr, other alloying elements are added to strengthen and bestow the sought-after quality of stainless steel. The alloying elements are: nickel (Ni), molybdenum (Mo), titanium (Ti), copper (Cu), niobium (Nb), aluminium (Al) and silicon (Si), with mainly the following non-metal alloying elements also added: carbon (C), nitrogen (N) and boron (B) interstitial alloying elements. They improve steel properties such as formability, extreme temperature strength and oxidation resistance, cryogenic toughness, creep strength, wear resistance, pitting corrosion resistance, and other properties.

The alloying elements play an important role in the phase transformation during the solidification of a stainless steel melt. The Ni, which is an austenite (γ) former, enlarges the γ-phase region during solidification. The volume fraction of γ-phase depends on the amount of phase-stabiliser content of the steel. It can be retained from higher temperatures down to room temperature. The Mo, Ti and Nb, which are ferrite (α) phase formers, enhance the formation of the α-phase matrix of the stainless

steel [11, 13]. Duplex stainless steels have a matrix made of γ- and α-phases while martensitic (BCT) stainless steel contains the martensite matrix phase. Fig.2.2.2 shows stainless steels classification based on the alloying elements added to Fe-Cr-Ni base alloys.

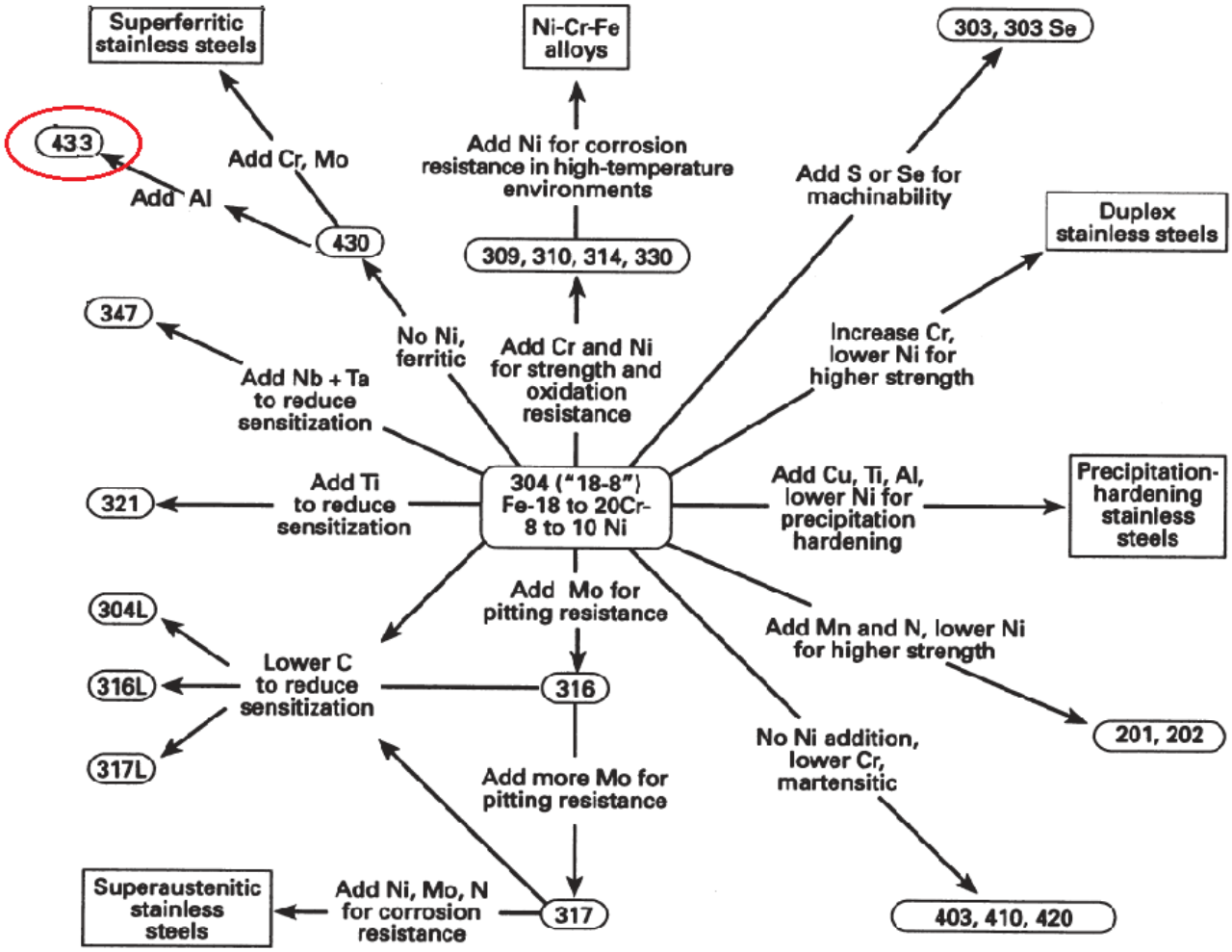

Figure 2.2.2: Classification of stainless steel grades based on the addition of alloying elements [11].

C addition increases the strength of stainless steels at elevated temperatures while N gives strength and toughness for cryogenic applications. Careful additions of these interstitial elements must be made because excessive addition of C and N can decrease corrosion resistance of the alloy by forming Cr carbides and nitrides, thus leading to Cr depletion in the microstructure, which reduces corrosion resistance, particularly adjacent to the grain boundaries, a phenomenon called sensitization [16].

Fracture strength and pitting corrosion resistance are obtained by careful addition of N. If added in excess, N will not only reduce corrosion resistance but can also develop strain aging during cold forming because of nitrogen's ability to diffuse fast through the matrix towards dislocations and immobilise them at room temperature[17]. This is called the Cottrell or strain ageing effect.

However, the primary requirement for stainless steels is corrosion resistance for all applications. The selection of a particular grade of stainless steel must meet the standard for corrosion resistance first and foremost, in preference to improved mechanical and physical properties. All properties are considered in relation to their contribution to achievement of the overall service performance requirements. The range of stainless steel grades varies progressively with levels of corrosion resistance and mechanical properties, each offering specific attributes in respect of their ability to withstand corrosion under varying environmental conditions. The available grades of stainless steel

can be classified into five basic families: ferritic, austenitic, martensitic, duplex and stainless steels that allow precipitation hardening.

2.2.1. Ferritic stainless steel grades

FSS grades are "body-centred-cubic" (bcc) crystal structure as matrix at room temperature. They are designated the 400 series by the American Iron and Steel Institute (AISI). This family of stainless steels made of binary Fe-Cr alloys containing Cr ranging from 12% to 30%. The C content is kept well below 0.08%C and permitting limited strength of the alloy. FSSs are not hardenable (ability to form martensite as it cools) by heat treatment and have annealed yield strengths ($R_{p0.2}$) ranging between 275 to 350 MPa. They are ferro-magnetic and their excellent corrosion resistance depends on their Cr and Mo content [18, 19].

During the continuous casting process of FSS materials, by having at least 12% Cr and other micro alloying elements, are formed from the liquid solidifies to an α-ferrite phase and have limitations to undergo γ→α-phase transformation during hot rolling. If any stainless steels are heat-treated or used in the temperature range 350-550 °C, a serious decrease in toughness will be observed after shorter or longer times of application. The phenomenon is encountered in alloys containing 15-75%Cr, i.e. including FSS material. The origin of this embrittlement is the spinodal decomposition of the matrix into two phases of bcc, namely σ and (σ´+σ) phases. The σ-phase is very rich in iron (Fe) and the (σ´+σ) is very rich in Cr. This type of embrittlement is called 475°C embrittlement. However, it can be healed by heating the steel at temperatures above 600°C and quenching to room temperature [13]. The FSS grades are designed based on the phase diagram given in Fig.2.2.3 below.

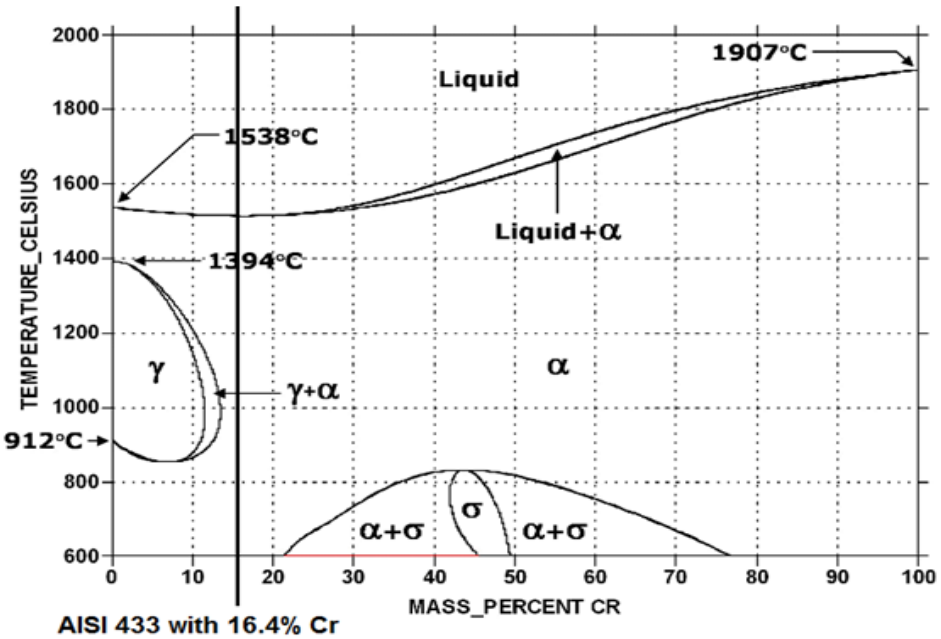

Figure 2.2.3: Fe-Cr equilibrium phase diagram, vertical line shows where the 433 FSS lies [11].

It's not only Cr addition which plays a significant role of stabilizing the α-phase region, but also by lowering interstitial alloying elements such as B, C and N which are all austenite formers. Lowered interstitial elements constrict the γ-phase loop together with the dual phase (γ+ α) region while widening the α-phase region. Fig. 2.2.4 below shows the effects of different alloying elements on the γ-phase region. From Fig.2.2.4, some alloying elements expand while other constrict this region of the γ-phase.

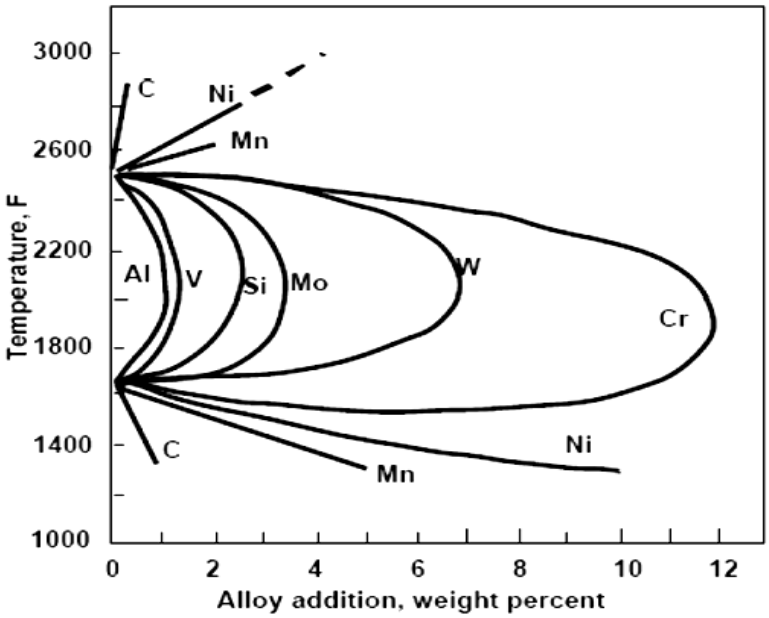

Figure 2.2.4: Effect of alloying elements on the Fe-C phase diagram, especially the γ-loop [20].

Some of the FSS grades are stabilized to avoid intra-granular corrosion. Stabilization is achieved by adding alloying elements that have a high affinity for interstitial elements such as C and N and inhibit precipitation of carbides and nitrides. When interstitial elements are tied up by stabilizing elements, such as Nb or Ti, corrosion resistance is increased. However, when interstitial elements react with Cr to form chromium carbides (Cr_3C_2, Cr_2C_7or $M_{23}C_6$), corrosion resistance is deceased [11]. These precipitates prefer to form at grain boundaries, depleting the Cr amount adjacent to the grain boundaries, resulting an inter-granular corrosion. The FSS 433 is stabilized by Al to tie up N and form AlN and not chromium nitrides. The C amount is in a very low concentration for the precipitation of Cr carbides, hence C stabilization is unnecessary in 433 FSS [21].

The main disadvantages of the FSS are [13]:

- They have poor to fair cryogenic properties,
- Limited formability,
- Fair high temperature properties,
- They are prone to surface defects such as ridging or roping during metal forming operations which renders formed articles with poor surface quality,
- Limited weldability, i.e. they exhibit rapid grain growth and sensitization in sections greater than 3 mm in thickness, which impair weld metal and heat affect zone (HAZ) tensile and fatigue strengths, and toughness properties. A FSS material cannot be used in dynamic or impact loading structures in an as-weld condition if compared to ASS.

2.3. Processing of stainless steels

Stainless steel flat products are produced by using a simplified typical conventional system layout as illustrated in Fig. 2.3.1 below.

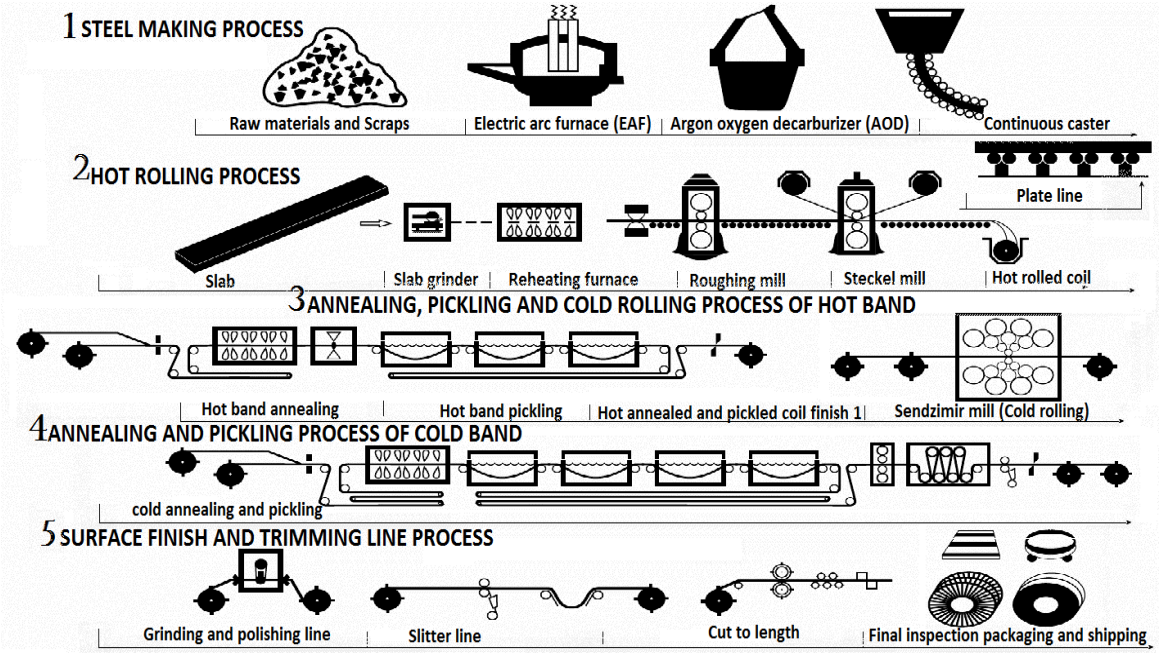

Figure 2.3.1: Typical process flow diagram of stainless steel sheets or strips [22].

The plant system comprises the following typical processes, namely:

- Steel making process.
- Hot rolling process, composed of Roughing and Steckel mills.
- Hot band annealing, pickling and cold rolling process.
- Annealing and pickling of cold band process.
- Surface finishing and trimming line processes where surface finish, trimming into customer's specified dimensions, coiling of strip, labelling and packaging are done.

2.3.1. Steelmaking process

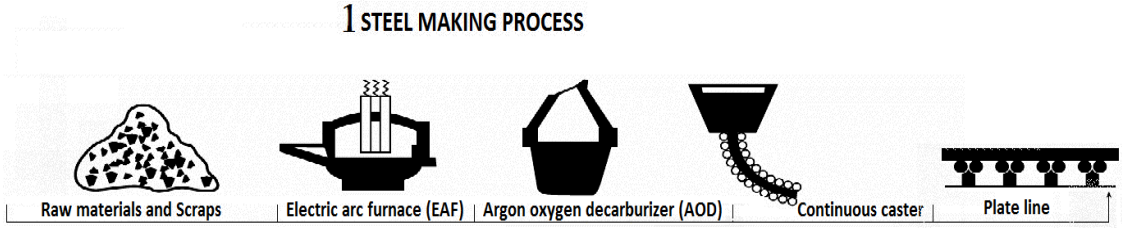

Figure 2.3.2: Typical steel making process of stainless steel.

In the steelmaking process, a carefully calculated mass of raw materials (Fe-Cr pellets) is mixed with metal scrap, reducing agents and fluxes in order to form a desired liquid alloy composition. The composition of the alloy governs the steel's properties right up to the final steel flat product. After mass balance, the raw materials are poured into an Electric Arc Furnace (EAF) where energy is delivered to melt the raw materials. Electrical energy in the form of a current is delivered by graphite electrodes to form a melting electric arc and supplies enough heat to melt raw materials and liquefies metals at temperatures above 1400°C

The liquid stainless steel is then poured into an Argon-Oxygen De-carburizer (AOD) vessel for refinery or alloying element adjustments, purification (removal of impurities), reduction of oxidation metallic compounds, desulphurisation and decarburization (lowering C content to the desired amount). In the AOD vessel, oxygen, argon (Ar) and nitrogen gases are blown strongly into the stainless steel liquid to remove impurities as they rise to the liquid surface where they will be entrapped by slag (molten flux). The C content can be lowered down to 0.02% in the liquid alloy, depending on the grade to be produced. Micro-alloying elements are also added and balanced at this stage for desired properties.

The refined molten metal is then conveyed by a ladle into a tundish, then poured into a continuous casting mould through a bifurcated submerged entry nozzle (SEN) for continuous casting, then cast into solid steel slabs. During the casting stage the temperature is careful controlled, especially the cooling rate, which is based on the phases and size of grain structures that need to be achieved at room temperature. After continuous casting, the slabs will have a typical width of 900 mm to 1600 mm, a thickness of about 200 mm, and a length from 4m to a maximum of 12m. Surface grinding is applied to remove any possible surface defects before the slab is taken to the hot rolling stage. The surface finishing and trimming preparation of slabs or plates that is required as saleable semi-finished products can be done just after casting. The surface finish preparation of slab is done under the “plate-line” stage [22].

2.3.2. Hot rolling process

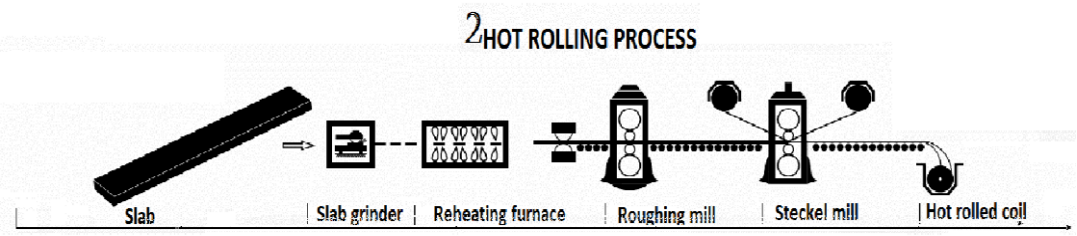

Figure 2.3.3: Typical steel reverse hot rolling mill for stainless steel.

The hot rolling process begins at the slab grinder where the surface is further cleaned by removing solidified flux scales from the slab’s surface that were formed just after the continuous casting stage. The cleaning is done to ensure that the slab’s surfaces are free from defects before being passed into the walking-beam reheating furnace where the slabs are heated up to temperature ranges between 1100°C and 1300°C, depending on the stainless steel grade. However, for 433 grade, the homogenisation temperature is 1200°C. The temperature of the whole slab has to be uniform throughout the cross section of the slab after a given soaking time. The reheating of the steel slab is done before being rolled to the desired thickness through the roughing and Steckel mills [22].

The slab’s surfaces are then blasted with high pressure water to remove scale formed while it was inside the walking beam furnace. It is hot rolled on a reversing four high mill stand known as a roughing mill. The seven passes are done to achieve thicknesses between 65 mm and 25 mm.

Thinner gauges are achieved by further hot rolling in a reverse four high mill stand known as a Steckel mill. Five passes are done to achieve a thickness ranging from 25 to 2.5 mm thickness within finishing exit temperatures ranging from 750 to 850 °C before it is water spray cooled. Once the predetermined gauge is reached, the material can either be coiled (black coil, also known as hot band) by a down coiler device or cut into plate (black plate) by a shear and stacker device. If the plate thickness is above 15 mm it can be cut using plasma cutters [15]. The flat products after hot rolling can be processed further as plate finish product. If the black coil or plate is not required as product, then the steel is taken to the cold rolling stage for the production of thin sheets or strips.

2.3.3. Hot band annealing, pickling and cold rolling process

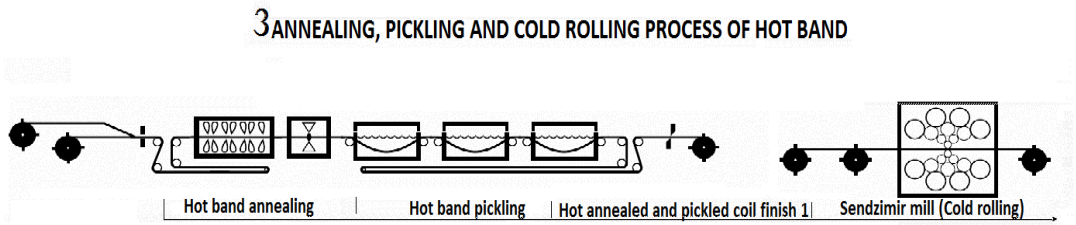

Figure 2.3.4: Typical hot band annealing process for stainless steel.

The hot band process begins at the batch annealing furnace where the hot rolled products are heated up to the recrystallization temperature, normally about 0.7($T_{melting\ point}$). At this recrystallization temperature, the workpiece is kept at that temperature for a calculated time to soften (anneal) the microstructures and restore ductility. After annealing, the strip is descaled by shot blasting and then pickled and passivated with acid. The passivation is applied to restore the stainless surface appearance of the workpiece. This product has a dull surface finish.

The cold rolling process takes place at a Sendzimir mill (Z-mill) which is a reversing 20 high cluster mill stand -see Fig. 2.3.5 below. It produces a smooth, shiny finished, cold rolled stainless steel. The hot band strips of 433 FSS grade are normally given a typical 62 % thickness reduction so that a thinner gauge is achieved with a smooth and shiny surface. The final gauge ranges between 0.2 mm to 6.0 mm [23].

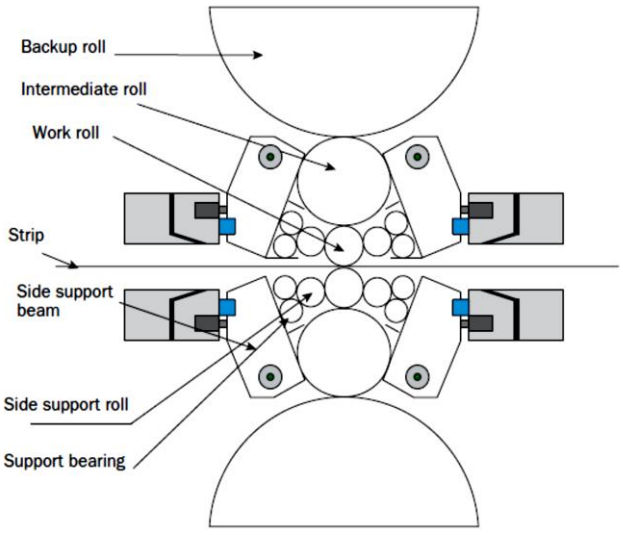

Figure 2.3.5: Typical schematic interior diagram of cluster mill (Sendzimir mill) for cold rolling stainless steel [24].

The Sendzimir mill which is an often used stainless cold rolling mill, reduces the thickness of the steel from an incoming range of 3 mm to 8 mm to a final thickness of 0.25 mm to 6 mm. The working rolls can attain a product high speed of 800m/min and the mill is computer controlled to produce the precise shape and thickness throughout the cross section of the sheet [23].

2.3.4. Annealing and pickling process of cold band

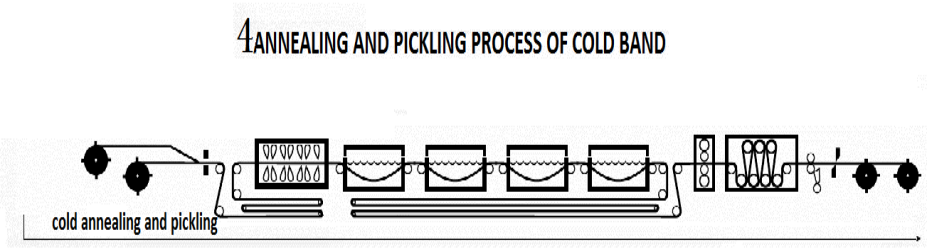

Figure 2.3.6: Typical annealing and pickling process of cold band stainless steel.

After cold rolling, the material is then annealed and descaled electrolytically, pickled and passivated to reform the passive surface layer (Cr_2O_3). A decontamination treatment removes organic metallic residues while the passivation process involves immersion of the strip in a cold 20-25% NHO_3 dilute acid bath for a few minutes to restore the passive layer. Thereafter, the material is then processed through a skin-pass rolling mill to ensure a brighter surface finish [23]. The cold rolled material, if required, can be processed through a vertical bright annealing (VBA) furnace. In the VBA, the strip is firmly gripped by thick wool at the bottom and top surface ends in order to avoid any oxidative atmosphere entering the inert atmosphere chamber.

2.3.5. Surface finishing and trimming line process

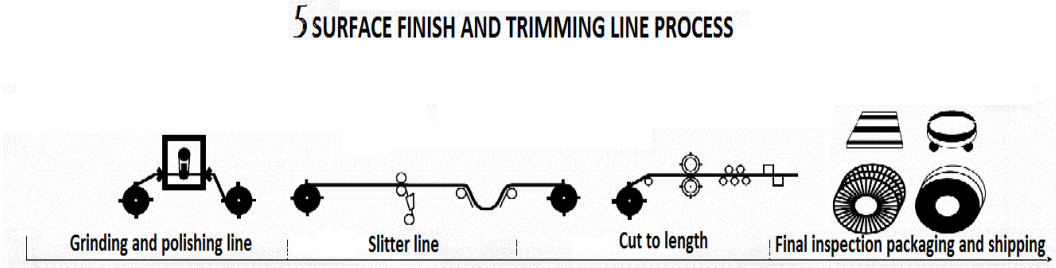

Figure 2.3.6: Typical surface finish, slitting, coiling process of stainless steel strip coil.

In the surface finishing line, the product can be ground and polished with abrasive belts to the desired surface finish according to the customer's specification. The product can be given different surface finishing such as a rough surface finish, a mirror surface finish or a scratches/fingerprints protected coated surface finish. After surface finishing, the material is trimmed into specified dimensions by a laser or shear cutter on the slitter line and cut into required lengths before coiling at the 'cut to length' line. Final inspections are done to ensure that the products meet quality standards before being packed.

2.4. Evolution and modification of as-cast structure during the solidification process of FSS

2.4.1. Introduction

During production of FSS sheet/strip, the first stage is a continuous casting process producing cast steel slabs of typically 200 mm thickness. The solidification begins immediately when the molten steel enters into the casting mould through a bifurcated SEN. The liquid to α-Fe, ferrite phase transformation results in evolution of three main types of dendritic microstructural zones, namely chill, columnar and equiaxed zones. When the molten steel enters the mould, it makes contact with the colder mould wall surface and a high cooling rate is experienced, causing many nucleation sites along the mould wall and formation of very fine approximately equiaxed grains known as the chill zone. The chill zone forms a narrow band adjacent to the mould wall, see Fig.2.4.1 below. The chill zone does not grow inward very far since nucleation stops and solidification by growth of the columnar grains begins.

The chill zone grains have a dendritic interface, which links solid (chill grains) and liquid (molten metal) phase. The dendritic interface grains will either have dendrites oriented perpendicular to the wall or others will have their dendrite axes at an angle to the mould wall. With the growth competition process, the grains with dendrites perpendicular to the mould wall tend to crowd out the other grains resulting in a large and long columnar structure oriented with their dendritic interface parallel to heat flow direction [25]. The columnar dendritic structures grow predominantly into the centre of the mould in a direction opposed to the heat flow behind an advancing dendritic interface.

During growth of columnar dendritic structures, solutes are rejected from the solidified phase and remain in the liquid at the advancing solid-liquid (dendritic) interface. Solutes rejection is caused by the lower solute solubility limit in the α-Fe phase than in the liquid phase. The rejected solutes build-up which causes a higher concentration of solutes in the liquid than was present in the initial concentration of the melt. The overlapping of the constitutional supercooled regions at the centre, causes homogeneous nucleation of equiaxed grains at the centre of the slab, see Fig. 2.4.1. However, not only constitutional supercooling plays a role in the formation of an equiaxed dendritic structure but fragmented dendrites formed by the convection current flow of cold and hot liquid melt. These dendritic fragments are suspended within the liquid melt and tend to act as nucleation sites for equiaxed grains at the centre of slab. As solidification continues, these small dendritic fragments grow and crowd together, eventually ceasing the inward growth of columnar dendrite structures as they fill up the centre of slab. This point is known as columnar-equiaxed transition.

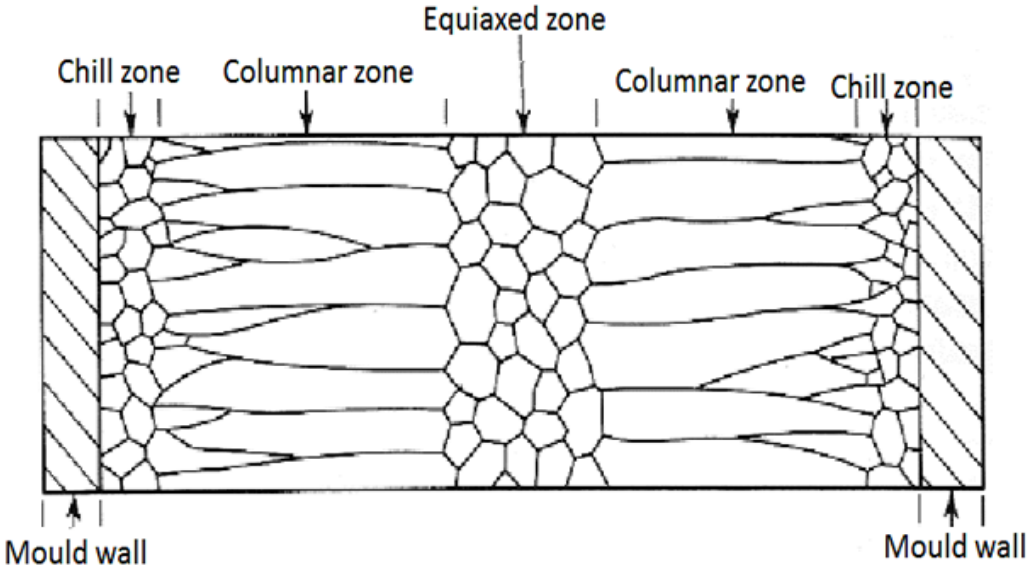

Figure 2.4.1: Schematic diagram of a cross section of a slab showing morphology of as-cast structure [25].

However, there are other factors also, including thermodynamic and kinetic mechanisms as well as casting parameters, which govern the solidification of as-cast zones during continuous casting. These factors can be controlled to achieve the desired as-cast microstructure. These factors will be considered in detail under the following sections of this chapter.

It has been reported that as-cast equiaxed grains offer improved metallurgical properties if compared to columnar grains. For example, fine-grained equiaxed cast structures reduce susceptibility to hot tearing and generally improve structural homogeneity during and after thermo-mechanical processing [26]. Equiaxed structures with their random texture, resulted in the desired forming properties of the final rolled and annealed product. On the contrary, columnar cast structure with their predominantly cube texture, impairs the subsequent cold forming properties. This is a subject of interest for the objective of this study, namely to understand the influence of as-cast equiaxed and columnar structures on the rolling texture evolution and forming properties of final rolled product in the FSS 433.

2.4.2. Factors that influence evolution of equiaxed and columnar cast structures during solidification of FSS

The solidification process during continuous casting can be influenced by various metallurgical factors, which determine the types of solidification microstructures and inclusions that form in the cast slab. Some of these factors are thermodynamic and kinetic (heterogeneous nucleation and constitutional undercooling), the chemical composition of an alloy and casting parameters (casting speed, tundish superheat, cooling rates and mould fluxes). These factors are discussed in some detail below.

2.4.2.1. Heterogeneous nucleation and growth of crystals during solidification in FSS

FSS solidifies through heterogeneous as opposed to homogeneous nucleation of solid grains in the liquid. Heterogeneous nucleation occurs on mould walls and at preferential sites within a melt, such as on solid particles within the melt, e.g. inclusions, fragmented dendritic structures or on added nucleants.

The solid-liquid interface between the particles or the mould wall and liquid melt provides an extra driving force for nucleation of the second phase (crystal solid). Therefore, this leads to lowering of the activation energy for nucleation of crystals or grains. This is well covered in the basic solidification theory and equations 1 and 2 are generally applied for heterogeneous nucleation solids whereby r* and (ΔG^*) are the critical embryo size and the activation energy respectively:

$$r^* = -\frac{4\gamma_{ls}}{(\Delta G_v)(2-\cos\theta-\cos\theta^2)}$$

Equation: 1

In addition, the activation energy is defined by equation 2:

$$\Delta G^* = \frac{4\pi(\gamma_{ls})^3(2\ -\ 3\ \cos\theta\ +\ \cos^3\theta)}{3(\Delta G_v)^2}$$

Equation: 2

where ΔG_v is the chemical driving force for nucleation, γ_{ls}, is the surface energy at the interface of liquid and solid and θ the contact angle at the interface of the nucleus and substrate solid particle or nucleant. The columnar zone is the region that forms just after chill zone. It is composed of elongated columnar grains which are oriented in the most favourable crystallographic direction for fast growth, e.g. in a cubic crystal structure the <100> direction perpendicular to the mould wall or parallel to the solidification front direction is the preferred growth direction. The decisive accommodating factor here is the loosely packed plane $\{100\}$, which readily allows new incoming atoms into the solid crystal lattice from the liquid phase during solidification. Unlike as in the chill zone where solidification is by nucleation and growth, here it is only by the latter, i.e. by growth of the columnar grains. The columnar grain size is generally coarse since favourably oriented grains in the dendritic grain interface or solidification front grow faster and overtake the rest [25].

2.4.2.2. Continuous casting factors which influence the size of the equiaxed zone

The depth of equiaxed zone is highly influenced by intrinsic casting factors, namely convection currents, heat transfer in the alloy, heat flow in an ingot to dissipate superheat, the separation of liquidus and solidus (freezing range, ΔT_f) of an alloy, stirring of the melt during casting etc. These factors can be controlled to some extent to promote production and widening of the equiaxed zone. Verhoeven [25] outlined steps on how to increase the size of the equiaxed zone by means of using factors mentioned above during casting.

- Low superheat, approximately below 20°C for FSS, deepens the equiaxed zone. This is due to the high possibility of dendrite fragments to survive within the melt and create nucleation sites of equiaxed grains at the center of mould. A large superheat tends to prematurely melt these dendrite fragments.
- A large gap between the liquidus and solidus of the alloy which results in a large freezing range for the alloy, i.e. $\Delta T_f = T_{liquidus} - T_{solidus}$, therefore a large ΔT_f leads to longer dendrite lengths L (i.e. $L = \frac{\Delta T_f}{G_A}$) at the solidification front that are more fragile and easily fragmented by convection currents, thus promoting the size of the equiaxed zone.
- A sand mould promotes the formation of an equiaxed zone if compared to a metal mould. It generates a low $\Delta T/\Delta x$ at the liquid/solid interface that increases the length of fragile dendritic grains at the liquid-solid interface.
- An alloy with a low melting point has a low $\Delta T/\Delta x$ which results in longer dendrite lengths at the dendritic interface, hence a larger equiaxed zone.

- Rapid mixing, e.g. by aid of EMS, increases fluid flow that helps in fragmenting the dendrites at the solidification front and superheat is dissipated quickly which maximizes the possibility of dendrite fragments surviving to act as nucleants.

With all of the above factors, dendrite fragments that remain in the melt until the superheat has dissipated, would eventually become equiaxed grains, hence the more these fragments remain within the melt the wider is the equiaxed zone at the centre of the ingot/slab. However it is important to highlight that not all dendrites at the solidification front break up, some remain unbroken and grow inward from the mould wall towards center mould as columnar grains.

2.4.2.3. Influence of chemical composition on the formation of columnar and equiaxed cast structures

Alloying elements such as Al, Nb, Ti, Mn, Si, Ca et cetera can be used to control the evolution of columnar and equiaxed zones during solidification. Hu *et al* [27] observed that addition of both at least 0.17wt%Nb and 0.05wt%Ti to the 17% Cr FSS grades, reduces the grain size considerably and widens the equiaxed zone. These added alloying elements also influence the subsequent formation of the rolling and recrystallization texture during rolling and annealing processes. The authors observed that TiN, at high temperature, could reduce the grain size by grain boundary pinning while maximising the equiaxed zone proportionally by acting as nucleation sites for the equiaxed crystals [27].

It was also found that Al can significantly increase the equiaxed crystal zone in 430 FSS proportionally in correlation with addition of Al. Fan *et al.* [28] found that an optimal addition occurs at 0.19wt%Al in AISI 430 FSS, yielding an equiaxed-to-columnar grain ratio of about 55%, while a greater or lesser proportion causes less formation of an equiaxed grain ratio. An increase in the addition of Al increases the melting temperature of the steel as well as the volume fraction of Al_2O_3 and AlN inclusions. The Al_2O_3 inclusions form with a small particle size and a large volume fraction spread evenly across the melt, thereby providing more nucleation sites for equiaxed grain crystals during solidification and consequently refining the grain size. The AlN reduces the soluble N content and prevents γ—Fe (austenite) phase stabilisation at higher temperatures while providing nucleation sites for equiaxed grains [28].

2.4.2.4. Effect of continuous casting parameters on columnar and equiaxed evolution

Casting parameters such as casting speed, mould oscillation mode, tundish superheat and lubrication processes have a marked influence on the evolution of solidification structures. When a FSS slab forms, it initially solidifies by forming a thin chill zone on the mould wall, succeeded by a columnar zone and finally an equiaxed zone pattern when observed from the surface towards the centre of the cast slab, see Fig. 2.4.1 above.

Superheat

Tundish superheat, as one of the casting parameters, has a significant influence on solidification zones [29]. For example, in 17%Cr FSS, it was found that when the tundish charges the mould caster with a lower superheated liquid metal of about 20ºC (superheat is the temperature gain above melting point of metal) as opposed to the higher 140°C, solidification develops a wider equiaxed zone while constricting the columnar zone [29]. This phenomenon is due to the faster dissipation of superheat and latent heat of fusion inside the mould during the solidification process. When the superheat is dissipated more quickly, it increases the possibility of dendrite fragments to survive within the melt thereby creating many nucleation sites of equiaxed grains. With the aid of EMS, rapid mixing of the

melt can be achieved and this promotes superheat dissipation, hence the formation of an equiaxed structure is promoted [29]. Fig.2.4.3 below shows the effect of different degrees of tundish superheat on the solidification structures.

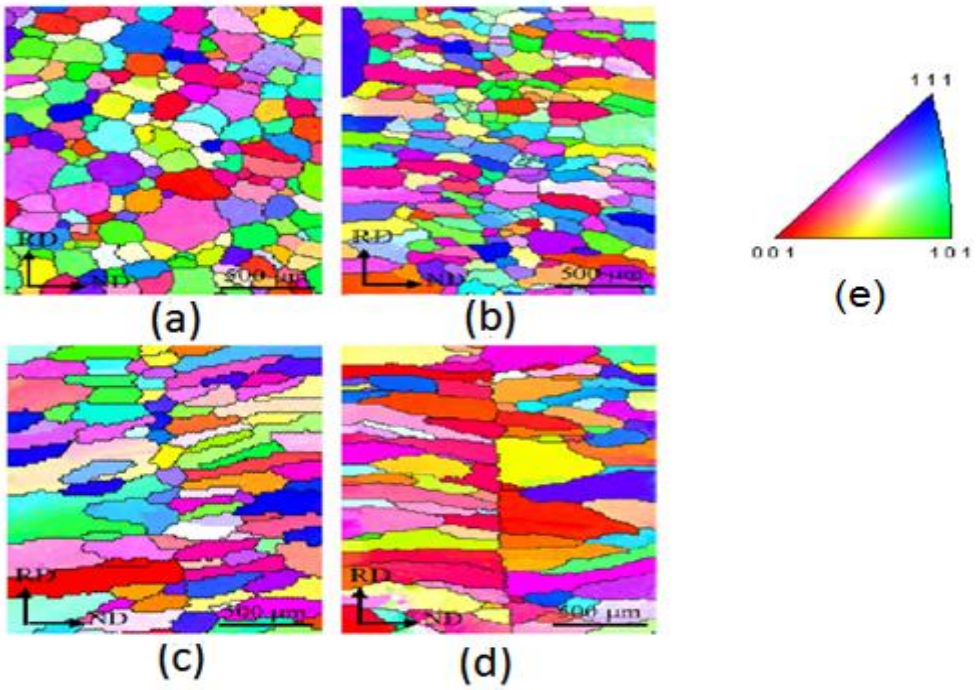

Figure 2.4.3: Typical EBSD micrographs of 17%Cr FSS cast strip with various degrees of melt superheat, (a) 20°C , (b) 60°C , (c) 95°C , (d) 140°C and (e) [001] inverse pole figure [30].

In the contrary, when the superheat exceeds 20°C, the prior-nucleated crystals in the mould dissolve into the hot liquid pool due to the higher liquid temperature. The liquid temperature in the mould comes closer to the liquidus temperature of the metal, thereby lowering undercooling at an early stage of solidification. Therefore the remaining driving force for solidification is used sparingly by capitalising on the energetically favourable direction which has lower surface energy than the equiaxed grains and that causes the columnar grains to develop and advance towards the centre of the cast section. Therefore, increasing the superheat increases the size of the columnar zone as shown in Fig.2.4.3 above and delays the columnar to equiaxed transition (CET).

Liu *et al* [30] further proposed a concept of the superheat effect on solidification structure by constructing a curve that shows a relationship between the percentages of equiaxed grains in as-cast slab versus superheat temperature in the tundish during continuous casting, see Fig.2.4.4 below. It was found that columnar solidification starts above a superheat of 40 ^{o}C.

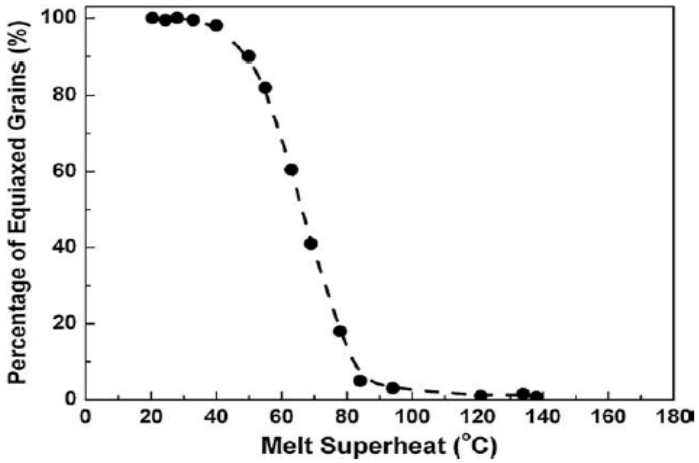

Figure 2.4.4: The effect of melt superheat on the percentage of equiaxed grains in the as cast slab [30].

Casting speed

The casting speed affects the size of the solidification zones because it influences the thermal gradient and solidification modes. Hou *et al* carried out a study on the influence of casting speed on the widths of equiaxed and columnar zones during continuous casting of high carbon steel (0.7%C, 0.65%Mn) billets [31]. Fig.2.4.5 below depicts the relationship between casting speed and number of grains in the equiaxed grain zone that was found.

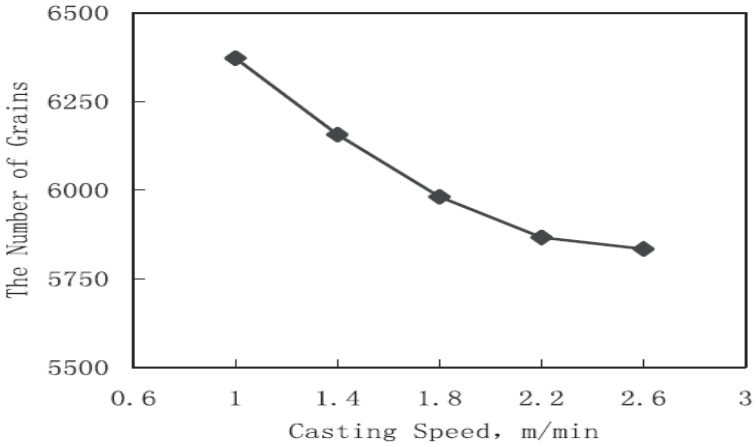

Figure 2.4.5: Grain number of central equiaxed grain zone of billet under different casting speeds for high carbon steel [31].

It was found that the highest number of grains was achieved at approximately 1.0 m/min see Fig 2.4.5. However, when the casting speed was increased, the number of equiaxed grains decreased, behaviour of the curve when the casting speed is less than 1.0 m/min was not reported in their studies. The reason could be an increase of cooling intensity with a decrease in casting speed, which leads to a large average temperature gradient ($\Delta T/\Delta x$) at the liquid-solid (dendritic) interface during solidification. It is known that the length of dendritic arm's (L) crystal structures at the dendritic interface is related to $\Delta T/\Delta x$ and freezing range of an alloy (ΔT_f) by equation 3 below [25]:

$$L = \frac{\Delta T_f}{\Delta T/\Delta x}$$

Equation: 3

At a constant ΔT_f , when $\Delta T/\Delta x$ increases with a decrease in casting speed, the L-value decreases accordingly. For a shorter L-value, convection currents in the liquid metal cast do not easily break-off the dendritic crystals at an advancing dendritic interface as compared to longer and fragile dendritic arms at lower values of $\Delta T/\Delta x$. Thus, a lesser number of dendritic fragments is suspended within the liquid metal. This condition leads to lesser numbers of nucleation sites for equiaxed grains in the metal liquid. Hence, a decreases in the equiaxed zone or number of equiaxed grains takes place. A relatively faster casting speed decreases the $\Delta T/\Delta x$ value and the slab reaches the secondary cooling zone sooner which increases ΔT_f, thereby providing a suitable condition for widening of the equiaxed zone [29, 32].

However, different steels will have different optimum casting speed values that will yield maximum equiaxed zone width. Therefore, it relies on achieving a balance for each caster/alloy combination between the casting parameters such as casting speed, super heat, under cooling and the alloy being cast in order to optimize the width of equiaxed grains.

2.4.2.5. Columnar to equiaxed transition models

The properties of final rolled and annealed FSS sheets are affected by the solidification structures. Therefore, it is imperative to understand how the as-cast structures are formed during casting. The equiaxed zone is associated with improved properties in the final product while the columnar zone causes anisotropic properties in the steel sheet, such as deep drawing plasticity. It is a critical concern to understand the formation of columnar and equiaxed structures and of columnar to equiaxed transition (CET) grains during the solidification process. With that knowledge, the metallurgist can manipulate the CET to achieve an optimised solidification structure. Therefore, many authors [26,33, 34, 35] have derived models that will predict the CET during solidification. These models became helpful tools in the casting of FSS such that good control of the desired microstructures and properties can be achieved.

CET model proposed by Tarshis *et al.*

Tarshis *et al.* [33] investigated the variation of the as-cast grain size with respect to the variation of alloying elements (solutes) at a constant superheat for a given alloy system. They used a Ni alloy and an Al alloy to study the effect of alloying elements in the as-cast grain structure's variation And a model was derived which incorporated the solute concentration (C_0). The model was derived by varying the C_0 of a given alloy system at constant superheat and measuring the as-cast grain size at every change of C_0. The relationship is given below as equation 4:

$$P = \frac{-mC_0\,(1-k)}{k}$$

Equation: 4

Where P is a constitutional supercooling parameter, m is mass percent of solute, C_o is the concentration of solute and k is the redistribution coefficient.

In Fig.2.4.4 below, it was found that the relative grain size decreases as the parameter P increases, which promotes CET.

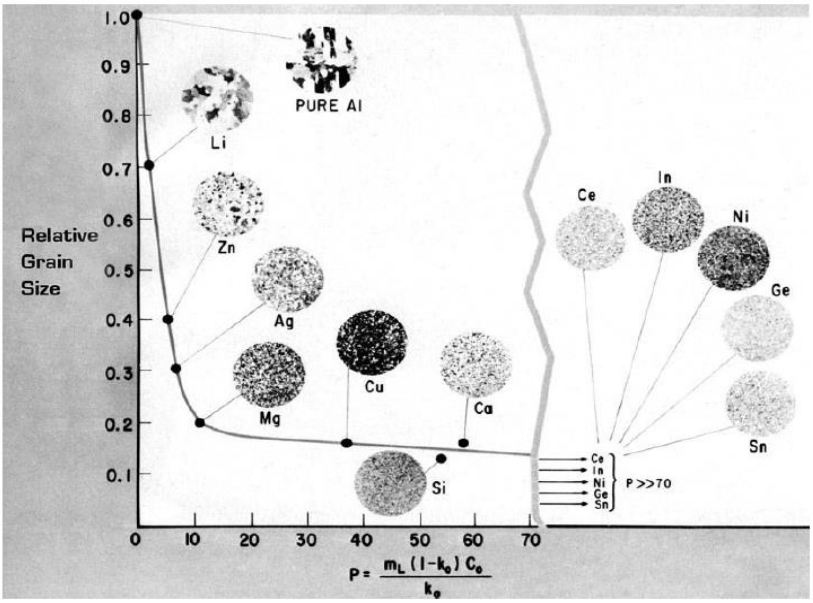

Figure 2.4.4: Variation of relative grain size of Al-1% solute alloy as a function of parameter P [33].

At low P values, the structures were columnar, but they changed to a columnar-equiaxed mixture, and finally to equiaxed as the P value increased [33].

Controlling of columnar and equiaxed growth during solidification is crucial for obtaining optimised final properties of the as cast alloy. For example, if higher strength and ductility is a primary requirement for the application of a material, it is desired to widen the equiaxed zone. When polycrystalline material is wholly equiaxed, a mutual compatibility of deforming crystal grains increases deformation resistance and the larger number of grain boundaries within the material hinder the formation and propagation of the cracks. Nevertheless, when high temperature creep resistance is required, it will be more ideal to have material with large grains (or at the extreme with less grain boundaries) because creep rupture usually originates from the grain boundaries. Growing columnar grains in the direction of the main solidification front's advance, will lessen the grain boundaries in that direction, hence improving the high temperature creep resistance [34]. With the aid of CET models, control of columnar and equiaxed growth becomes easier depending on what properties are required from the material.

Hunt *et al's* CET model

Hunt *et al* [26, 35] developed a CET model based on steady state directional solidification. These authors studied the growth of equiaxed grains in a supercooled liquid ahead of the columnar interface such that conditions required to grow a fully equiaxed structure can be predicted. A mechanism to terminate columnar growth was proposed, that is when columnar growth transforms into equiaxed growth. CET will take place when the volume fraction of equiaxed grains at the columnar growth front exceeds 0.66.

Hunt *et al*. calculated that wholly equiaxed growth would occur when the steady state temperature gradient ($\Delta T/\Delta x$) is below a critical value given by equation 5:

$$\left\{\frac{\Delta T}{\Delta x}\right\}_{ss} < 0.617\, N_o^{\frac{1}{3}}\left[1-\frac{\Delta T_N}{\Delta T_C}\right] * \Delta T_C$$

Equation: 5

Where $\{\Delta T/\Delta x\}$ is the steady state thermal gradient, N_0 is the number of nucleation sites per unit volume, ΔT_N is the critical undercooling for nucleation, ΔT_C is the critical undercooling at the columnar growth front.

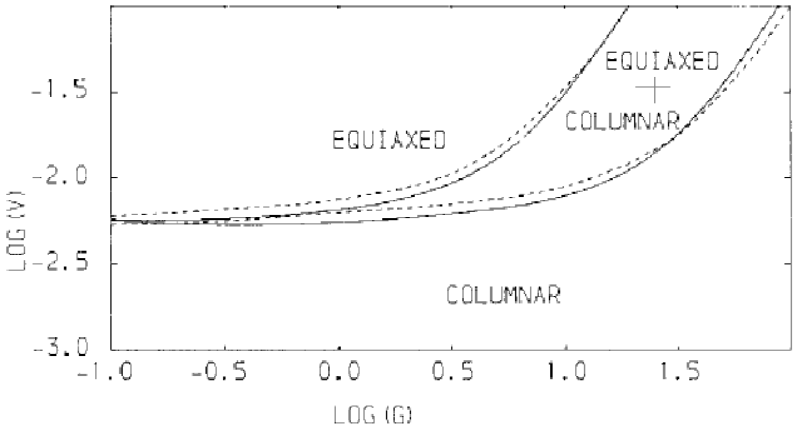

Figure 2.4.5: Plot of growth rate (Log (V)) versus temperature gradient (Log (G)=log{ΔT/Δx}) for Al-3wt%Cu alloy showing columnar and equiaxed regions calculated from approximate analysis of the CET model [33].

This model was applied on the aluminium alloy Al-3wt%Cu, see Fig.2.4.5. The model predicts that at a high solidification velocity (V), more nucleating sites are generated at a relatively low thermal gradient (ΔT/Δx), and equiaxed growth increases, while at a low solidification rate and a higher thermal gradient, the growth of columnar grains predominates [26]. The critical undercooling at the columnar front is defined in terms of the initial concentration of solutes (C_0) and solidification velocity (V) given in equation 6:

$$\Delta T_C = [-A' m\,(1-K) C_0\, V]^{\frac{1}{2}}$$

Equation: 6

Where $-A'$ is material constant, and $-m(1-K)C_0$ is a columnar growth restriction factor. When the growth restriction factor increases, columnar growth is inhibited while equiaxed growth increases, which means CET is promoted, depending on the metal alloy.

CET model proposed by Lin *et al.*

Lin *et al.* [34] postulated their model, which is based on the volume fraction of equiaxed grains that nucleate ahead of the columnar growth front. They argue that in order to determine the critical condition for CET to take place, the volume fraction of equiaxed grains needs to be ascertained before being wrapped up by the columnar growth front. They determine the volume fraction of equiaxed grain based on Hunt's model, which states that fully equiaxed growth may occur if the volume fraction of equiaxed grains is greater than 0.66, whereas the structure is assumed to be wholly columnar if the volume fraction of equiaxed grains ahead of the columnar growth front is less than 0.66.

The distance r_e ahead (radius ahead of the columnar growth front) of the growth front's interface of the columnar grains, is related to the equiaxed volume fraction by equation 7:

$$r_e = \int_0^{z_n} \frac{V_e[z]}{V} dz$$

Equation: 7

Where V_e is the equiaxed growth velocity, V is the solidification growth velocity, z is the distance in the liquid from the dendritic tip parallel to the dendritic axis and Z_n is the maximum distance for equiaxed dendritic growth.
The equiaxed growth velocity (V_e) is based on the local solute concentration and undercooling ahead of the columnar growth front within the radius ahead of the columnar growth front region, r_e.

The local solute concentration distribution ahead of the dendritic tip as a function of z (the distance in the liquid from dendritic tip parallel to the dendrite axis) is given by equation 8:

$$C_i(z) = C_{0i} + (C_i^* - C_{0i})E_1[P_{ei}(2z + R)/R]/E_1(P_{ei})$$

Equation: 8

Where C_{0i} is the nominal concentration of solute species i, C_i^* is a concentration of solute species i in the liquid at dendritic tip, E_1 is an exponential integral function, P_{ei} a Peclet number for species i, and R is the dendritic tip radius.

Equation 8 is represented by the graph in Fig.2.4.6 below using 316 stainless steel material, which was subject to unidirectional solidification at temperature gradient of $\Delta T/\Delta x$ = 1X10^3 K/m . It may be inferred that solidification system has approached the absolute stability when solidification velocity is close to 0.1 m/s.

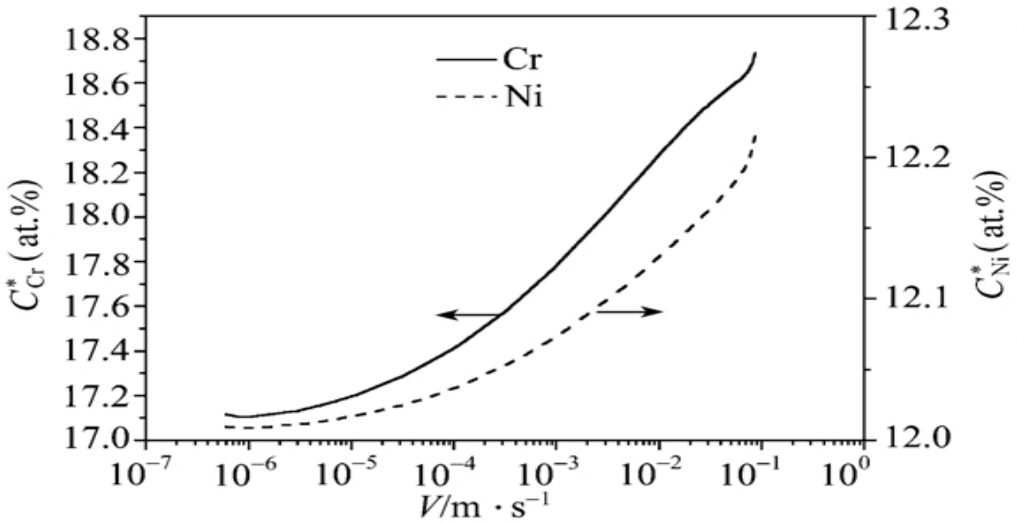

Figure 2.4.6: Variation of liquid composition at the dendrite tip with the growth velocity during unidirectional solidification of 316 stainless steel [35].

The Peclet number is defined as $P_{ei} = \frac{VR}{2D_i}$ for species i, V is a solidification growth velocity and D_i is the diffusion coefficient of solute i in the liquid. Peclet number is a ratio of thermal energy convected to the fluid to the thermal energy conducted within the fluid (metal liquid). In addition, the local undercooling profile ahead of the columnar growth front is defined by equation 9:

$$\Delta T(z) = T(z) - T_q(z)$$

Equation: 9

Where $T_q(z)$ is the actual temperature distribution in the liquid ahead of the solidification growth front and $T(z)$ is the equilibrium liquidus temperature corresponding to the solute's redistribution in front of the solidification front.

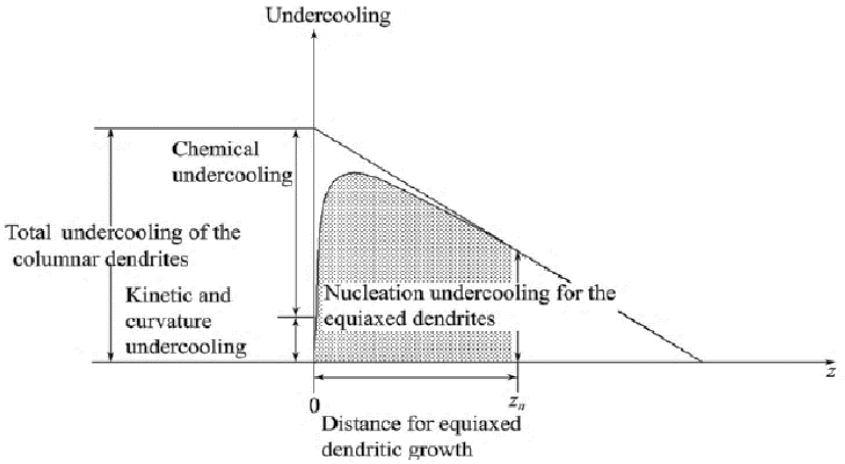

Figure 2.4.7: Schematic representation of the undercooled region of the moving solidification interface, z_n is the distance from the solid/liquid interface in the liquid [34].

The concept of an extended volume fraction was introduced to calculate the volume fraction of equiaxed grains. The extended volume fraction is defined by using the Avrami actual volume fraction equation, given in equation 10 [36]:

$$\phi = 1 - \exp[-\phi_e]$$

Equation: 10

Where ϕ is the actual volume fraction and $\phi_e$is the extended volume fraction. It was assumed that equiaxed growth takes place in a spherical mode, and the total number of nucleation sites will quickly reach the number of heterogeneous nucleation sites once nucleation undercooling occurs, in which case the extended volume fraction is expressed by equation 11:

$$\phi_e = \frac{4\pi\, r_e^3\, N_0}{3}$$

Equation: 11

Where, N_0 is the total number of the heterogeneous substrate particles originally available per volume. To predict the CET condition, Hunt's model was developed which incorporated the extended volume fraction (ϕ_e) of the equiaxed structure in terms of the number of heterogeneous nucleation sites. Hunt's model defines the critical thermal gradient ($\Delta T/\Delta x$) and the rate of advance of the solidification front (V) required for the CET by using Lin *et al's* model - see Fig. 2.4.8 and 2.4.9 below for an illustration of how the Lin *et al.* model operates.

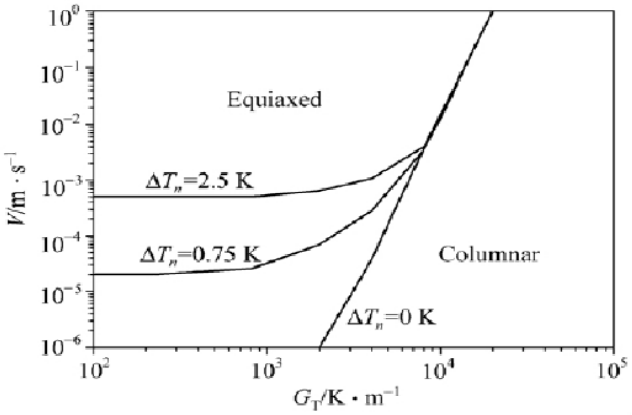

Figure 2.4.8: Influence of nucleation undercooling on CET, $N_0 = 10^9 / m^3$ [34].

From Fig. 2.4.8, it can be seen that the critical nucleation undercooling ΔT_n has a significant effect on the CET at a lower temperature gradient ($\Delta T/\Delta x$) and has little effect at higher values of $\Delta T/\Delta x$. When the nucleation undercooling is lower, the rate of the solidification growth front becomes lower as well, which renders CET to become easier and to take place at a lower $\Delta T/\Delta x$. However at $\Delta T_n = 0$ K, the CET curve becomes a straight line. This is due to the fact that at a lower temperature gradient ($\Delta T/\Delta x$) and a slow solidification velocity (V), the nucleation undercooling ahead of the growth front is very low whilst the nucleation rate is usually high and the CET curve becomes non-linear when the nucleation undercooling is greater than zero. At this stage, the nucleation undercooling has a decisive effect on the CET curve.

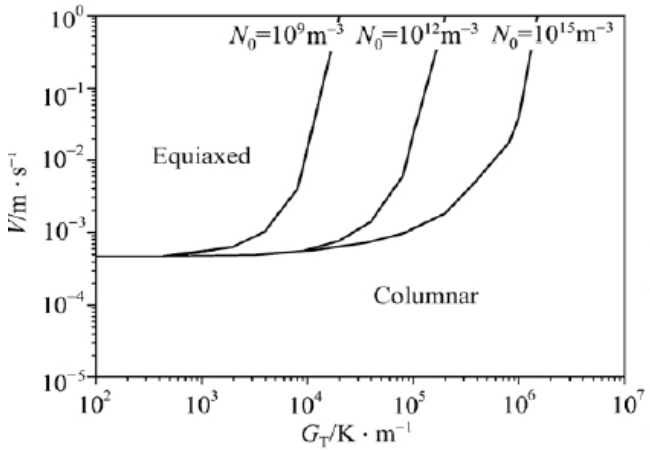

Figure 2.4.9: Influence of number of nucleating sites on the CET ($G_T=\Delta T/\Delta x$), $\Delta T_n = 2.5$ K [34].

Fig. 2.4.9 above shows the effect of the number of nucleation sites (N_0) on the CET curve at a constant nucleation undercooling ΔT_n, where G_T is an effective temperature gradient. As may be seen, for a different number of nucleation sites, undercooling has less effect on the CET curve at lower thermal gradient ($\Delta T/\Delta x$) but has a considerable effect at higher values of $\Delta T/\Delta x$. However, with increasing number of nucleation sites (N_0), the CET extends to the higher $\Delta T/\Delta x$ at a constant critical solidification front's growth rate and hence leads to a widened equiaxed zone. This is mainly due to the fact that N_0 determines the number of equiaxed crystals, which can grow once a critical undercooling is reached. The more nuclei (N_0) in the liquid, the more the number of equiaxed crystals, and the larger the volume of equiaxed crystals and the easier CET takes place.

2.4.3. Modification of as-cast structures during the solidification casting process by means of electromagnetic stirrer devices

The Japanese steel industries developed a device known as the Electro-Magnetic Stirrer (EMS) that is used to modify the as-cast structures [37, 38]. The EMS uses Lorentz forces to stir molten steel during the continuous casting process in order to improve the as-cast structure's quality. Three types of EMS have been developed which can be positioned at different locations of the casting process; namely,

- an in-mould electromagnetic stirrer (M-EMS) which stirs the molten steel inside the mould,
- the strand electromagnetic stirrer (S-EMS) which is located just below the mould in the secondary cooling zone; and
- the final electromagnetic stirrer (F-EMS) which is installed near the exit of the slab caster.

The main use of an EMS is to improve grain refinement, to eliminate surface defects, inclusions, to reduce solute segregation and thus enhance the forming properties in the final FSS sheet product. In steel industries where crystallographic texture is a concern, EMS is used. This promotes the nucleation and growth of equiaxed grains with a random texture during the solidification processes and this enhances grain refinement, and a reduction of inclusions within a steel slab. The random grain orientations are achieved by breaking the fragile dendritic grains at the solidification growth front, which then act as preferred sites for the nucleation of equiaxed grains. EMS has also been found to eliminate breakout of the initial solidified shell thickness during casting while it also contributes to an improvement of the presence of surface defects and the inner structure of the cast steel slab [38, 39, 40].

As-cast steel slab products, mainly FSS and electrical steels, develop a very narrow band of equiaxed grain structures during the continuous casting process [41]. Fig. 2.4.10 (a) below shows a macro-etched section of 433 FSS slab comprising a large volume fraction of columnar grains growing towards the centre of the slab section and a narrow band of equiaxed grains at the centre of the slab. This slab was cast without the use of an electromagnetic stirrer device.

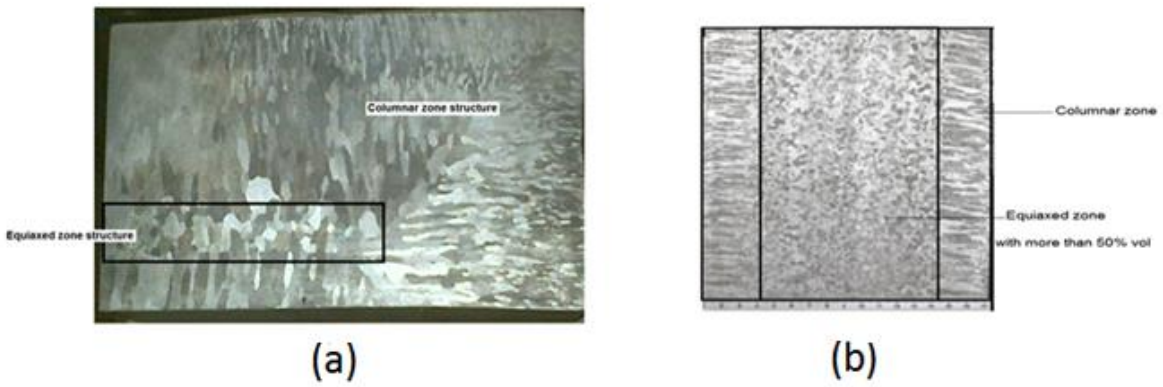

Figure 2.4.10: (a) Macro-etched AISI 433 steel slab revealing a small volume fraction of equiaxed grains after casting without EMS, (b) AISI 430 shows the equiaxed grain zone achieved by using EMS [40].

With the use of EMS, the equiaxed grain structure exceeded 50% volume fraction in the 430 FSS slab; see Fig. 2.4.10 (b) above.
The equiaxed grains form because of the M-EMS and S-EMS, which break the dendrite tips during their early stage of nucleation. The fragmented tips are left in a uniform suspension in the liquid steel where they act as nucleants for equiaxed grains. This results in a wide equiaxed zone as well as grain refinement, particularly in the secondary cooling zone [40, 41].

2.5. Thermo-mechanical, cold working and annealing processes of FSS

2.5.1. Hot rolling process of 433 FSS

433 FSS continuously cast slabs are reheated to temperatures between 1100°C and 1200°C, a range where most precipitates dissolve. The metallurgist needs to strike a balance between the benefits of high and low reheating temperatures. A high soaking temperature permits dissolution of significant amounts of precipitates with a negative effect of grain growth, while a low soaking temperature inhibits grain growth but leaves excessive precipitates undissolved [42].

After reheating, the 433 FSS is allowed to cool down to a hot working temperature, normally ranging between 950°C and 1000°C, which is conducive to hot working ductility without material cracking or forming of embrittlement phases. With a high diffusion rate of solutes through the α – ferrite phase matrix within the hot-working temperature range, the material readily homogenises the solutes. Usually the finish rolling temperature is kept just above 750°C to ensure homogenisation, and is then rapidly cooled through the 400°C-550°C temperature window to avoid 475°C embrittlement.

The material deforms in two different modes through its thickness during hot rolling. The surface deforms due to shear strain caused by slip friction between the working rolls and the material's surface. The shear deformation mode forms shear bands at the surface and introduces a high dislocation density in that zone. Consequently the surface normally has very fine recrystallized grains just after hot rolling, see Fig. 2.5.1 below illustrating Inverse Pole Figures (IPFs) //RD taken from a 430 FSS hot deformed transfer bar during a study of the texture gradient occurring through the thickness [43].

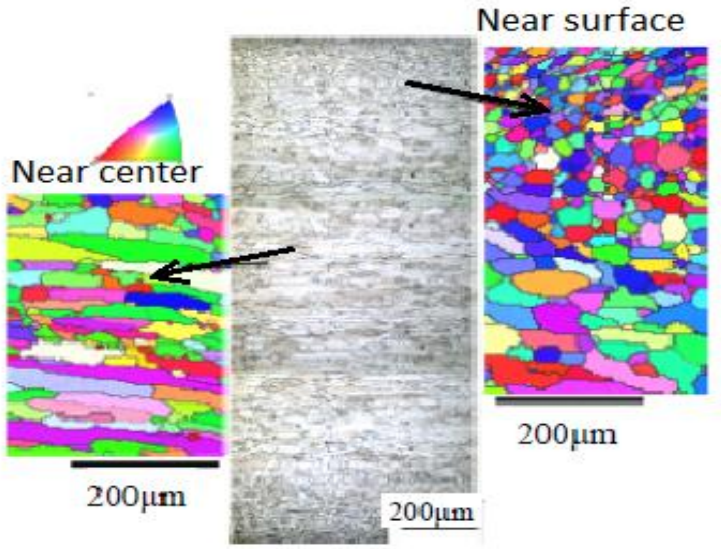

Figure 2.5.1: IPF//RD through thickness of 430 FSS after hot rolling showing partial recrystallized grains near the surface and elongated unrecrystallised grains near the centre [43].

However, material near the centre merely deforms under plane strain conditions, thus causing grains to elongate along the RD with a lesser dislocation density, with the result that unlike the material near the surface as depicted in Fig. 2.5.1 above, material in the centre is difficult to recrystallize during hot

rolling. This deformation behaviour influences the evolution of the microstructure as well as the texture through the thickness. Hot bands of FSS, therefore, generally exhibit a texture gradient through the thickness.

Hot rolling in stainless steel production in some plants is divided into roughing and finish hot rolling. Rough rolling breaks down the as-cast structure in the slab as the slab is reduced to a thickness of the transfer bar before it proceeds to the finish hot rolling mill. Rough rolling is done in the dynamic recrystallization (DRX) region in order to optimise the grain size [42]. At this stage grain growth control is achieved by using a thickness reduction schedule together with the presence of carbides that inhibit growth of recrystallized grains. The roughing rolling of 433 FSS is performed at temperatures ranging from 824°C to 970°C [12].

After rough rolling, the steel is further finish hot rolled by subjecting it to the hot finish rolling stage. The starting finish hot rolling temperature ranges between 900 and 950 °C and the exit temperature ranges between 750°C and 850°C. The final standard gauge thickness is typically aimed at 32 to 3.5 mm, for an as-cast slab of 200 mm thickness as the starting material [12]. During this stage, sufficient strain accumulates to initiate DRX that results in grain refinement.

2.5.3. Cold rolling

Cold rolling is a process whereby material is simultaneously deformed into thin flat sheets and strengthened at room temperature. This rolling stage is mainly performed well below the recrystallization temperature of an alloy. This allows hot rolled plate reduction to thinner gauges of sheets, strips or foils with good surface finish and increased tensile strength but lessened ductility. The alloy is strengthened by increasing the number of dislocations and utilising work hardening or strain hardening. A usable shape with improved properties is achieved at a scheduled amount of cold work and subsequent annealing.

Cold working affects the microstructure's morphology. The grains are compressed along the thickness direction (ND) and elongated along the rolling direction RD, which serves to accommodate the induced deformation energy. Grain boundaries remain intact under these circumstances while all individual grains undergo the same change in shape but with different orientations. The changes in grain orientation are dictated by slip systems that attain their critical resolved shear stress during plastic deformation, i.e. in bcc metals and alloys this is in the family of {110}<111> slip systems [44]. Fig. 2.5.2 shows the difference between a cold rolled and an annealed microstructure [45].

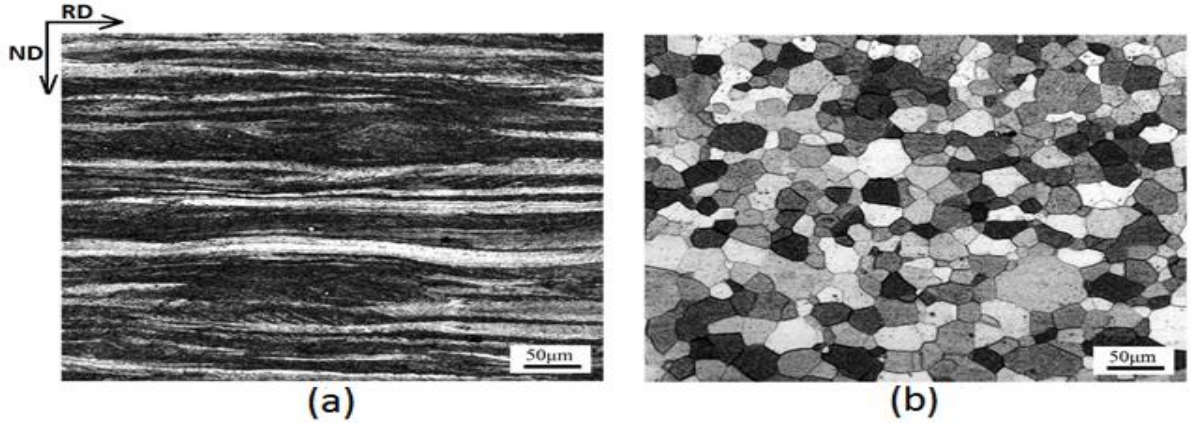

Figure 2.5.2: Optical micrographs for the microstructures in the TD plane after cold rolling (a) 80% cold reduction microstructure and (b) cold rolled and annealing at 950°C for 3 minutes microstructure [45].

The cold rolling process is effectively a plane strain deformation mode. The material undergoes extensive plastic deformation and lengthening along the RD while the thickness is reduced considerably along the ND with little spread of material along the width (TD). During hot and cold rolling processes, a portion of plastic deformation energy will be introduced into the material system and therefore the total energy of the material system will be increased which acts as a driving force for the recrystallization process during the annealing stage [46].

2.5.4. Annealing

Annealing is a heat treatment designed to soften cold-worked materials and restore their ductility while achieving their tensile strength and hardness at the required level. During this process, the materials can experience recovery, recrystallization and grain growth softening mechanisms.

2.5.4.1. Recovery

The original cold worked microstructure of an alloy consists of deformed grains with a high density of tangled dislocations. During annealing, vacancies will facilitate the movement of dislocations to form a polygonal sub-grain structure. The dislocations will rearrange and form cell walls in the matrix. Fig. 2.5.3 below shows typical schematic diagrams of cold worked microstructures and microstructures in the recovered condition with polygonal sub-grain structures.

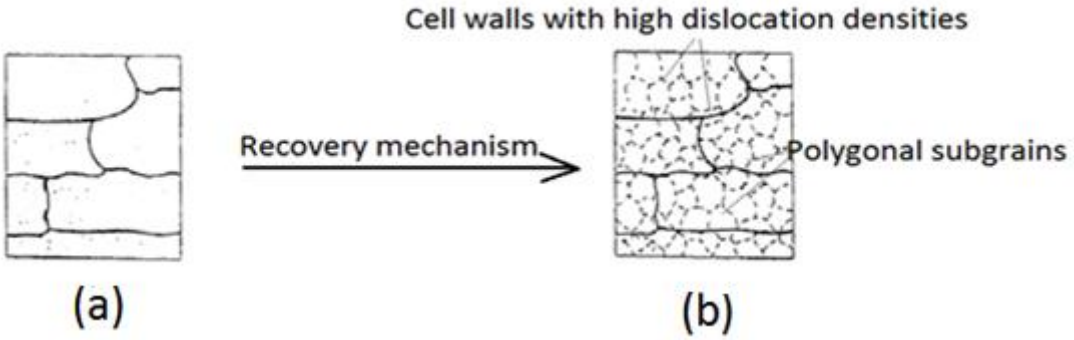

Figure 2.5.3: Schematic diagram depicting microstructures of an alloy (a) in the cold worked condition, (b) in the recovered condition [47].

The dislocation density remains virtually unchanged during recovery but is rearranged into cell wall boundaries to form polygonal sub-grain structures. Since the dislocation density is not materially reduced during recovery, the mechanical properties are also relatively unchanged. However residual stresses that develop during cold rolling are eliminated from the microstructures, hence recovery is also referred to as stress-relief annealing.

Since FSS have a high stacking fault energy, which lessens strain hardening as compared to ASS [48], the recovery stage is rapidly reached and lowers the cold worked energy. However, based on the alloy composition and cold working history, the temperature required to initiate stress relief (recovery) can be calculated with due allowance for the predetermined residence time.

Since recovery normally precedes recrystallization, it lessens the stored cold-working energy needed for recrystallization. Prolonged recovery time may even inhibit recrystallization, in that case considerable thermal activation energy will have to be supplied extraneously to enable recrystallization.

2.5.4.2. Recrystallization

Static recrystallization (SRX) occurs at or just 50 °C above the critical recrystallization temperature of an alloy. The critical recrystallization temperature equates slightly above the $0.7T_m$ (of the alloy's absolute melting point), depending on the amount of cold work [48]. This process occurs through nucleation and growth of the new grains from the deformed matrix resulting in new grains containing few dislocations. The nucleation of new grains can also be initiated by a hard particles such as inclusions, carbides, nitrides or etc. within deformed matrix, this mechanism is known as particle stimulated nucleation (PSN) or through by strain induced boundary migration (SIBM) [48]. When deformed metal is heated above the recrystallization temperature, recovery rapidly eliminates residual stresses for metals with high stacking fault energy (SFE), such as FSS and produces a polygonised sub-grain structure with dislocations settling on the sub-grain's cell walls. New grains then recrystallize at the cell wall boundaries of the polygonised structures where dislocations are concentrated, eliminating most of the dislocations, with the result of new grains with a low dislocation density.

2.5.4.3. Grain growth

If a metal is kept at its recrystallization temperature for a prolonged time, grain growth will start immediately as a new grain is formed from SRX and resulted into larger grains. The recrystallized grain structures are predominantly characterised by fine grains with a consequently increased grain-boundary area that drives grain growth by reducing the grain boundary area per unit volume. Grain growth proceeds until grain boundaries per unit volume are eventually reduced to a few larger grains. Fig. 2.5.4 below depicts alloy microstructures undergoing grain growth over a prolonged period. The grain growth kinetics depends on the surface energy of the grain structures as well as the grain size at any specific point. Fig. 2.5.5 shows the grain size as a function of time at various temperatures.

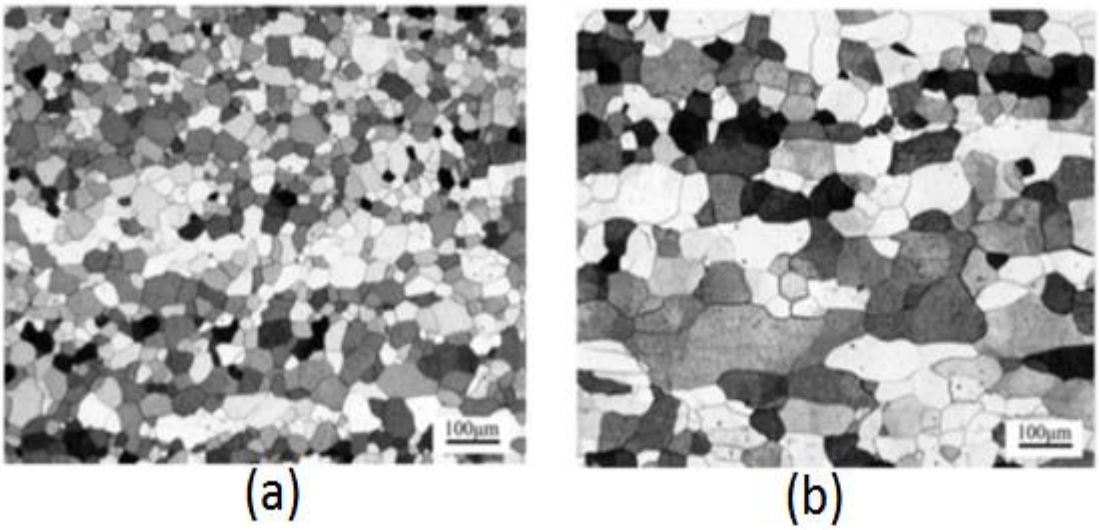

Figure 2.5.4: A typical micrograph of an ultra-purified 21%Cr FSS grade showing the difference between (a) recrystallized grain and (b) grains that undergo grain growth [49].

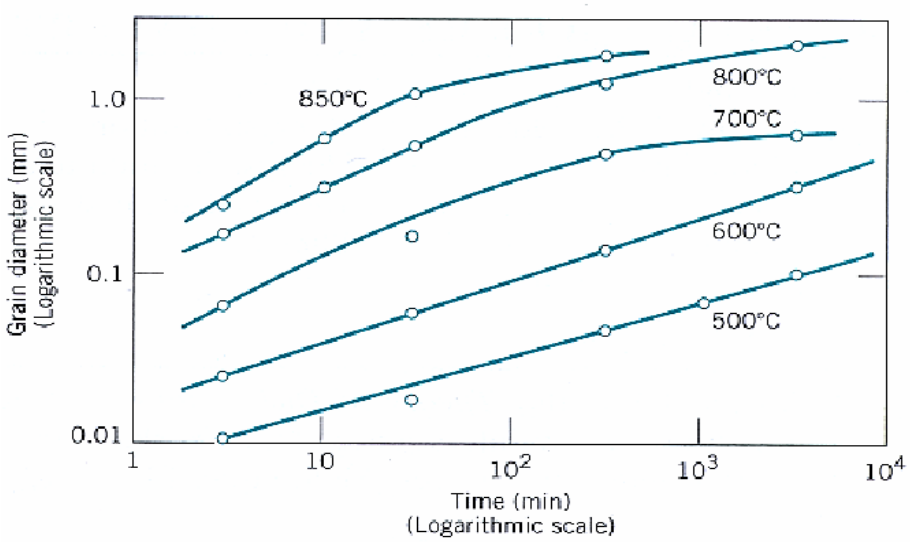

Figure 2.5.5: A typical plot of grain size versus time at various temperatures [50].

Grain growth arises from a radial outwards movement of grain boundaries at the expense of the fine grains that are consumed. The average grain size increases with time and temperature, see Fig.2.5.5. However, there are processes used to hinder grain growth, particularly at elevated temperatures. Metallurgists make use of steel alloys that contain finer precipitates such as carbides or carbo-nitrides in the final product. These precipitates must be large enough in volume fraction, fine enough in size to effectively pin grain boundaries and uniformly dispersed throughout the matrix. At elevated temperatures, like in 433 FSS, fine AlN, TiC, TiN, NbC and other carbides are effective in pinning the grain boundaries through what is called the “Zener-drag” effect.

2.6. Evolution of texture during casting, thermo-mechanical and annealing processes of FSS

2.6.1. Introduction

Most engineered polycrystalline sheet alloys have a preferred grain orientation distribution (i.e. crystallographic texture). Alloys with a characteristic texture have anisotropic properties in the sense that the properties depend on the direction along which they are measured. Texture is a statistical distribution of crystal orientations measured with respect to the relevant sample coordinates, e.g. rolling direction (RD), the transverse direction (TD) and the normal direction (ND). When grain orientations are mainly aligned or clustered in a specific preferred orientation, the alloy is textured, but if the crystal orientations are distributed uniformly, the alloy has a random texture. The alloy can be weakly, moderately or strongly textured depending on the percentage of crystals having the same preferred orientation.

Texture can be measured using various techniques, such as neutron diffraction, x-ray diffraction (XRD) or scanning electron microscopy with an electron backscattered diffraction detector (SEM-EBSD). It is usually represented by means of IPF or an orientation distribution function (ODF). These representations relate the grains or crystal orientations to the alloy workpiece's rolling/processing coordinates. Sample coordinates of rolled sheets can be defined by the RD, TD and ND.

Texture can influence metal properties (e.g. formability, surface roughness, magnetic permeability and etc. of the metal alloy sheet) quite significantly. Metallurgical processes such as casting and rolling are frequently used in the stages of making the alloy sheet. Hot and cold rolling can rearrange the as-cast grain orientations in all (RD, TD and ND) rolling axes by a process known as grain flow and rotation, thereby causing a hot rolling deformation texture. However, cold rolling tends to destroy the grain structure and their orientations extensively and forms elongated platelets along the RD. During annealing of a cold worked alloy, new grains recrystallize with different textures or inherited cold-work textures, depending on the nature of the cold work and annealing processes, as well as the composition of the alloy. A recrystallized texture in the final sheet can have a marked influence on the forming, magnetic and other properties of a metal sheet [54].

Texture control during alloy sheet or strip production is therefore necessary with a view to instil the final desired material's forming and mechanical properties.

2.6.2. Texture evolution during casting of FSS

It is well known that columnar grains with {001} <uv0> as cast texture are prone to deteriorating forming properties in FSS sheets. However, Raabe [52] showed that forming properties of cold rolled and annealed sheets could be improved by initially promoting the formation of a large volume fraction of as-cast equiaxed grains with weak or random texture. Hunter and Ferry [53] found that grains with an <001> orientation in the preferred direction, which are close to the exiting heat flow from the mould wall, grow from the chill-zone interface to produce columnar grains with a strong <001>//ND orientation fibre texture (ND is the normal direction in relation to the mould wall).

In 2009, Liu *et al.* [30] studied the solidification structures and texture development of 17%Cr FSS (Fe–16.9Cr–0.114Ni–0.03C, mass %) produced by twin-roll strip casting. It was found that weak and nearly random textures developed in both equiaxed sub-surface and centre layers of the as-cast strip, see Fig. 2.6.1.

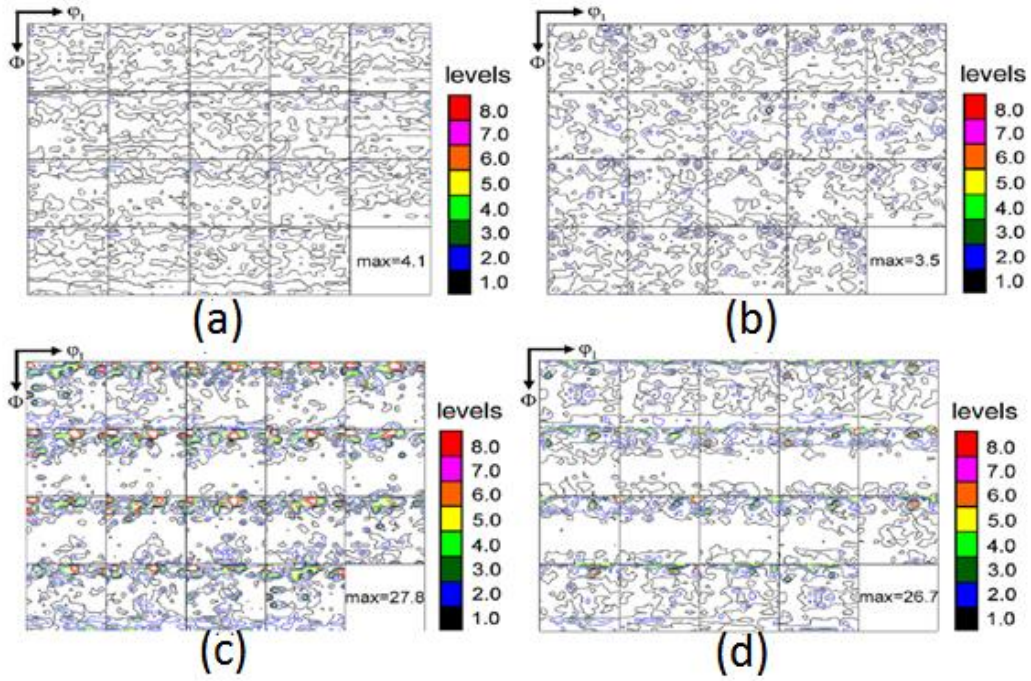

Figure 2.6.1: As-cast texture of equiaxed zones (a) sub-surface, (b) at centre and columnar (c) sub-surface and (d) at centre at constant φ_2=45° ODFs, of 17%Cr FSS [30].

As may be seen in Fig.2.6.1 to the contrary, the columnar-grained strip exhibited a sharp through-thickness <001> fibre texture tilted by about 0° to 15° from the normal as-cast direction.

Adding nucleants during FSS casting modified the as-cast structure and texture evolution. Hunter and Ferry [53] demonstrated that by adding Ti during FSS casting, profoundly changed the evolution of the microstructure and texture during solidification. Textures and microstructures of the same steel but with and without added Ti were compared. Without Ti, the grain orientation was almost random at the surface of the chill zone, but as the solidification progressed the preferred growth of grains with their {001} planes parallel to the ND resulted in a somewhat sharper texture. In contrast, the addition of Ti led to the formation of TiN particles into the interface of the chill zone to the liquid with a strong <001>//ND fibre texture. A subsequent epitaxial growth of dendrites from the particles inherited the initial particle's orientation, intensified the <001>//ND fibre texture of dendrites in the as-cast strip to an extent that exceeded that observed in the Ti-free FSS [53].

2.6.3. Effect of the hot rolling process on the evolution of texture in ferritic stainless steel

The hot rolling process is intended to improve the as-cast grain structure and form a new hot band grain morphology with a different texture. Therefore, it is imperative to understand the development of the hot-band texture and its microstructures because they affect the subsequent cold rolled and annealed textures and also their final mechanical and formability properties.

Raabe *et al*. [6] noted that the hot-band texture could be influenced by various metallurgical factors such as processing parameters, thermodynamics, initial microstructure and the crystallographic texture of the alloy. In their study, it was found that the slab reheating temperature and soaking time, hot rolling schedules (deformation in the ferrite phase, reduction scheme, and strain rate through the thickness), precipitation behaviour, stored deformation energy and stacking fault energy influence the evolution of texture.

During hot rolling of thick FSS plates, considerable texture variation through the thickness has been observed; see Fig. 2.5.1 [6, 43]. At the centre, the grains are flat and elongated with a low fraction of recrystallized grains. The texture at the centre comprises a strong α-fibre and a weak γ-fibre texture, whereas the surface comprises a large amount of recrystallized grains consisting of equiaxed grains with a texture that is completely different from that of the centre layer, i.e. mainly with pronounced $(001) < 112 >$ and shear (Goss) $(011) < 100 >$ texture components.

The variation of the through-thickness texture was explained in terms of the macroscopic gradients of deformation modes and the temperature profile occurring in these materials during hot rolling. The layers close to the centre were essentially deformed by plane strain. The grains in these layers typically assume an elongated pancake type morphology. Cooling at the centre is much slower than at the surface. Both effects promote dynamic recovery instead of dynamic recrystallization in the centre layers. The as-cast texture $(001) < \mathrm{uv0} >$ of columnar grains is essentially retained by dynamic recovery. A strong α-fibre texture defines the maximum intensity at a $(001)[110]$ texture component in layers that are close to the centre.

However, the surface zones are deformed by shear strains that are induced by slip friction between the fast rotating roll's surface and the slower-moving workpiece's surface. Shear strain deformation stores significant deformation energy within these surface zones. The high deformation energy on the surface causes dynamic recrystallization of equiaxed grains. The shear or Goss texture is evidence that the surface was deformed by shear strain, which is why the surface is characterised by a pronounced intensity of Goss texture together with a $(011)[112]$ texture component.

Raabe and Lucke [54] noted that due to a high accumulation of dislocation energy in the surface zones and which is low at the centre layer of hot-rolled strip, surface recrystallized equiaxed grains have a Goss texture while the centre layer has a non-recrystallized elongated pancake structures with an α −fiber texture. This is because of the shear strain at the surface and plane strain at the centre layer during hot rolling respectively. The inhomogeneity of texture through the thickness of the strip is linked to ridging which causes a poor surface quality of deep drawn steel strip [6]. A surface characterised by shear texture components $\{011\} < 100 >$ and $\{110\} < 112 >$ results from and are stabilised by the shear strain during hot rolling.

2.6.4. Influence of cold rolling and annealing processes on texture evolution in ferritic stainless steel

In cold rolled FSS steel sheets, texture sharpness takes place by inheriting the former hot band texture with domination of α-fiber and γ-fiber texture components while reducing the intensity of the other texture components through the thickness of the strip. When Maruma *et al.* [55] studied the effect of cold rolling and annealing temperatures on texture evolution in FSS, it was found that during cold rolling, hot-band texture components remained stable even when the material was given 82% cold reduction. The material was characterized by a rotated Cube $\{001\} < 110 >$ texture component. This behaviour is attributed to the difficulty of α-fiber texture components ranging from $\{001\} < 110 >$ to $\{112\} < 110 >$ to recrystallize because of their low Taylor Factor (TF), (TF is used to express a flow stress (σ) measured in a polycrystalline material in terms of the critical resolved shear stress [CRSS-τ_{CRSS}], in constituent single crystals. The higher is TF for a certain crystal, the higher is stress required to cause the crystal to slip during material plastic deformation, assuming all crystals in material have approximately similar CRSS, which leads to a high stored deformation energy [39]. However, the γ-fibre texture components have a high TF that enable them to store more deformation energy and readily recrystallize during annealing. Cold rolled FSS sheets therefore tend to have a characteristically homogeneous or heterogeneous texture distribution where α-, γ-fibre, Goss (shear) and even rotated

cube texture components are dominant, depending on the chemical composition of the FSS grade and former rolling schedule.

Zhang *et al.* [45] studied the effect of hot rolled shear bands on the formability and surface ridging of an ultra-purified 21%Cr FSS. The material was hot rolled, cold worked and annealed for texture studies. It was found that the material developed a heterogeneous sharp texture of α-fibre and γ-fibre components with comparable intensity, while the intensity of the α-fibre texture component was 8.51, and that of a γ-fibre component was 7.22, see Fig 2.6.4 (a). The cold rolled α-fibre texture component was inherited from the as-cast columnar elongated dendrites with a {001} <uv0> texture as a mechanism to respond to the effects of the cold rolling process [2].

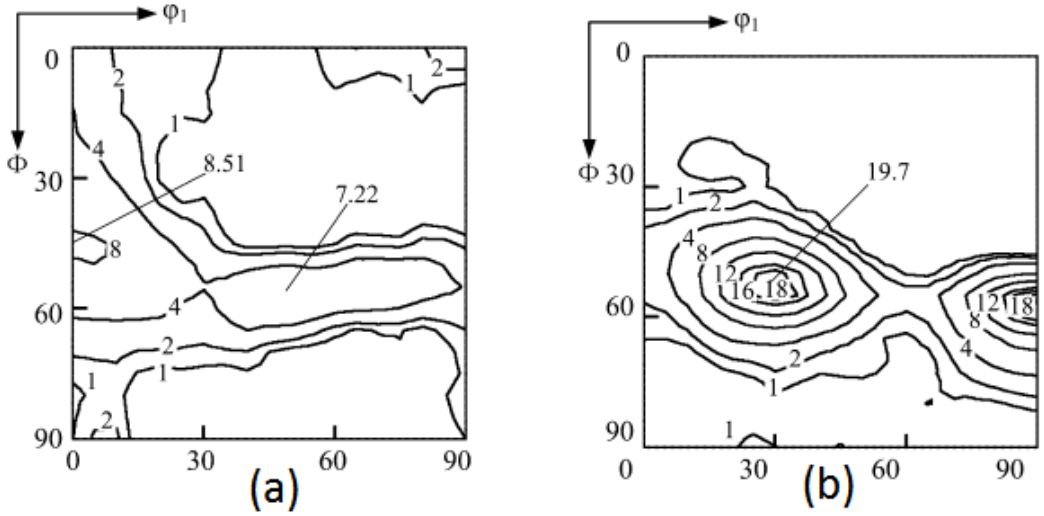

Figure 2.6.4: Typical ODFs at $\varphi_2 = 45°$ showing the effect of cold working and annealing on texture of ultra-purified 21%Cr FSS, (a) 80% cold work (b) annealed at 950°C for 3 minutes [45].

When the cold work texture was annealed at 950°C for 3 minutes (Fig. 2.6.4 (b)) it was found that homogeneous γ-fibre texture components emerged strongly at $\{111\} < 112 >$ and $\{554\} < 225 >$ with 19.7 and 18.0 intensities respectively, while the α-fibre texture components disappeared. The recrystallization texture was attributed to the large amount of deformation energy stored in the {111}-grains, which caused them to recrystallize first during annealing and grow at the expense of the other grain orientations, including the α-fibre texture components.

2.6.5. Influence of precipitation and particle stimulated nucleation (PSN) on texture evolution in FSS

The chemical composition of the steel has substantial effects on the formation of precipitates that influence the formation of the rolling and recrystallization texture. FSS grades that are stabilized by an addition of Ti, Al and Nb alloying elements, form high temperature hard precipitates such as TiN, AlN or NbC during the casting and hot rolling stages. Ti has high affinity for N and forms the TiN precipitate at higher temperatures in the melt and forms TiC in the solid solution phase in the presence of C. However, C is highly reactive with Nb and preferentially forms NbC or Nb(C, N) than Ti to form TiC in solid solution during hot rolling. Nb and Ti tie up the C and N respectively in solid solution, which both preferred nucleation of {111}-texture grains, thus promoting nucleation of the preferred γ-fibre texture components. When deformation occurs in the fields around large (≥ 1 μm) non-deformable particles, a localised higher dislocation density and large orientation gradients are developed around these particles. These fields are preferential sites for nucleation of grains during the recrystallization process. This phenomenon is known as particle stimulated nucleation (PSN) [56, 57, 58].

The PSN mechanism plays a major role during recrystallization for texture and grain refinement and has been studied in Al alloys and some FSSs. Since inclusions are generally harder than the matrix, the matrix surrounding them experience more deformation and, therefore tends to store more deformation energy than other parts of the matrix. Therefore, areas around these inclusions have a higher driving force for recrystallization. Consequently, grains nucleate with random orientation in these regions [59].

Siyasiya *et al.* [58] studied the influence of chemical composition on the evolution of texture in 441 FSSs, and found that an optimal addition of (0.44%Nb + 0.15%Ti) content to the steel improves the γ-fibre texture; notably {111}<112> and {554}<225> texture components were significantly pronounced after recrystallization annealing, see Fig. 2.6.5. No further increase of γ-fiber texture was accomplished by a further addition of (Nb+Ti) to the FSS.

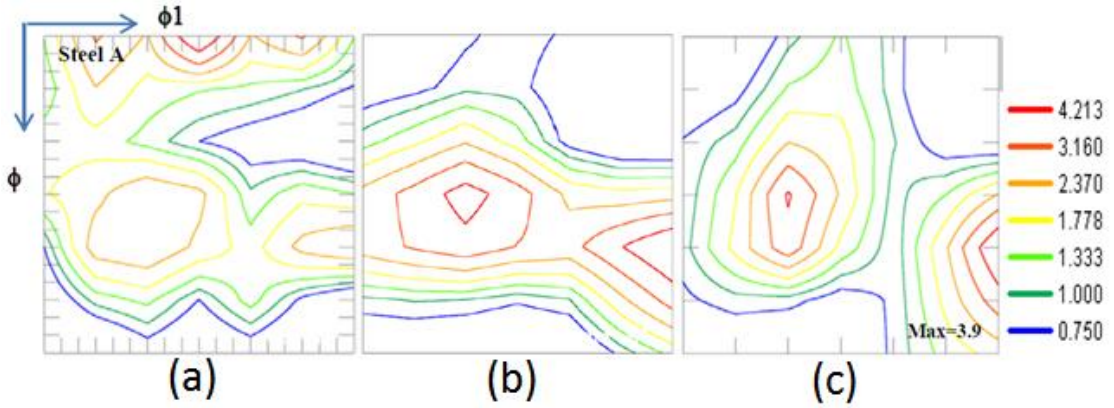

Figure 2.6.5: A typical ODFs at $\varphi_2 = 45°$ showing effect of (Nb+Ti) addition in 441 FSS after 62% cold worked and annealed at 1025°C for 5 minutes, (a) 0.26%Nb+0.2%Ti, (b) 0.44%Nb+0.15%Ti, and (c) 0.70%Nb+0.32%Ti [58].

In a related study it was also found that TiN first nucleates heterogeneously on the $MgO.Al_2O_3$ spinel, followed by Nb(C, N) on the TiN surface, thus resulting in the formation of a complex compound of $MgO.Al_2O_3$-TiN-Nb(C, N). It was concluded that those large and complex particles were responsible for PSN, which was in agreement with De Siqueira *et al* [59, 60].

Lewis *et al.* [61] studied the effects of Mo, Ti and Nb stabilising elements on the development of the recrystallization texture in 17%Cr FSS and its effect on the steel's formability. It was observed that grains with an {111}//ND orientation nucleated at the {α-ferrite phase matrix/Nb(C, N)} particle interface at an early stage of recrystallization. As little as 35% cold reduction of the material was sufficient to induce this recrystallization nucleation. This type of texture nucleates and grows at the expense of other orientations, including α-fibre texture components. The γ-fibre texture intensity increased with a further rolling reduction. The same phenomenon was observed in steels with larger sized particles of TiN, TiC, Nb(C,N) or $M_{23}C_6$. This effect was due to the PSN mechanism, whereby an increased lattice curvature and more stored deformation energy in the presence of large amounts of undissolved particles initiated recrystallization nucleation at the matrix/particle interface [61].

2.7. Ridging roping and formability in ferritic stainless steel

2.7.1. Introduction

Ridging of deformed FSS sheet has been studied for several decades. Many papers have been published for improvement of ridging resistance through optimising the recrystallization texture. Texture and the associated topographical arrangement of grain orientations play an important role in ridging development during forming operations. Ridging models have been proposed to elucidate their formation as a function of the recrystallization texture in FSS sheets that are prone to ridging. Chao-Wright [62, 63, 64], Takechi [66] and Engler [65] all developed models that explain how ridges are formed in association with the crystallographic texture of FSS sheet after a given amount of tensile straining along the RD or deep drawing.

2.7.2. Chao and Wright's ridging model

Chao in 1967, and Wright in 1972 developed models independently that offer a similar explanation for ridging or roping [62, 63, 64]. The writers attribute ridging to the differences in R_m-value of various recrystallization texture components. They found that $\{111\}//\mathrm{ND}$ −oriented grains have a higher R_m-value than the $\{001\}//\mathrm{ND}$ −oriented grains. Thus, during tensile straining along the RD, the $\{111\}$ −oriented regions will become larger in thickness than the average grains along the ND, and will be associated with ridge formation on the sheet surface. The $\{001\}$ −oriented regions on the other hand, will become smaller in thickness than the average grains along the ND and will form troughs, thus forming ridging or roping on the sheet surface.

Fig 2.7.1 is the schematic illustration of the model explaining ridging in terms of local variations of strain through the thickness of the deformed sheet in the direction X_3.

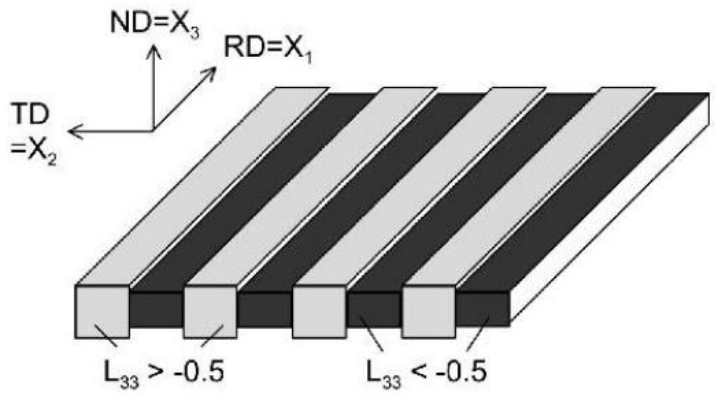

Figure 2.7.1: Schematic drawing of the occurrence of ridging due to local variation in strain rate in the through-thickness of deformed sheet [65].

L_{33} denotes gradient components of banded grains during tensile straining. The $\{111\}$ −bands deform less than the matrix and result in $L_{33} > -0.5$, thus ridge formation on the sheet surface along the ND. In contrast, when $\{001\}$ −bands deform more than the matrix, they yield ($L_{33} < -0.5$) along the ND, hence, leading to trough formation on the sheet's surface.

2.7.3. Takechi et al.'s ridging model

Instead of focusing on the local strain rate variation through the thickness, Takechi *et al.* [66] focused on the local variation in out-of-plane shear rate of the deformed sheet. The reasoning behind this was

that shear of $< 110 >//\mathrm{RD}$ −fibre would move out of the sheet surface plane in TD during forming operations. The schematic drawing in Fig. 2.7.2 below illustrates the model.

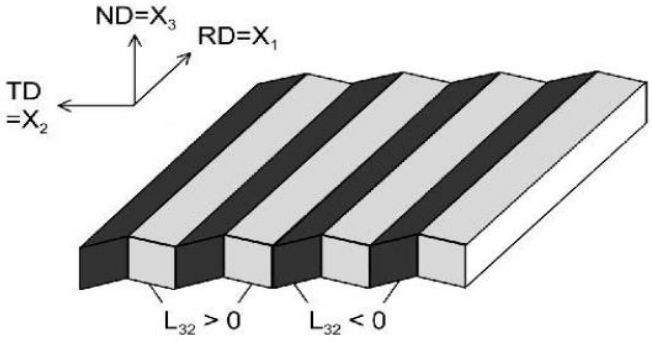

Figure 2.7.2: Schematic drawing of the occurrence of ridging due to local variation in shear rate out of plane of deformed sheet [66].

Here L_{32} denotes a shear-rate component of deforming bands. The two symmetrically positioned bands of orientations (clustering of grains with similar orientations), namely $\{111\} < 110 >$ and $\{112\} < 110 >$, show different opposite signs of the shear rate (L_{32}), i.e. opposing out-of-plane shear. The $\{111\} < 110 >$ −bands will result in $L_{32} > 0$ (ridge) and $\{112\} < 110 >$ −bands in $L_{32} < 0$ (trough) forming under the tensile strained sheet, or *vice versa*. This behaviour may lead to significant surface roughening on the free sample surface.

2.7.4. Engler et al.'s ridging model

Engler *et al.* [65] modified the ridging model of FSS postulated by previous authors on grounds that the ridging model cannot provide a viable explanation for the ridging mechanism based on the deformation of individual grains because the amplitude of ridges ranges between 0.5 and 1 mm, which is considerably larger than the average grain size of 10-20 µm. The stochastic effect of topographic (heterogeneous) orientation distributions that can be obtained through EBSD should be considered instead. The authors employ a model that uses as an input large-scale (1.8 mm X 3.6 mm) EBSD maps and gives an output of local variation of strain-rate components of both individual and clustered grains (colonies). The model can also analyse the variation of macroscopic strains from band to band that are aligned parallel to the RD and relate to ridging. Fig. 2.7.3 below shows some EBSD maps defining texture banding or colonisation.

The self-consistent, polycrystalline visco-plastic (VPSC) model is based on the orientation-dependent anisotropy of plastic deformation. This model can characterise and simulate ridging using EBSD [65]. The model output suggests that $\{001\}//\mathrm{ND}$ −oriented grain colonies are deformed under uniaxial tensile stress along the RD. The colonies have very low l_{33} −values (velocity-gradient tensor during tensile deformation) along the ND, which is less than the velocity-gradient tensor of average grains ($L_{33} \cong -0.5$), i.e. the colonies deform more than the average, implying they will be thinner than average in the ND and will be in proportion to the troughs in the sheet surface.

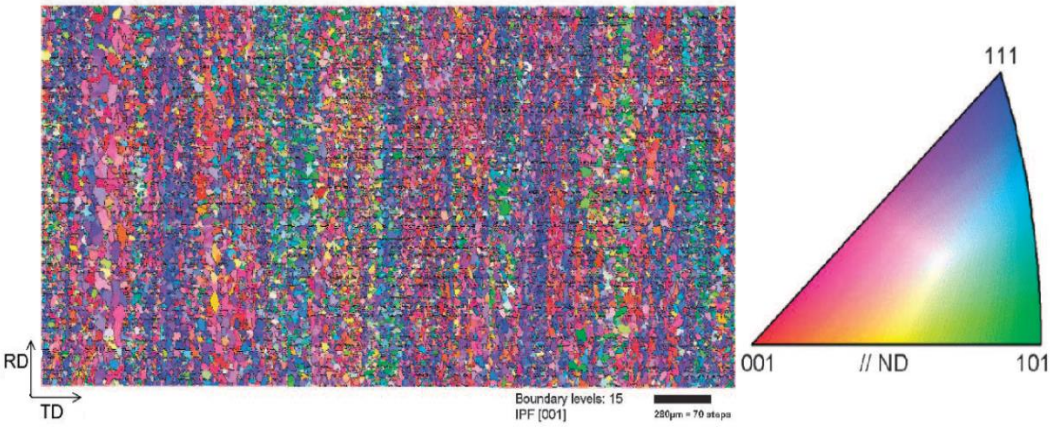

Figure 2.7.3: EBSD maps of processed FSS sheet taken from mid-layer surface, used as input data into visco-plasticity self-consistent (VPSC) model [65].

On the other hand the l_{33} −value of $\{111\}//\mathrm{ND}$ −oriented colonies is higher than the L_{33} −values, i.e. $l_{33} > L_{33}$. These colonies will deform less than the average along the ND, forming ridges on the sheet surface through tensile straining.

$$L = \begin{pmatrix} L_{11} & L_{12} & L_{13} \\ L_{21} & L_{22} & L_{23} \\ L_{31} & L_{32} & L_{33} \end{pmatrix} \cdot \dot{\varepsilon}$$

Equation: 12

Figure 2.7.4: Velocity gradient tensor matrix of average grains defined as a function of strain rate (**ε̇**) in a visco-plasticity self-consistent (VPSC) model [65]

These findings are consistent with the model developed by Chao [62, 63] and Wright [64] who explained ridging in terms of differences in the R_m-values between the various recrystallization texture components ($r = \frac{l_{22}}{l_{33}}$) in 2D as a function of recrystallization texture components obtained from EBSD maps.

2.7.5. Effect of texture on formability of ferritic stainless steel

Formability of metal sheet is the ability of a given blank sheet of metal alloy material to undergo plastic deformation (deep drawn, forged, stamped, shaped) without being fractured or damaged (tearing, earing or ridging and other formation of surface effects). By means of the Lankford-value or average strain ratio ($\bar{r}$), the formability of a metal sheet can be quantified.

The Lankford-value ($\bar{r}$) is defined by equation 13 given below:

$$\bar{r} = \frac{(R_{0^\circ} + 2\,R_{45^\circ} + R_{90^\circ})}{4}$$

Equation: 13

Where the variables are: R_{0° is a strain ratio of a tensile test specimen parallel to, R_{45° is a strain ratio of the tensile test specimen at a 45˚ angle of, and R_{90° is the strain ratio of the tensile test specimen at a 90˚ angle of, the RD of the metal sheet.

The strain ratio R of each of the three tensile specimens is defined by equation 14:

$$R = \frac{\ln\left(\frac{W_0}{W}\right)}{\ln\left(\frac{W\,L}{W_0 L_0}\right)}$$

Equation: 14

Where W_0 the width of the tensile test specimen before being strained in tensile test, W is the width of the tensile specimen after being strained by a given amount in the tensile test, L_0 is the original gauge length of the tensile specimen before strained, L is the gauge length of the tensile test specimen after being strained to a given amount.

The Lankford-value leads to the limiting drawing ratio (LDR), LDR is an indicator of material formability, which is defined as the ratio of the maximum blank diameter of metal sheet that can be safely drawn into a cup without flange to the punch diameter [67]. Fig.2.7.5 shows typical results of the LDR versus average strain ratio.

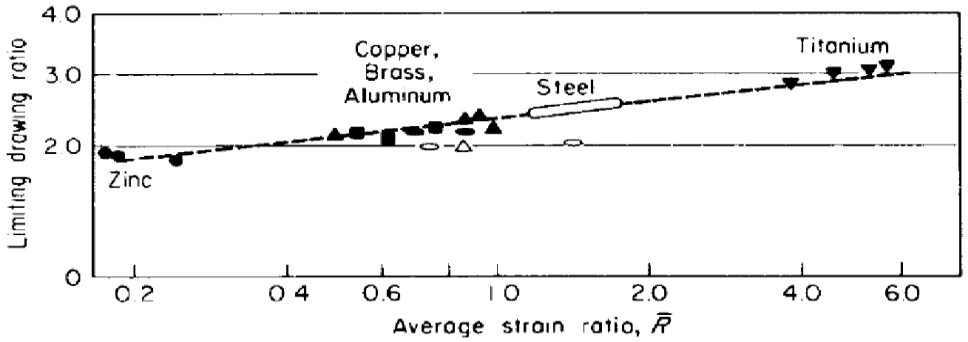

Figure 2.7.5: Correlation between the limiting draw ratio (LDR) and average strain ratio ($\bar{\mathbf{R}}$-value) for some sheet materials [56].

Fig. 2.7.5 above shows that the higher the average strain ratio ($\bar{R}$-value or $\bar{r}$), the higher the LDR of the sheet, and hence the better the formability of the sheet material. Texture determines the plastic anisotropy of the material.

Hamada *et al.* [68] observed that the crystallographic texture affects the average strain ratio ($\bar{r}$) of FSS sheets, which is a function of plastic deformation and, therefore, leads to an anisotropic property. The planar anisotropy of the strain ratio and average strain ratio of FSS sheets with uniformly distributed γ –fibre texture components, are characterised by a higher average strain ratio ($\bar{r}$) than is found in an inhomogeneous texture distribution where γ –fibre and α –fibre textures predominate.

The inhomogeneous texture distribution has a negative effect on the average strain ratio value ($\bar{r}$) and therefore impairs the sheet's formability. The presence of any texture components other than the γ –fiber texture components, lowers the average strain ratio ($\bar{r}$) of the FSS material. High formability is attained from a homogeneous distribution of the recrystallized γ –fibre texture components [69].

Chapter 3: Experimental approach

3.1. Description of the material

A continuously cast slab sample of 433 FSS with both equiaxed and columnar solidification structures was supplied by Columbus Stainless Steel, see Fig. 3.1.

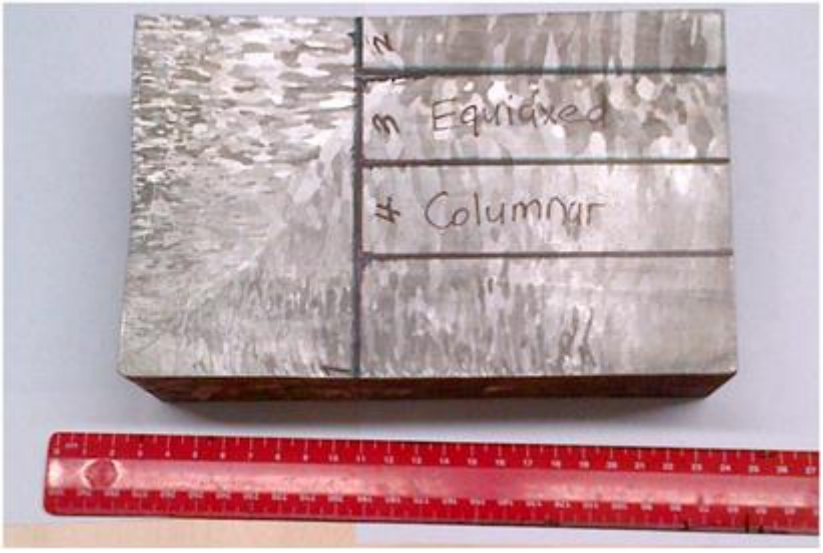

Figure 3.1: AISI 433 block steel sample from Columbus stainless steel.

The steel block was then surface ground down to 2400 grit SiC and macro-etched using Aqua-Regia solution. Two steel blocks of approximately separated wholly equiaxed and other columnar as-cast structures were mechanically obtained from the given block with equal dimensions, 122 mm long, 53 mm wide and 25.5 mm thick as shown in Fig. 3.2, and were designated initial equiaxed cast structure (IECS) and initial columnar cast structure (ICCS).

Figure 3.2: IECS and ICCS sample blocks of 433 FSS after mechanical separation.

3.2. Chemical composition

Chemical composition of the 433 steel that was studied is given in mass percentage in Table 1.

Table 1: Steel chemistry of 433 FSS in wt% balance of Fe

C	N	Cr	Ni	Mn	Si	Cu	V	Al	Nb	P	Co
0.048 max	0.037	16.400	0.160	0.510	0.290	0.090	0.120	0.261	0.002	0.023	0.090

3.3. Rolling Procedure

The thermo-mechanical processes, namely hot rolling, cold rolling and annealing were simulated according to the industrial schedules for the production of 433 FSS sheets of 1.5 mm thickness. The addition of an intermediate annealing of the hot band before cold rolling was done to study the effect of hot band annealing on the final texture. The intermediate annealing step is not standard practice in this plant. A flowchart of the rolling and annealing processes is given in Fig. 3.3.

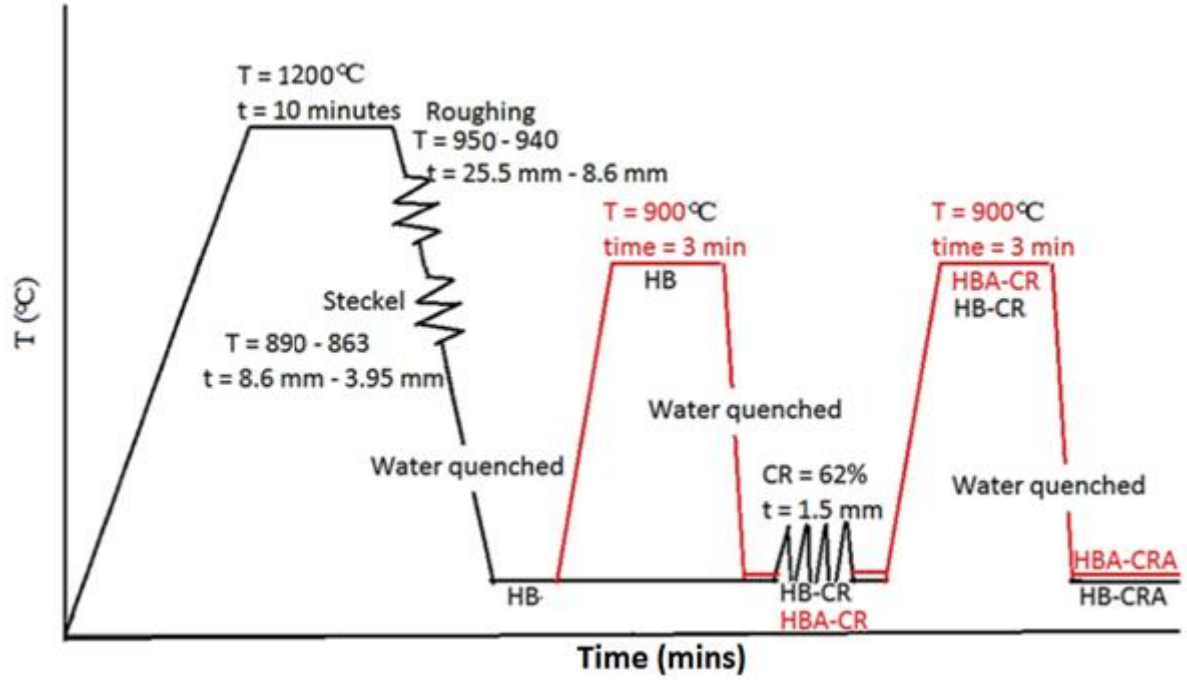

Figure 3.3: Thermo-mechanical processes diagram; hot band (HB), hot band annealed (HBA), hot band-cold rolled (HB-CR), hot band annealed cold rolled (HBA-CR), hot band annealed cold rolled annealed (HBA-CRA) and hot band-cold rolled annealed (HB-CRA).

3.3.1. Simulated rough rolling

The steel blocks were heated at 1200°C for an hour to homogenise the temperature across the whole cross-section of the samples shown in section 3.1 of the material's description. The blocks were then soaked at 1200 °C for 10 mins in a laboratory furnace and were then cooled down to a hot rolling starting temperature of 950 °C. The hot rolling operation was performed at a temperature of 950 °C to 940 °C. The blocks were given the last three passes of the seven rough-mill passes in the plant from a 25.5 mm thickness hot rolled down to a sheet thickness of 8.6 mm and water quenched to room temperature to avoid Laves phase formation. Samples for metallurgical analysis were withdrawn before the simulated "Steckel"-rolling.

3.3.2. Simulated "Steckel" (finishing rolling)

After roughing, the material was soaked at 1200 °C for 30 minutes then cooled down to a finishing entry temperature of 890 °C. The hot band was given three passes to achieve a thickness of 3.95 mm at an exit temperature of 870 ℃ and thereafter water quenched.

3.3.3. Intermediate annealing

The hot band (after hot rolling) was annealed at 900°C for 3 minutes and water quenched. This was done in order to fully recrystallize the partially recrystallized hot band, which could possibly alter the texture.

3.3.4. Cold rolling

Both were directly rolled, hot band (HB) and the intermediate annealed strip (HBA), by subjected to 62% cold reduction. The final thickness was 1.5 mm.

3.3.5. Annealing of material

After cold rolling, the specimens for HB-CR and HBA-CR were annealed at 900°C for 3 minutes and water quenched. Samples for texture and microstructural analysis were collected at every processing stage.

3.4. Metallographic analysis

The microstructure of the rolled sheets was studied using the following techniques:

- SEM-EBSD: to generate IPF and ODF's crystallographic texture; and
- XRD : to study the bulk crystallographic texture

3.4.1. Scanning electron microscopy's electron backscattering diffraction (SEM-EBSD)

A surface area of 10 mm (TD) X 15 mm (RD) from RD-TD plane was machined and hot mounted in black resin. The samples were ground, diamond polished to 1 µm and then further polished with oxide particle suspension (OPS) to minimize surface defects that were induced by mechanically polishing forces. Electro-polishing for further surface preparation was avoided since it caused surface relief and shadow effects during SEM analysis. All the sample preparations were done based on standard metallographic sample preparation procedures. The RD-TD plane was preferred over the typical RD-ND plane in order to be able to compare near surface, quarter and center plane texture of the hot bands over a larger area of about 3 mm (RD) X 4 mm (TD).

The samples were studied using a SEM:FEI Nova NanoSEM model configured with Oxford EBSD:EDAX Digiview 3 EBSD Camera instruments. The accelerating voltage was set at 15 kV and the probe current at $7 \text{ X } 10^{-9}$A. The orthorhombic sample holding system, which is defined by the RD, ND and TD, was tilted with its surface at an angle of 70° between the RD-axis and the electron beam's incidence axis, to allow more diffracted electrons to reach the EBSD detector. The scans were done over an area of 3 mm (TD) X 2 mm (RD) with a step size of 2.5 µm at a magnification of 100X. At least 1000 grains were scanned on a given surface area using combo-scan (stage and beam scanning) to ensure a good statistical texture representation. Grain boundaries were analysed by using EBSD raw data that were

processed further using EDAX-TLS software, and phase identification was done by using Orientation Image Mapping (OIM) software after indexing Kikuchi band patterns.

During data acquisition, at least seven Kikuchi bands were used to index a pattern to ensure reliable results and EBSD patterns having an average confidence index greater than 0.1 permitted a 95% confidence interval. A time average confidence index of the patterns was above 0.45 during this experiment, which led to more than 96% of the patterns being indexed correctly in every case.

Orthorhombic sample symmetry was applied and orientations were expressed in Euler angles such that the angles are within the following range $0° \leq (\varphi_1\ ,\ \Phi\ ,\ \varphi_2) \leq 90°$ with a 10˚ Gaussian half-width spread around the ideal orientation. The ODFs were then calculated using the series expansion method (L_{max} = 22) with 5˚ clustering angle from the raw data obtained from the EBSD. The crystallographic texture was presented in ODFs at a section $\varphi_2 = 45˚$ since this contains important rolling and recrystallization texture of rolled bcc metals and their alloys. The software was set up to define a grain as an area that has an angular difference of at least 5° between the adjacent lattice areas during grain size measurement. The choice of 5° was considered so that boundaries that would be within a range of 5°< Φ< 12° for LAGB and a range of Φ>12° for HAGB are defined and avoid localised misorientation within a grain/crystal if a misorientation of less than 5° was selected.

The texture gradient through the thickness of the strips was studied at the surface, mid-surface and centre of the transfer bar samples, surface and center of hot band samples and near center of cold band and annealed samples withdrawn from the various stages of the thermo-mechanical processing. Texture was presented in ODFs Bunge notation sectioned at $\varphi_2 = 45˚$.

The “s” defines the depth of the layer where the texture was measured and is given by equation 15 [8].

$$s_n = (1 - x) * t$$

Equation: 15

Where:

- s layer at texture is measured
- x fraction of material thickness that is removed by wet grinding
- t is the final gauge thickness of each rolling stage

- Transfer bar samples thickness t = 8.46 mm
- Hot band (HB) and annealed hot band (HBA) t = 3.95 mm
- HB-CR, HB-CRA, HBA-CR and HBA-CRA t= 1.51 mm

The examined texture layers were prepared as follows:

- s_1 = (1-0.12)*t near surface layer texture
- s_2 = (1-0.25)*t mid layer texture
- s_3 = (1-0.50)*t near center layer texture

3.4.3. X-ray diffraction’s (XRD) bulk texture analysis

Sample preparation was the same as for SEM-EBSD analysis except polishing stage. The XRD technique was used to measure the macro-texture. The measurements were performed on the Phillips Analytical X’Pert PRO diffraction system equipped with an Open Eulerian Cradle, in the θ–θ configuration with a mini-proportional detector and fixed collimator point focus and programmable receiving slit. The diffractometer was equipped with a Co $K_{-\alpha}$ radiation source (λ=1.789Å) and the X-ray source was operated at 30 mA and 50 kV.

Three pole figures at the following planes, namely {110}, {200} and {211} were measured according to the Schulz reflection method. These pole figures were measured by recording the intensity distribution of a single {hkl} reflection plane by tilting and rotating the sample over an orientation sphere. Background intensities were measured next to the diffraction peaks with an offset 2θ of 4˚ angle to ensure suitable diffraction patterns.

The XRD-pattern's raw data were used to calculate ODFs using the Gaussian series of expansion method (I_{max} = 22) in MTex software that operates on the Matlab platform, to the obtain orientation-distribution function's (ODFs) texture representation. The section $\varphi_2 = 45^{\circ}$ ODFs Bunge notations were extracted to present rolling and recrystallization textures.

The texture gradient through the thickness of the sheet/strip was studied at the near surface, mid-layer and near centre of the steel sheet/strip.

3.5. Mechanical tensile testing

HB-CRA tensile test specimens along the RD were prepared according to the ASTM A 370 standard. The shape and dimensions of the tensile specimen are shown in Fig.3.5 and Table 2 respectively.

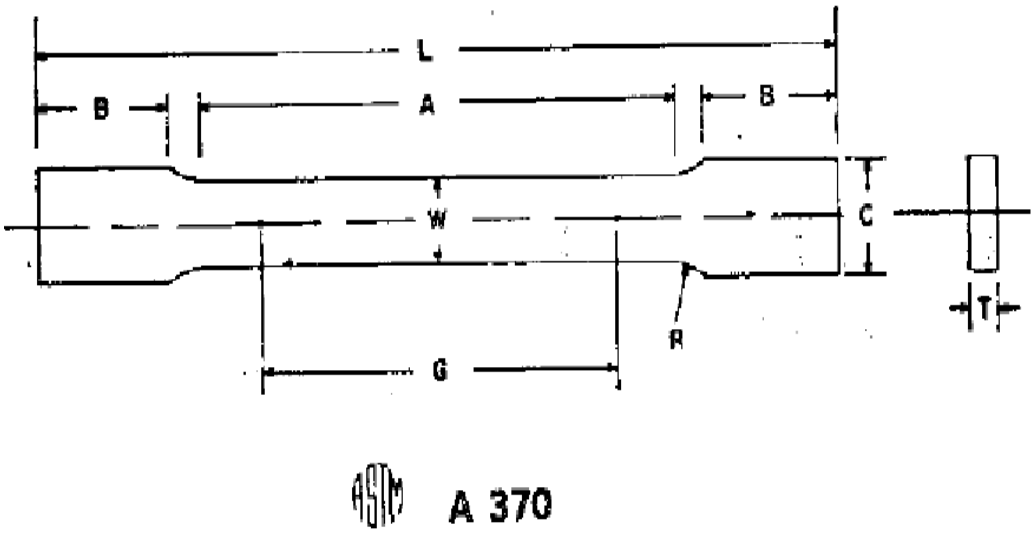

Figure 3.5: Schematic diagrams of the tensile test specimen according to the ASTM A 370 standard.

Table 2: Dimension of the tensile test specimen according to ASTM A 370 standard

Dimension	Value (mm)	Tolerance (mm)
G	50	± 0.10
W	12.5	± 0.25
T	1.5	
R	13	
L	200	
A	60	
B	50	
C	20	

The tensile tests were done at room temperature at a crosshead velocity of 2mm/min. The uniaxial tensile stress was applied along the RD using an Instron universal tensile tester model no 1175 of 1 ton capacity and is shown in Fig. 3.6 below. Three specimens from IECS and ICCS, HB-CRA samples were tested. Mechanical properties were determined and presented as average values of yield strength (MPa), ultimate tensile strength (MPa) and percentage elongation (%).

Figure 3.7: Instron-1175 Universal Test Machine used to determine mechanical properties.

3.6. Surface roughness

HB-CRA, IECS and ICCS samples were machined into tensile-test rectangular shapes of 300 mm (RD) X 10 mm (TD) in the RD-TD plane. They were ground and diamond polished on their gauge lengths to 1 μm to ensure a smooth surface finish before 10% tensile straining, see Fig. 3.8.

Figure 3.8: Surface roughness of unstrained HB-CRA specimen, 1 μm polished surface and TD sampled.

The surface roughness was measured using a Talysurf 120 (Taylor Hobson) Stylus Profilometer; see Figure 3.9. The surface roughness was mapped by measuring the roughness along the TD, i.e. across the width of samples. Twelve sampling lengths (lr) across the width of 10 mm each, with six on the front surface and the other six on the back surface of the specimen, were measured. The average of the surface roughness parameter values was calculated. The measurements were first done before straining the samples, i.e. at 0% tensile elongation, and then again after 10% tensile elongation. The specimens were afterwards observed under the optical microscope.

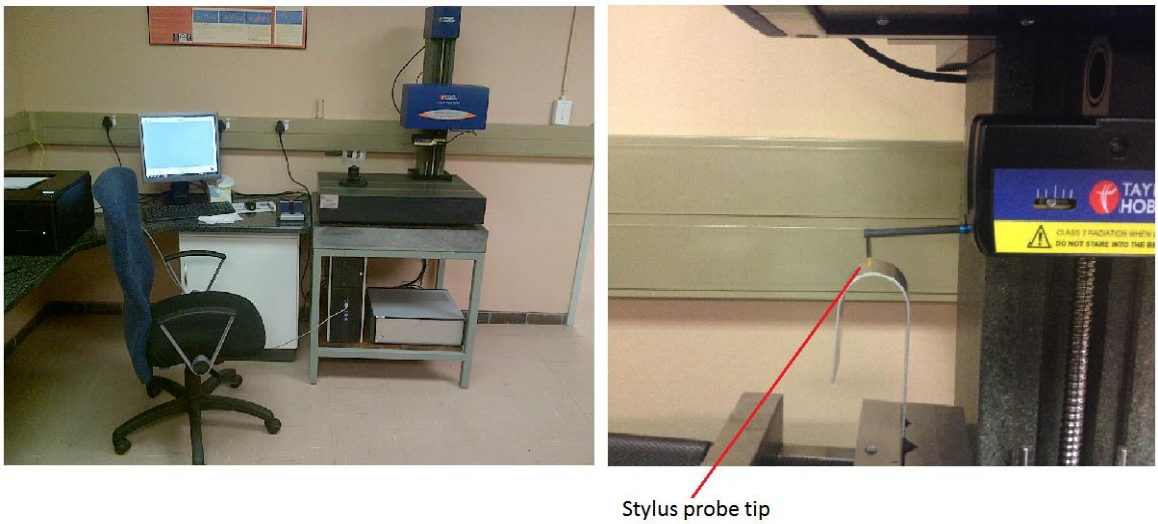

Figure 3.9: Profilometer used to measure surface roughness (sample not from this study).

The surface roughness parameters that were measured are as follows [70]:

a. Maximum profile peak height, denoted by R_p: This parameter defines the largest profile peak height within the sampling length (lr).
b. Maximum profile valley depth, denoted by R_v. This defines the largest profile valley depth within the sampling length (lr). It is the depth of the lowest point on the profile from the mean line (R_a).
c. Maximum height profile, represented by R_z. R_z is the sum of the maximum profile peak height and maximum profile valley depth within the sampling length, i.e. $R_z = R_p + R_v$. R_z is used on all surface textures measured to assess how texture of the surface evolved.
d. Arithmetic mean deviation of roughness profile, R_a. It is the arithmetic mean of the R_z within lr. R_a-value can vary considerably without affecting the performance of the surface and is used to specify an acceptable roughness on the surface.
e. Mean width of the profile elements, RSm. It is the average value of the profile elements' width within the lr.
f. Material ratio of the surface roughness profile, Rmr(c). It is the ratio of the bearing length to the evaluated length (ln = 5*lr) and is expressed as a percentage. The bearing length is the sum of the section length obtained by cutting the surface roughness profile with a line drawn parallel to the mean line (R_a) at a given length. Therefore, if the c = R_P then Rmr (R_P) is 0%, or if c = R_v then Rmr (R_v) is 100% and if c = R_a then Rmr (R_a) is 50%, i.e. the material ratio normally used in making the surface design.

Chapter 4: Results

4.1. Introduction

In this chapter, the results of the microstructural evolution during thermo-mechanical processing are presented in optical and EBDS micrographs, supplemented with grain boundary character distribution (GBCD) graphs. Texture results of each rolling stage are discussed in detail in terms of ODFs that were obtained by using SEM-EBSD and XRD techniques. Results also present the effect of recrystallization texture on surface roughness of HB-CRA materials by using optical micrographs and surface roughness profiles that were obtained with the aid of a Stylus Profilometer. Mechanical properties of HB-CRA steels were assessed to understand the effects of recrystallization texture on the formability of rolled and annealed (HB-CRA) steel sheets.

The results are divided into four sections:

- First will be the effect of hot, cold rolling and annealing on the microstructural evolution of IECS and ICCS samples.
- Second will be the texture evolution during hot, cold rolling and annealing of IECS and ICCS.
- Third will be the effect of recrystallization texture of IECS and ICCS on surface roughness of final rolled and annealed (HB-CRA) steel sheets.
- The last section will relate recrystallization textures of IECS and ICCS specimens with the mechanical properties of (HB-CRA) steel sheets

4.2. Effects of thermo-mechanical processing on micro-structural evolution in IECS versus ICCS

Microstructural analyses were carried out by using a scanning electron microscope (SEM). The EBSD inverse pole figures (IPFs) micrographs and grain boundary character distribution (GBCD) graphs were taken normal to the rolling plane (RD-TD) of all rolled steel sheets.

4.2.1. Analysis of microstructures after rough rolling

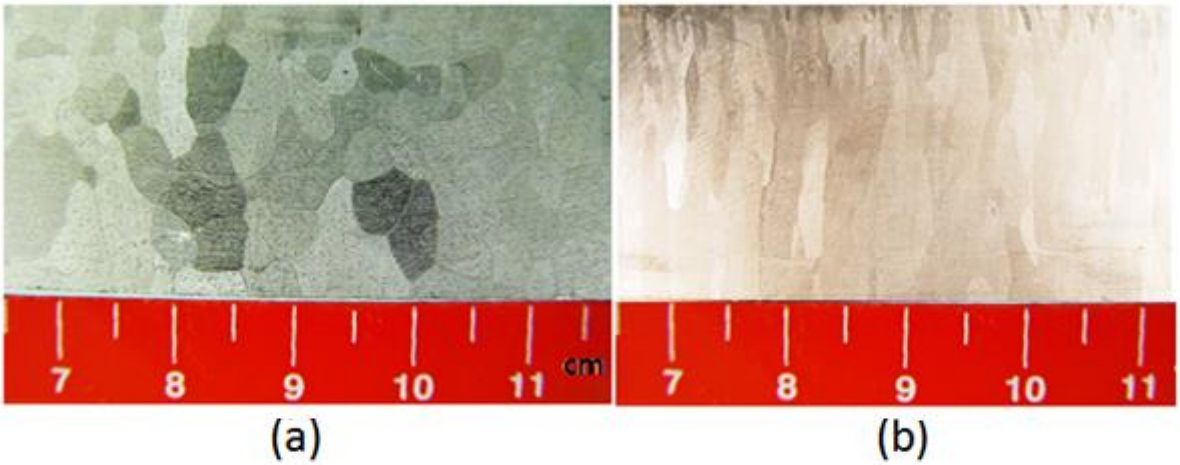

Figure 4.2.1: Macrostructures of the as cast slab revealing the solidification structures, (a) IECS and (b) ICCS.

The as cast structures shown in Fig 4.2.1 above, i.e. IECS and ICCS, were obtained from 200 mm thickness slab after macro-etching with Aqua Regia (1:3, HNO_3:HCl) solution. The initial grain sizes of IECS and ICCS were in macro-scale, as depicted in Fig 4.2.1 before hot rolling. Thereafter, both

materials were given a similar hot rolling treatment in order to study their microstructural and texture evolution during simulated hot rolling stages. The roughing hot rolling micrographs taken from near the surface and center of the rolling plane are presented in Fig, 4.2.2 and Fig 4.2.3 respectively. The micrographs are in the form of IPFs and with their corresponding GBCD graphs of both IECS and ICCS samples throughout the results, were all generated from the corresponding EBSD data.

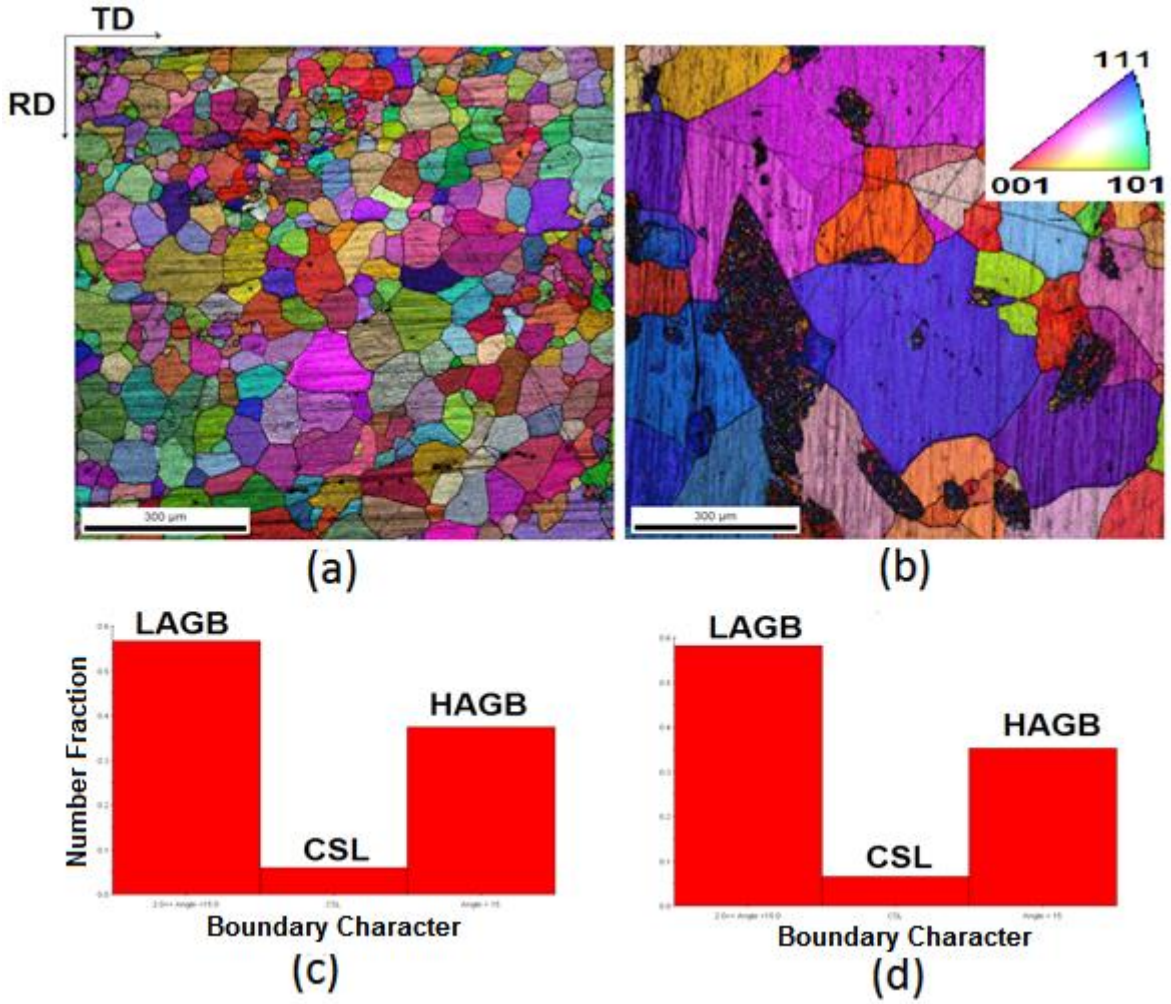

Figure 4.2.2: EBSD maps at the near surface-layer in the RD-TD plane after roughing hot rolling (a) IECS and (b) ICCS and corresponding GBCD graphs for (c) IECS and (d) ICCS specimens.

At the near surface of the IECS specimens, see Fig 4.2.2 (a), the microstructure partially recrystallized into a smaller grain size than the as-cast grains in Fig 4.2.1 (a). Some of the smaller grains were clustered, resulting in a non-uniform distribution of grain size across the matrix. A majority of grains were in the (101)-orientation, as shown in a green colour and others were between (001), red colour and (101)-orientations while (111)-oriented grains are in the minority. The average grain size was found to be 113±14 µm which were measured at a cut-off angle of at least 5° misorientation and above in all analyses. The grain orientations seemed to be uniformly distributed across the matrix.

Contrary to the findings in the IECS, in the ICCS the grain size appeared larger except within the prior austenite grains where complete recrystallization took place due to their low stacking fault energy, which formed finer sub-grains; see Fig 4.2.2 (b). The grain orientations were uniformly distributed across the matrix. The average grain size was found to be 142±28 µm, and was larger than that of the IECS. Partial recrystallization of the hot rolled as cast structures occurred in both IECS and ICCS during roughing hot rolling.

The GBCDs present a lower HAGBs fraction than LAGBs fraction for both IECS and ICCS in Fig 4.2.2 (c) and Fig 4.2.2 (d) respectively below. However, the IECS specimens exhibited a slightly higher fraction of HAGBs than in the ICCS specimen. The GBCDs support the observations that were made in the IPFs microstructures of recrystallized grains on both steels, i.e. the occurrence of partial recrystallization in both steels.

The microstructures obtained from the centre are given in Fig 4.2.3 and are similar to those of the surface, i.e. almost uniform grains for the IECS specimen and clustering of small grains in the ICCS specimen. However, GBCD graphs show that less recrystallization took place at the center than in the near-surface, i.e. a reduction from the fraction of LAGBs which is larger than that of the near-surface given in Fig 4.2.2 (c) and (d) above.

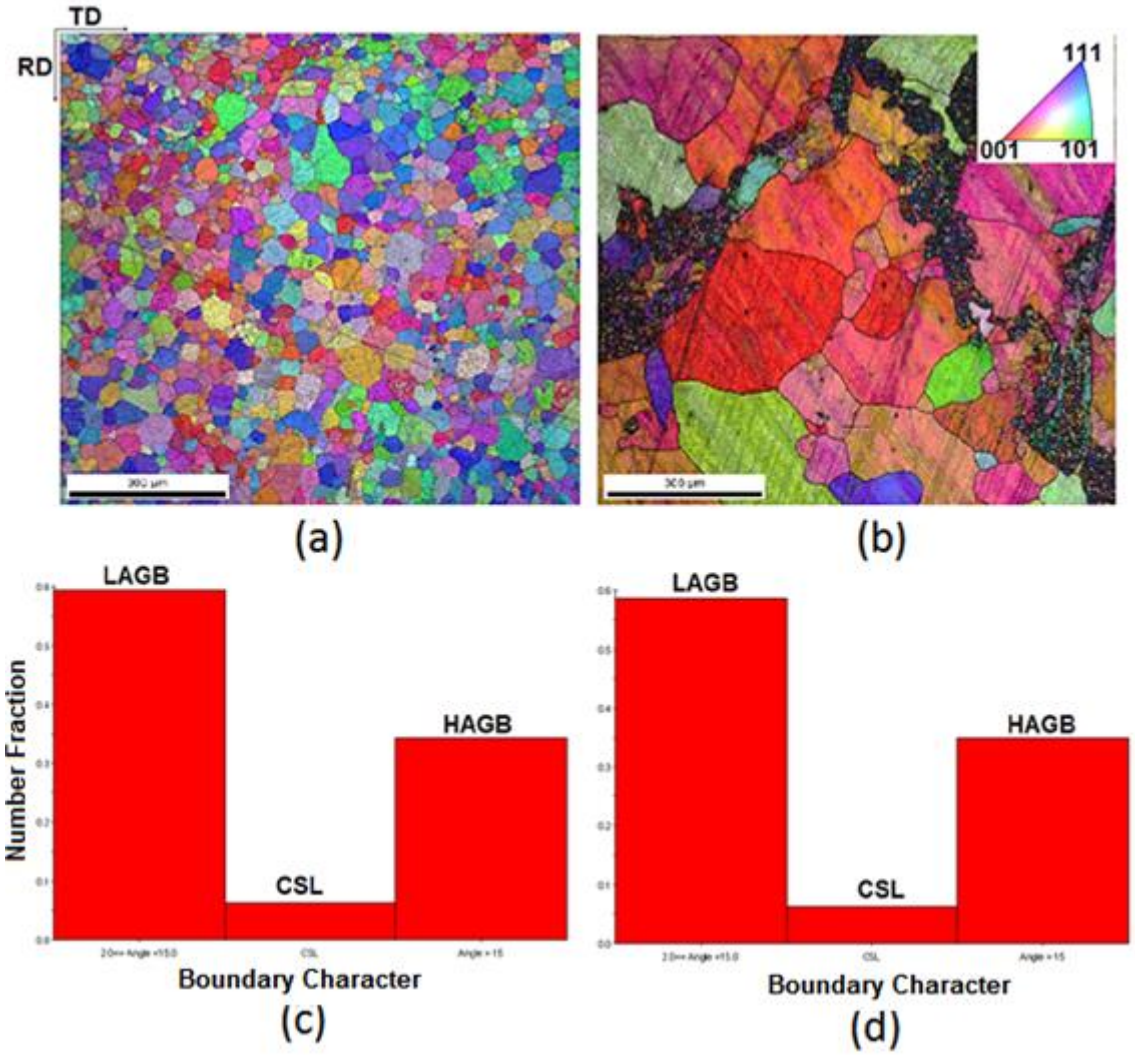

Figure 4.2.3: EBSD maps at near centre-layer in the RD-TD plane after roughing hot rolling for the specimens of (a) IECS and (b) ICCS and corresponding GBCD graphs for (c) IECS and (d) ICCS specimens.

In terms of grain orientations, the IECS specimen was dominated by {001}-oriented grains (red-colour) and followed by {101}-oriented grains (green-colour) and {111}-oriented grains (blue-colour) across the matrix. Nevertheless, the ICCS specimen had larger grains that were (001)-oriented and seemed to dominate across the matrix. The orientations of the fine grains in prior austenite regions were not well resolved.

4.2.2. Analysis of hot band microstructures

As may be seen in Fig 4.2.4, the EBSD map, which was taken near the surface, revealed partially recrystallized grains again after finish hot rolling. As the temperature decreased from roughing to the finishing temperature, there was more recovery than recrystallization in both specimens of IECS and ICCS, see the GBCD graphs in Fig 4.2.4. (c) and (d), i.e. the HAGB fractions of the IECS and ICCS specimens were found to be 0.21 and 0.17 respectively and were lower compared to those found in the roughing stage, which were 0.37 and 0.35 respectively. Furthermore, the HAGB fraction within the IECS specimen (0.21) was higher than that in the ICCS specimen (0.17) and this suggested that there was more dynamic recrystallization (DRX) in the specimen of IECS than in that of the ICCS during finish hot rolling. Although the grain size could not be measured accurately at this stage, the ICCS specimen's microstructure remained coarser, even after finish mill rolling.

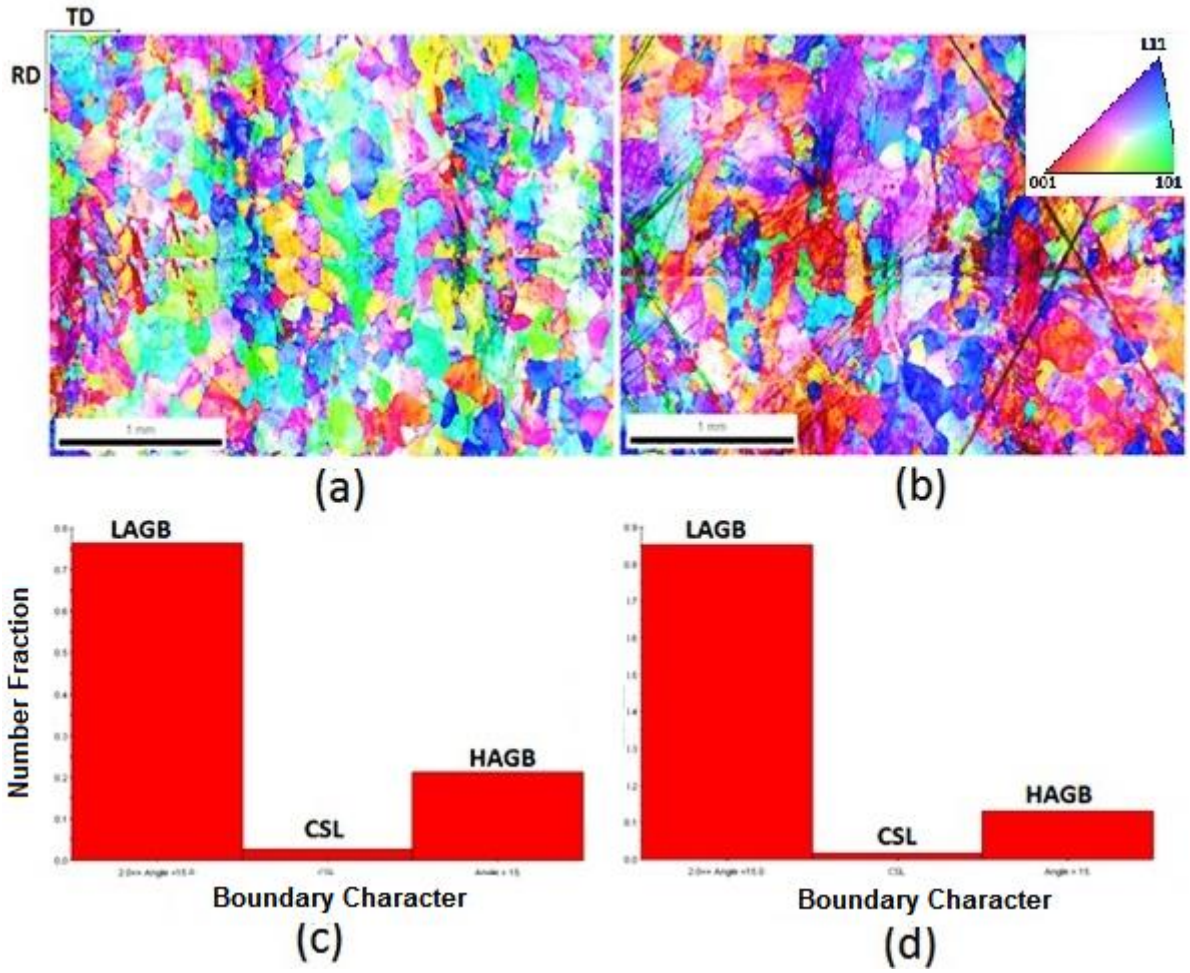

Figure 4.2.4: EBSD maps in the near surface-layer in the RD-TD plane after finish hot rolling of the specimens from the (a) IECS and (b) ICCS and corresponding GBCD graphs for (c) IECS and (d) ICCS specimens.

The grain orientations developed differently between the IECS and ICSS steels. On the one hand, the IECS specimen in Fig 4.2.4 (a) exhibited a domination of green (101)-oriented grains followed by a colour close to red (001)-orientation. The (101) and (001)-orientations are components of shear (Goss) and Cube or rotated Cube texture respectively. On the other hand, the ICCS specimen in Fig 4.2.4 (b), was characterized by red (001)-oriented grains with a few blue (111)-oriented grains. The (111)-orientation is a component of the γ –fibre texture.

The EBSD scans were also done on the hot band center to assess the microstructure and texture gradients through the thickness of two respective hot bands, see Fig 4.2.5. A similar trend was observed as with the surface except that the Cube texture (001) increased its intensity and largely in specimen ICCS at the expense of the (101) Goss texture, see Fig 4.2.4 (b) and Fig 4.2.5 (b). At the center, the microstructures were coarser than those in the near-surface and as expected, those of the ICCS specimen was coarser than that of the IECS specimen.

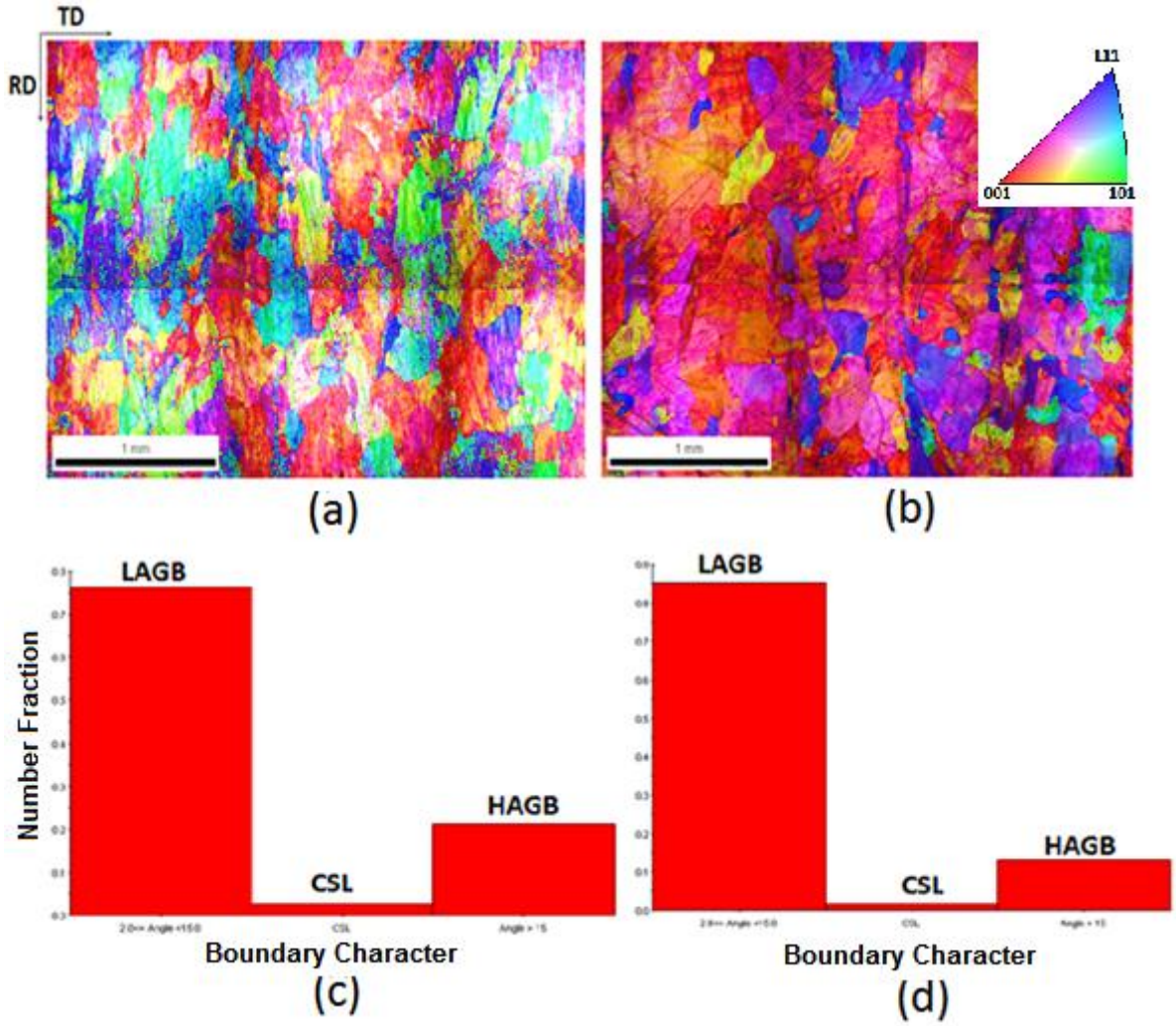

Figure 4.2.5: EBSD maps at near centre-layer in the RD-TD plane after finish hot rolling of the respective specimen (a) IECS and (b) ICCS and corresponding GBCD graphs for (c) IECS and (d) ICCS specimens.

The elongated grains in Fig 4.2.5 (a) are a characteristic associated with rolling and dynamic recovery and follows from a suppressed recrystallization microstructure's softening mechanism during or after hot rolling. The ICCS specimen's structure was dominated by the Cube texture; see Fig 4.2.5 (b). As expected, the GBCD maps revealed that little recrystallization had taken place at the center.

4.2.3. Analysis of annealed hot band (HBA) microstructures

Both IECS and ICCS hot band specimens were annealed at 900°C for 180 seconds and water quenched. The EBSD maps were taken at the near surface of the rolling plane and presented in Fig 4.2.6. As may be seen, static recrystallization took place after annealing the hot band, leading to a fully recrystallized grain structure, compare Fig 4.2.4 with Fig 4.2.6, i.e. after finish hot rolling and hot band annealing

respectively. Note the increase in the HAGB fraction in both the IECS and ICCS specimens after annealing in Fig 4.2.6 (c) and (d) respectively.

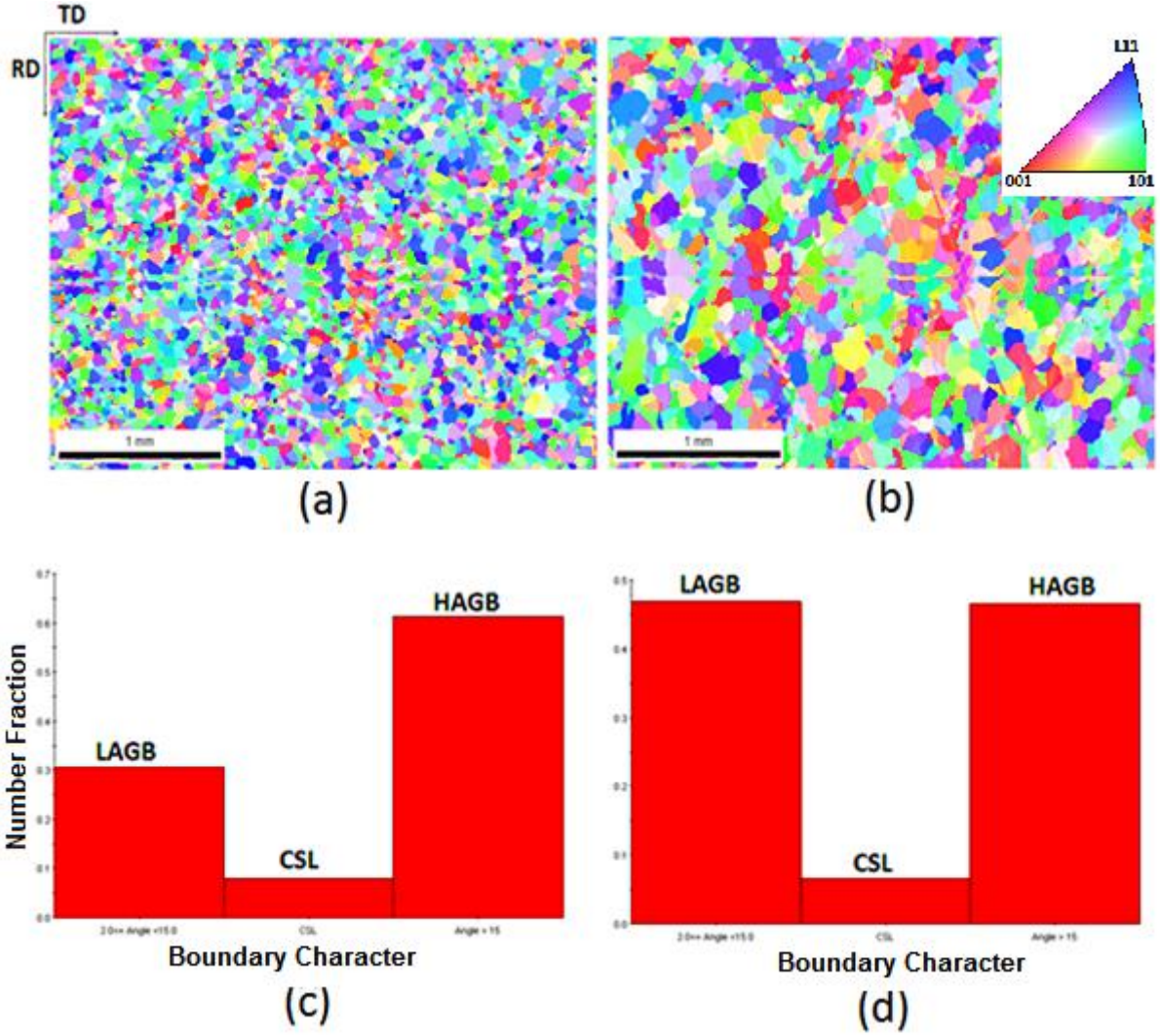

Figure 4.2.6: EBSD maps in the near surface-layer in the RD-TD plane after annealing of hot bands of the respective specimens from (a) IECS and (b) ICCS and corresponding GBCD graphs for (c) IECS and (d) ICCS specimens.

The average grain sizes of IECS and ICCS specimens after hot band annealing were found to be 11±3 µm and 40±9 µm respectively. This observation is in agreement with the coarser ICCS specimen's microstructures prior to annealing.

The near-surface of the IECS specimen recrystallized into a strong (101) and a weak (111) texture, see Fig 4.2.6 (a). These orientations are components of the Goss and γ —fibre textures respectively. Noteworthy in the IECS specimen's microstructure is the uniform distribution of grain size and grain orientations across the matrix, i.e. no grain clustering had occurred. The ICCS specimen also revealed a predominantly (101) texture but with less (111)-texture, Fig 4.2.6 (b), i.e. the Goss texture components were more dominant than that of the γ —fibre. In both steels after annealing, the Cube texture was to some extent replaced by the Goss texture, compare Fig 4.2.4 (a) and (b) with Fig 4.2.6 (a) and (b). Fig 4.2.6 (c) and (d) also reveal that IECS specimen recrystallized more than the ICSS specimen, i.e. with a lower fraction of LAGB in the IECS specimen (0.31) than in the ICCS specimen (0.47).

EBSD maps from the centre layer of both IECS and ICCS specimens are presented in Fig 4.2.7. A fairly equal fraction of (001), (101) and (111) oriented grains in the IECS specimen was observed while a strong nearly (001) texture and a weak nearly (101) texture in the ICSS specimen was observed, Fig 4.2.7 (a) and (b) respectively.

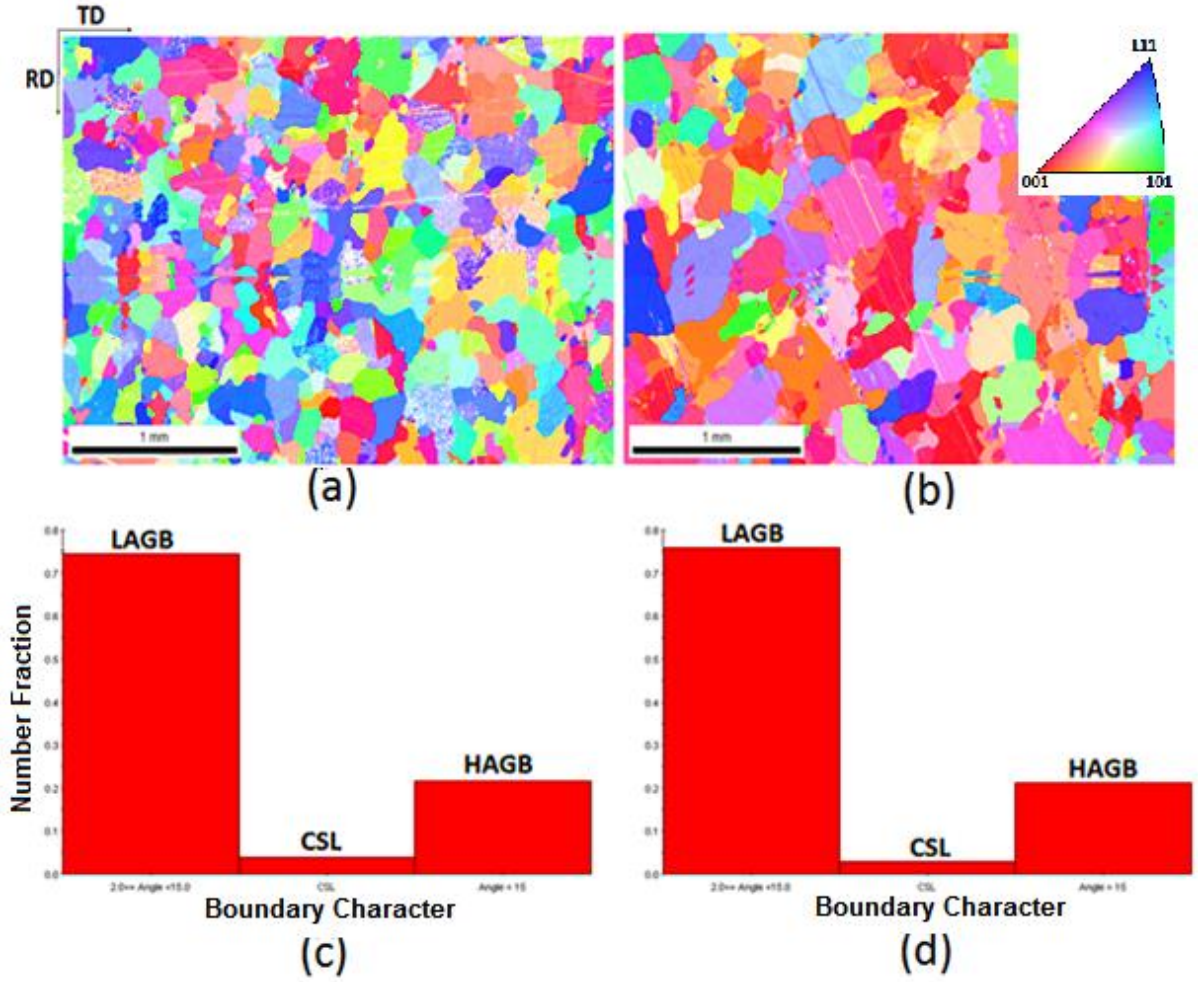

Figure 4.2.7: EBSD maps from near centre-layer in the RD-TD plane after annealing of hot bands of specimens from (a) IECS and (b) ICCS and corresponding GBCD graphs for (c) IECS and (d) ICCS specimens.

The average grain size of the IECS specimen was found to be 32±06 µm, which is less than that of the ICCS specimen (69±13 µm). For both the IECS and ICCS specimens, the grain size was coarser at the center. This is attributed to limited recrystallization at the center, see Fig 4.2.6 (c) and (d) and Fig 4.2.7 (c) and (d) for near surface and center respectively, i.e. there is higher fraction of HAGB in the former. For the IECS specimen at the center, the HAGB fraction was found to be 0.22 while at the near surface it was 0.61. Similarly, for the ICCS specimen at the center, it was found to be 0.21 while in the near-surface it was 0.46. In other words, microstructural and texture gradient existed through the thickness of both IECS and ICCS hot band specimens. However, even within these gradients, the IECS specimen exhibited a higher fraction of (111)-oriented and finer grains while the ICCS specimen exhibited more (001)-oriented and slightly coarser grains.

4.2.4. Analysis of HBA-CR microstructures

The annealed hot hand (HBA) was cold rolled and the elongated grains were characterized by mainly (111)-orientation in IECS specimens. Some regions (light in colour) were not resolved; see Fig 4.2.8 (a). These might be severely deformed regions with high dislocation density. Contrary to the IECS

specimens, the ICCS specimens exhibited more (001)-oriented grains, followed by (111) texture grains, Fig 4.2.8 (b).

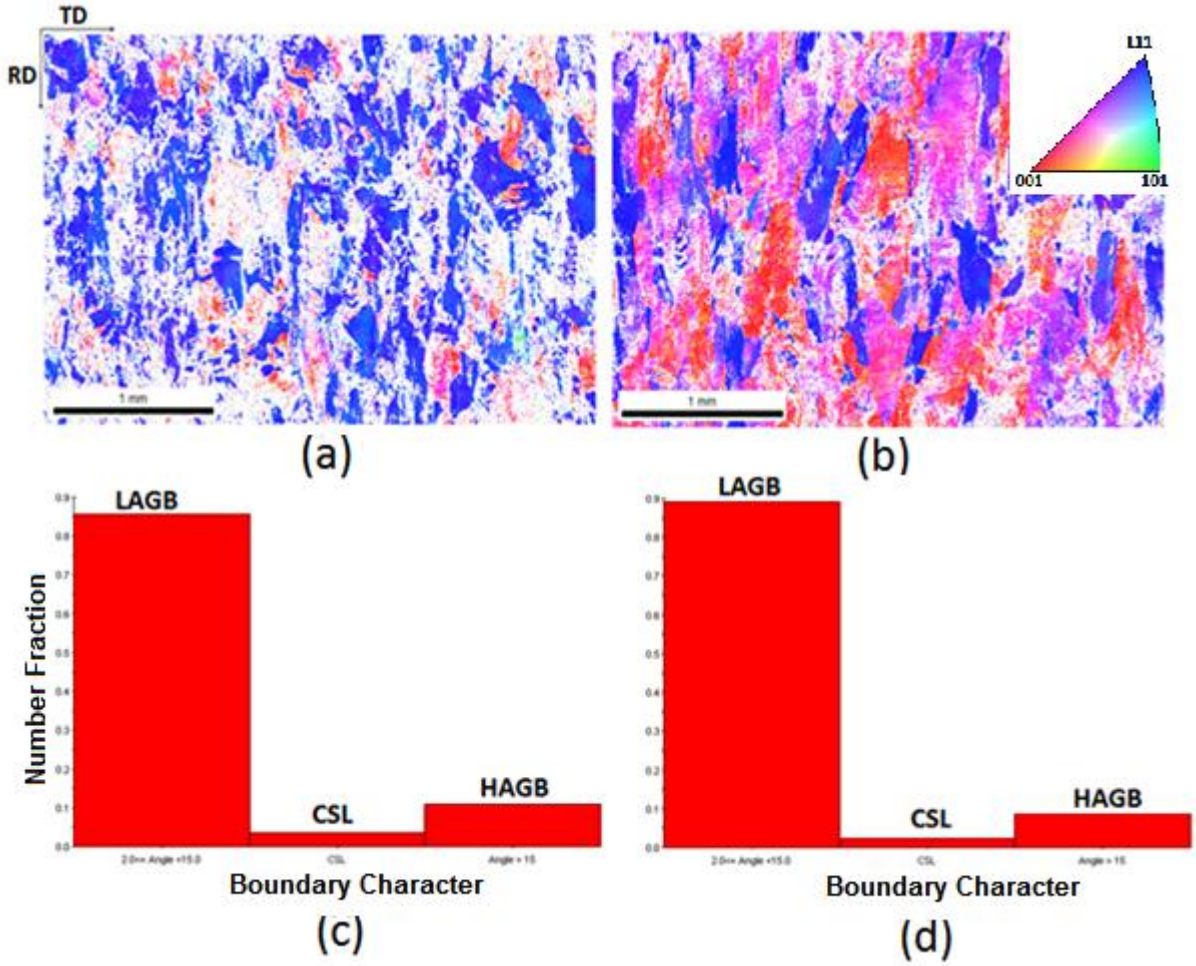

Figure 4.2.8: EBSD maps at near centre in the RD-TD plane after cold rolling of HBA steels in specimens from (a) IECS and (b) ICCS and corresponding GBCD graphs for (c) IECS and (d) ICCS specimens.

4.2.5. Analysis of HB-CR microstructures

After cold rolling the specimen IECS HB, (111) and (001)-oriented grains emerged strongly which were aligned in the RD with a pancake shape. The annealing of the hot band seemed to promote cold worked (111)-oriented grains at the expense of the (001)-oriented grains, compare Fig 4.2.8 (a) with Fig 4.2.9 (a). However, in view of IPFs mentioned in previous Fig 4.2.8 (a) seems to have some non-indexed grains, which made previous statement not convincing. By using their bulk texture ODFs acquired by XRD, given in Appendix A, see Fig 1.8A–HB-CR and Fig 1.9A –HBA-CR, do show high intensity of {111}-grains in HBA-CR than in HB-CR. On the contrary, cold rolling did not change the ICCS HB specimen's much, i.e. it remained largely (001) texture, see Fig 4.2.8 (b) and Fig 4.2.9 (b).

The GBCD graphs revealed a higher fraction of LAGB than CSL and HAGB in both samples after cold rolling. Nevertheless, the fraction of 0.79 LAGB of IECS specimen is greater than that of the ICCS specimen (0.57), see above Fig 4.2.9 (c) and (d) respectively. This might be attributed to the differences in the starting microstructures of the IECS specimen being finer than that of the ICCS specimen.

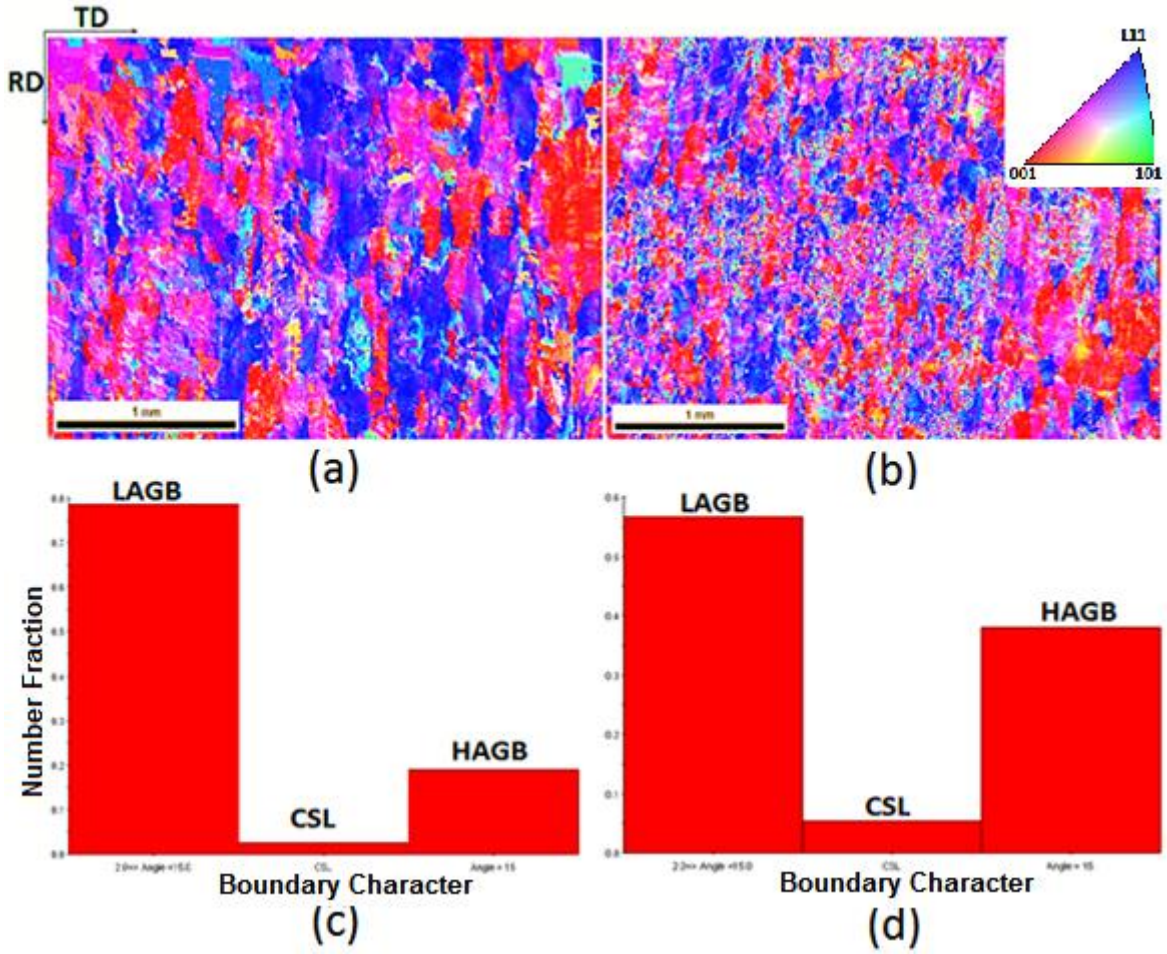

Figure 4.2.9: EBSD maps at near centre in the RD-TD plane after cold rolling of HB from the (a) specimen IECS and (b) from the ICCS specimen and corresponding GBCD graphs for (c) IECS and (d) ICCS specimens.

4.2.6. Analysis of HBA-CRA microstructures

The cold rolled HBA strips were annealed at 900 °C for 180 s and then water quenched as practiced in the plant. EBSD maps were scanned at the near centre thickness and presented in Fig 4.2.10. The EBSD maps of both IECS and ICCS specimen's annealed bands show grains that are partially recrystallized. As may be seen, both annealed bands have a finer grain size. The average grain size from IPF maps of IECS and ICCS specimen's annealed bands were found to be 11±06 µm and 12±04 µm respectively, i.e. there was no substantial difference between the two.

Fig 4.2.10 also presents grain orientations of annealed bands. As may be seen in Fig 4.2.10 (a), that from the IECS specimen's HBA-CRA, was characterized by homogenously distributed (111)-oriented grains while the equivalent ICCS specimen's material to an extent consisted of clusters of (001), (101) and (111)-oriented grains, Fig 4.2.10 (b). In other words, both specimens from IECS and ICCS exhibited homogenous and heterogeneous textures respectively. This has an implication on the Taylor Factor distribution, see section 4.2.8.

Even after 62% cold work and annealing at 900 °C for 180 s, there was still a relatively high fraction of LAGB, i.e. 0.64 and 0.42 for both IECS and ICCS specimens respectively. This suggests that static recovery was followed by static recrystallization and this was expected from a high stacking fault energy ferritic steels.

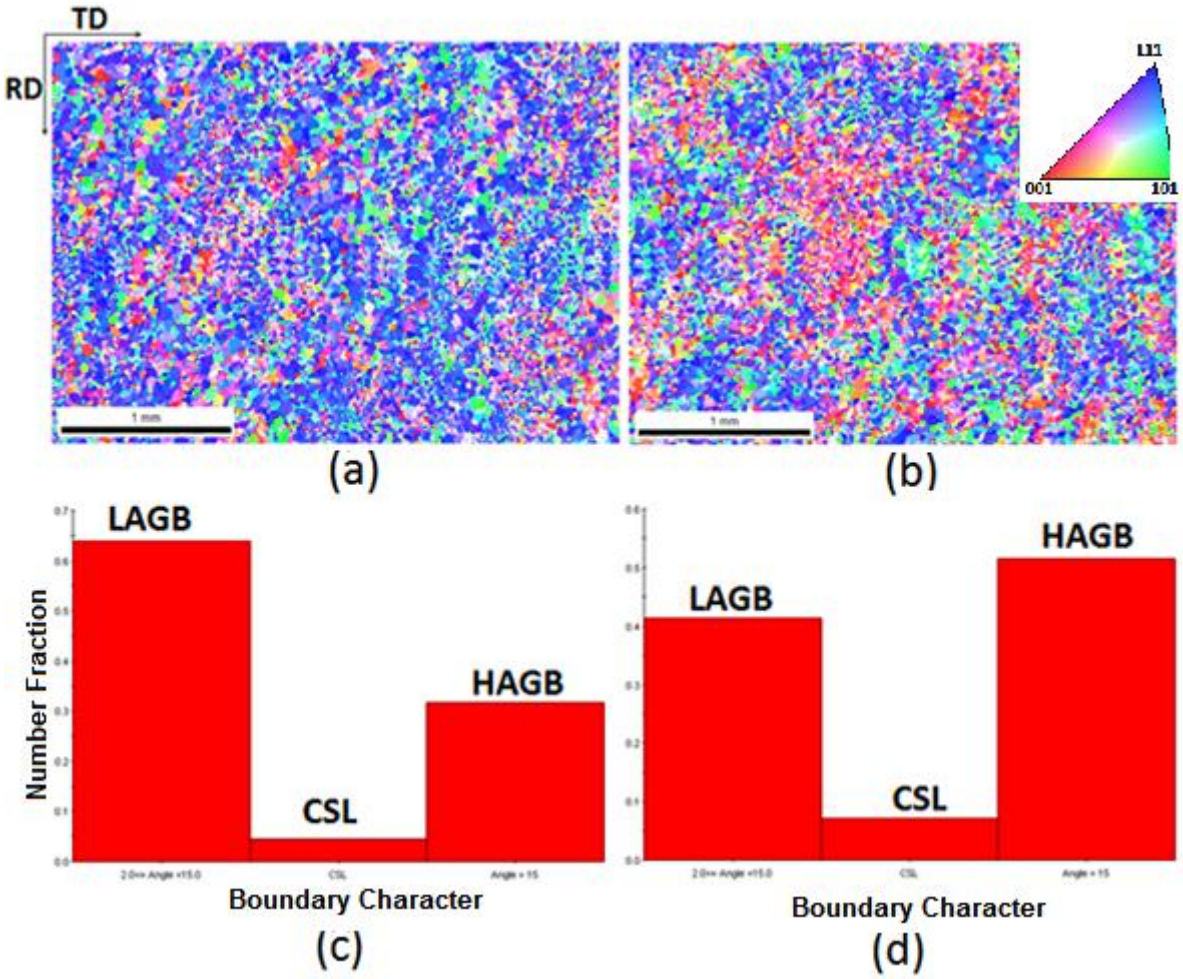

Figure 4.2.10: EBSD maps at near-centre in the RD-TD plane after annealing of HBA-CR steels (a) IECS specimen and (b) ICCS specimen and corresponding GBCD graphs (c) IECS specimen and (d) ICCS specimen.

4.2.7. Analysis of annealed HB-CRA microstructures

The EBSD maps of HB-CRA are given in Fig 4.2.11 and as may be seen, the IECS specimen exhibited a mixture of (111), (001) and (101)-oriented grains. The (111)-oriented grains were still dominant but not as much as in IECS HBA-CRA specimen, Fig 4.2.10. The pink-colour oriented grains are between the (001) and (111)- orientation but close to the (111)-orientation as seen from the orientations color scale given in Fig 4.2.11 (a). The ICCS HB-CRA material was characterized by a mixture of (001), (101) and (111)-oriented grains however the (001)-oriented grains were dominant, Fig 4.2.11 (b). Unlike in the IECS specimen, colonies of (001) and (101)-oriented grains were somewhat more conspicuous in the ICCS specimen.

A comparison of GBDC graphs between Fig 4.2.10 (HBA-CRA) and 4.2.11 (HB-CRA) show static recrystallization took place more strongly in HB-CRA than in HBA-CRA, which suggests that the former had a larger driving force for recrystallization due to retained strain of the un-annealed hot band.

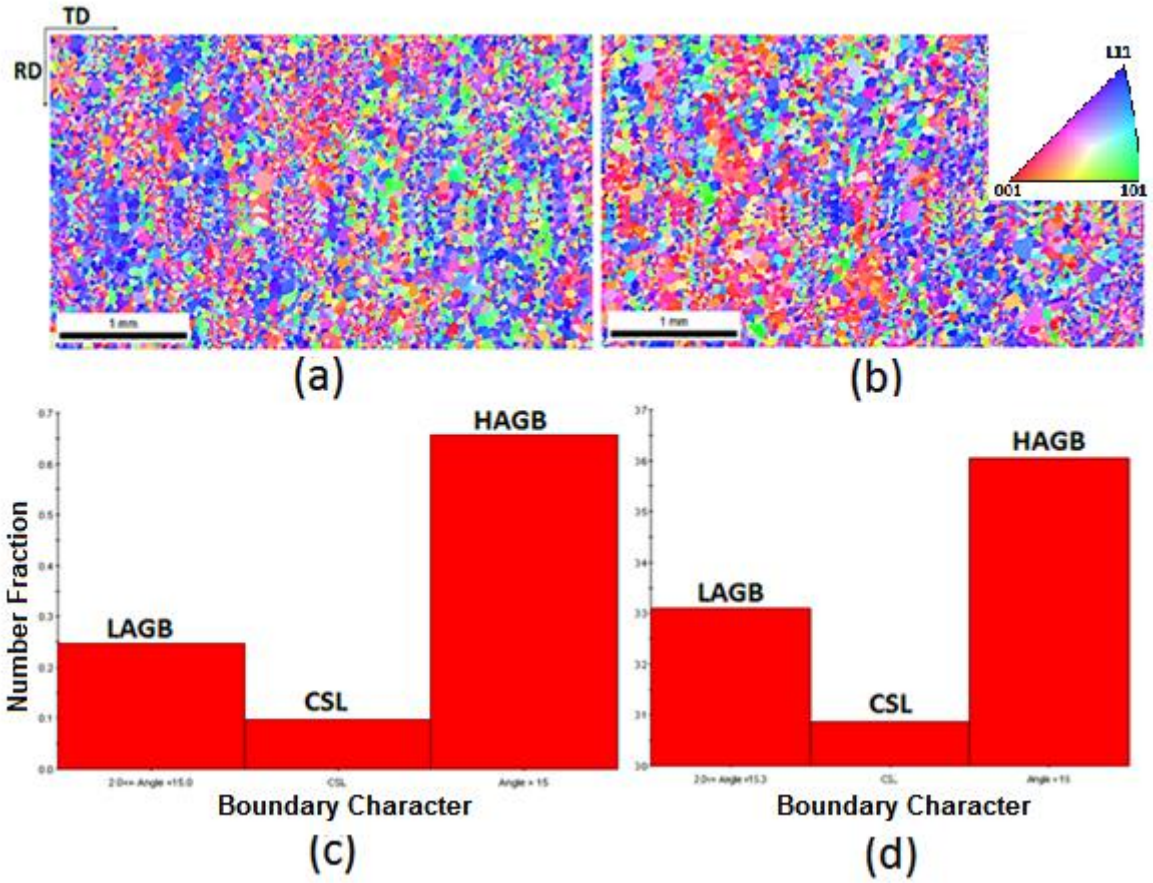

Figure 4.2.11: EBSD maps at near centre in the RD-TD plane after annealing of HB-CR steels (a) IECS specimen and (b) ICCS specimen and corresponding GBCD graphs (c) IECS specimen and (d) ICCS specimen.

4.2.8. EBSD Taylor Factor (TF) Mapping

The Taylor Factor (M_σ) values of HB-CRA strips were mapped and superimposed on the EBSD maps of Fig 4.2.11 as shown in Fig 4.2.12 (a) and (b) for the IECS specimen and the ICCS specimen respectively. As expected, the higher fraction of grains with higher TF values, ranging between 3.35 and 3.80 (orange to red in colour), found in the IECS material with a higher volume fraction of (111)-oriented grains. On the contrary, the high and low TF grains, ranging at values between 2.005 and 2.454 (blue in colour), seemed to form clusters in the ICCS material that is in agreement with the observed clustering of texture in this material, Fig 4.2.12 (b). The industrial implications of these observations will be discussed later.

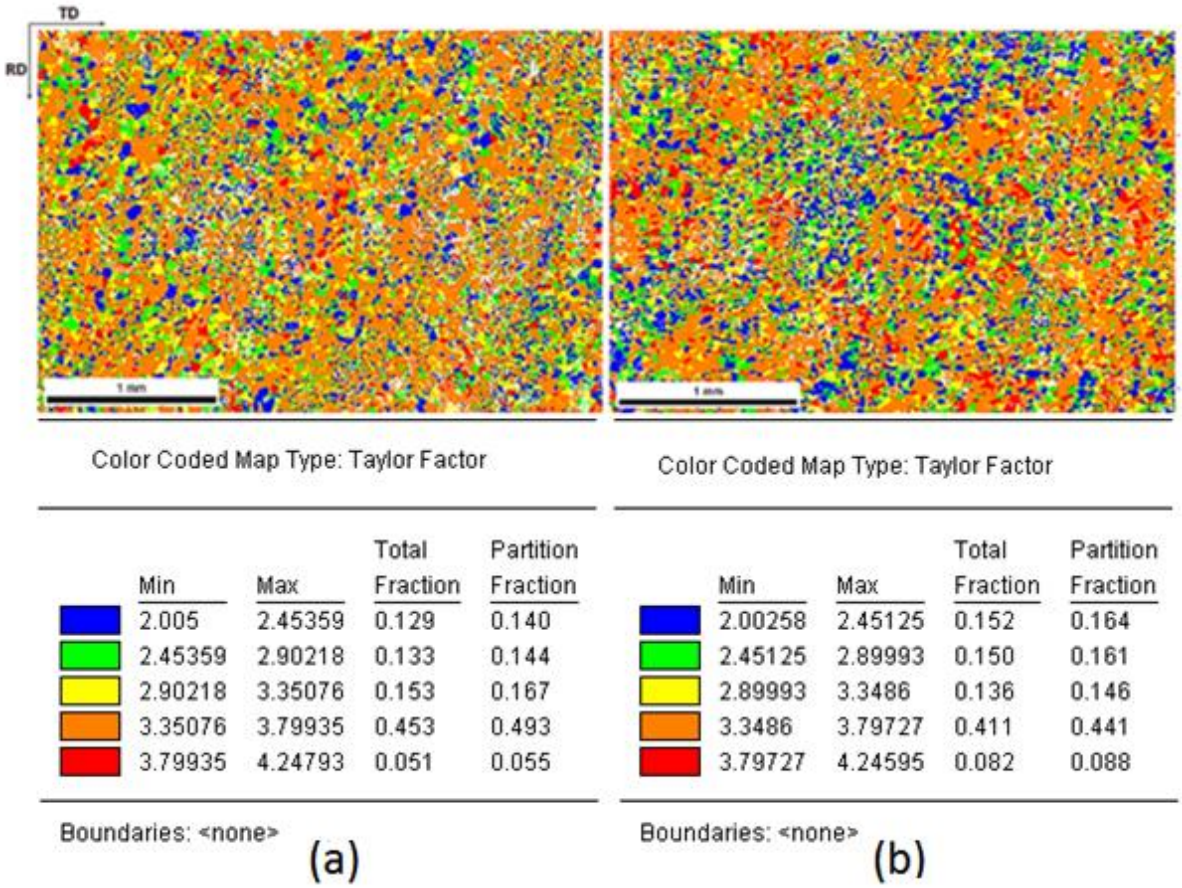

Figure 4.2.12: Taylor Factor maps at near centre layer in the RD-TD plane of HB-CRA steels for (a) the IECS specimen and (b) the ICCS specimen.

4.3. Effects of thermo-mechanical processing on texture evolution in the IECS material versus the ICCS material

4.3.1. Introduction of ODFs texture representation

Almost all bcc steels, i.e. including FSSs, tend to form fiber textures during their rolling and annealing processes. These fiber textures are mainly α −fiber, γ −fiber, Goss, Cube texture, rotated Cube texture and other texture components. A γ −fiber mainly constitutes the orientations with common planes $\{111\}//ND$, α −fiber forms by orientations with common $< 110 >$ directions lying parallel to the RD, Goss is defined by the $(110)[001]$ orientation while rotated Goss is $(110)[1\bar{1}0]$. The Cube texture is $(100)[0\bar{1}0]$ while rotated Cube can be $(001)[1\bar{1}0]$ or $(001)[\bar{1}\bar{1}0]$ orientations. All of these orientations and their positions in Euler space can be seen in an $\varphi_2 = 45°$ ODF given in Fig 4.3.1 below. Crystal orientations are described by Miller indices {hkl}<uvw> e.g. {hkl} defines the crystallographic planes that are parallel to the rolling plane (RD-TD) and <uvw> is the crystal directions which are parallel to the RD or TD.

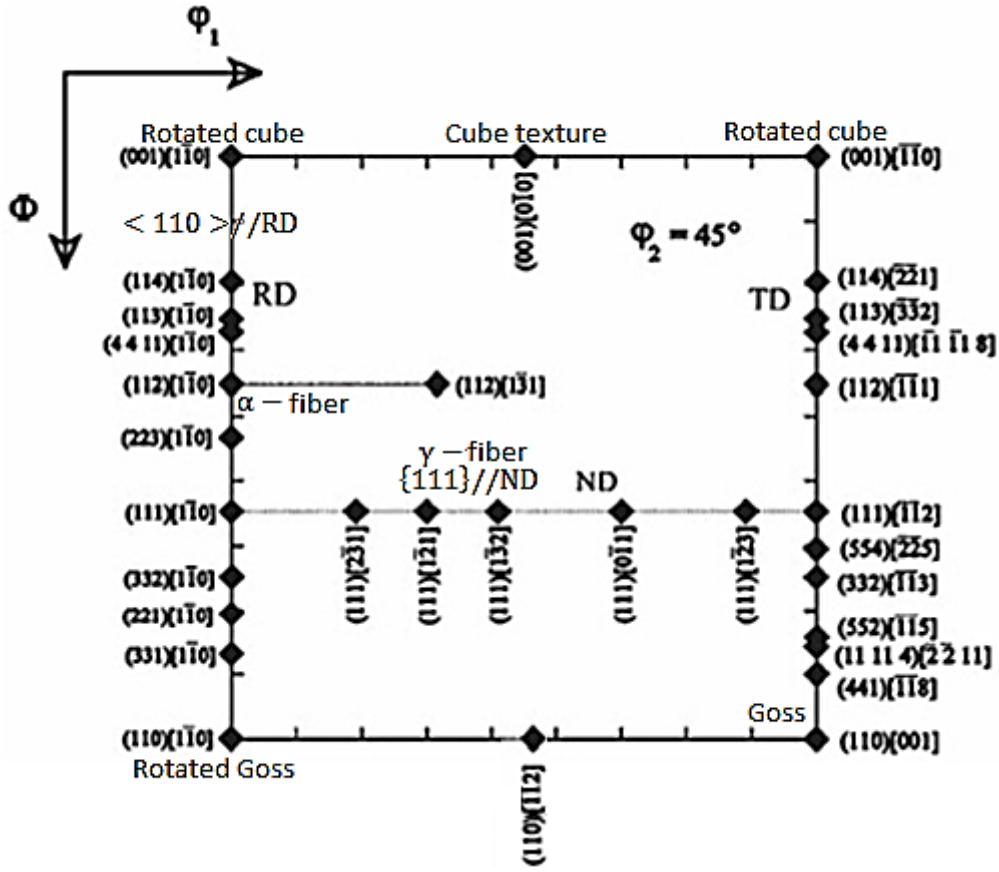

Figure 4.3.1: Ideal texture components located in $\varphi_2 = 45°$ section of bcc steels [66].

4.3.2. Texture analysis of as cast structures

The as cast texture could not be measured with confidence due to the limited scan area vis-à-vis the coarse cast structure of both the IECS and ICCS materials. However, since the recovery process during simulated rough hot rolling was predominantly through DRV, the measured texture distribution was assumed to be close to that of the as-cast condition.

4.3.3. Rough hot rolling texture

Typical ODFs of near-surface layer texture distributions in the IECS and ICCS specimens are shown in Fig 4.3.2 (a) and (b) respectively. The texture distribution across the thickness of the transfer bar after simulated rough hot rolling is presented in Fig 4.3.3 in the form of orientation graphs while the actual ODFs are given in Appendix B. These orientation graphs represent the texture of the near-surface layer (s_1 = 8.38 mm), the mid-surface layer (s_2 = 6.45 mm) and the center layer (s_3 = 4.20 mm) of the transfer bar scanned on the rolling plane (TD-RD). The three layers were scanned in order to assess texture gradients through the thickness of the simulated transfer bar.

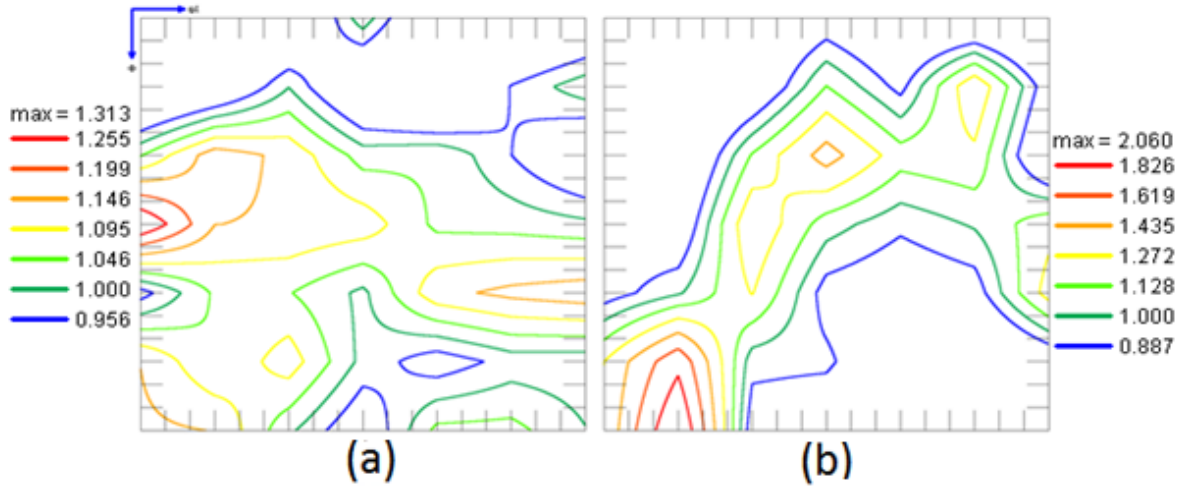

Figure 4.3.2: SEM-EBSD Bunge ODFs $\varphi_2 = 45°$ section in the near–surface layer on the RD-TD plane where s_1 = 8.38 mm (surface layer) after rough hot rolling for (a) IECS and (b) ICCS specimens.

As may be seen in Fig 4.3.2 (a), the IECS specimen's near-surface layer reflects more than two texture components that emerged with nearly equal intensities. The components are the α –fibre texture component, which emerged at the $(223)[1\bar{1}0]$ orientation and γ –fiber of the $(554)[\bar{2}\bar{2}5]$ orientation. The ICCS specimen's near-surface texture shown in Fig 4.3.2 (b) is characterised by a high intensity of rotated Goss texture of nearly $(110)[1\bar{1}0]$ orientation. A slight intensity of Cube texture emerged as well, but located below from its original position and its orientation is $(001)[0\bar{1}0]$. All the prominent texture intensities for the near-surface layer (s_1) for both materials are summarised in Fig 4.3.3 (a) while for the rest, i.e. mid-layer (s_2) and centre layer (s_3) are presented in Fig 4.3.3 (b) and (c) respectively.

In Fig 4.3.3 (b), the mid-layer texture for the IECS specimen is mainly characterised by Cube texture $(001)[0\bar{1}0]$ at a 4.69 intensity and γ –fiber components of $(111)[1\bar{1}2]$ and $(111)[0\bar{1}1]$ orientations with a 2.53 intensity. On the contrary, for ICCS specimens, the dominant texture is rotated Cube texture, i.e. the $(001)[1\bar{1}0]$ and $(001)[\bar{1}\bar{1}0]$ orientations exhibited a strong intensity value of 5.96.

At the centre, the IECS specimen exhibited a mixture of textures namely: rotated Cube texture components $(001)[1\bar{1}0], (001)[\bar{1}\bar{1}0]$ and Cube texture $(001)[0\bar{1}0]$ all with equal intensity values of 1.98. The other texture components were found to be $(114)[\bar{2}\bar{2}1]$ and the α –fiber component of $(114)[1\bar{1}0]$, both with intensity values of about 2.35, see Fig 4.3.3. As opposed to the IECS specimen, the ICCS specimen exhibited only strong rotated Cube texture components, i.e. $(001)[1\bar{1}0]$ and $(001)[\bar{1}\bar{1}0]$ orientations and their corresponding intensity values of 1.86 and 2.17 respectively.

In brief, the general trend is that in ICCS specimens , the dominant texture across the thickness was either Cube or rotated Cube texture while that in IECS specimens was a mixture of texture components

comprised of α and γ-fibre components at the near-surface and mid-layers and with the addition of rotated Cube at the centre layer.

While the texture gradient between the surface and the centre can be attributed to the change in the deformation mode from surface to centre, the initial as-cast microstructure equally influences the texture development during the rough hot rolling process. The mechanisms involved in the evolution of texture in these two starting materials are covered in detail in the upcoming discussion chapter.

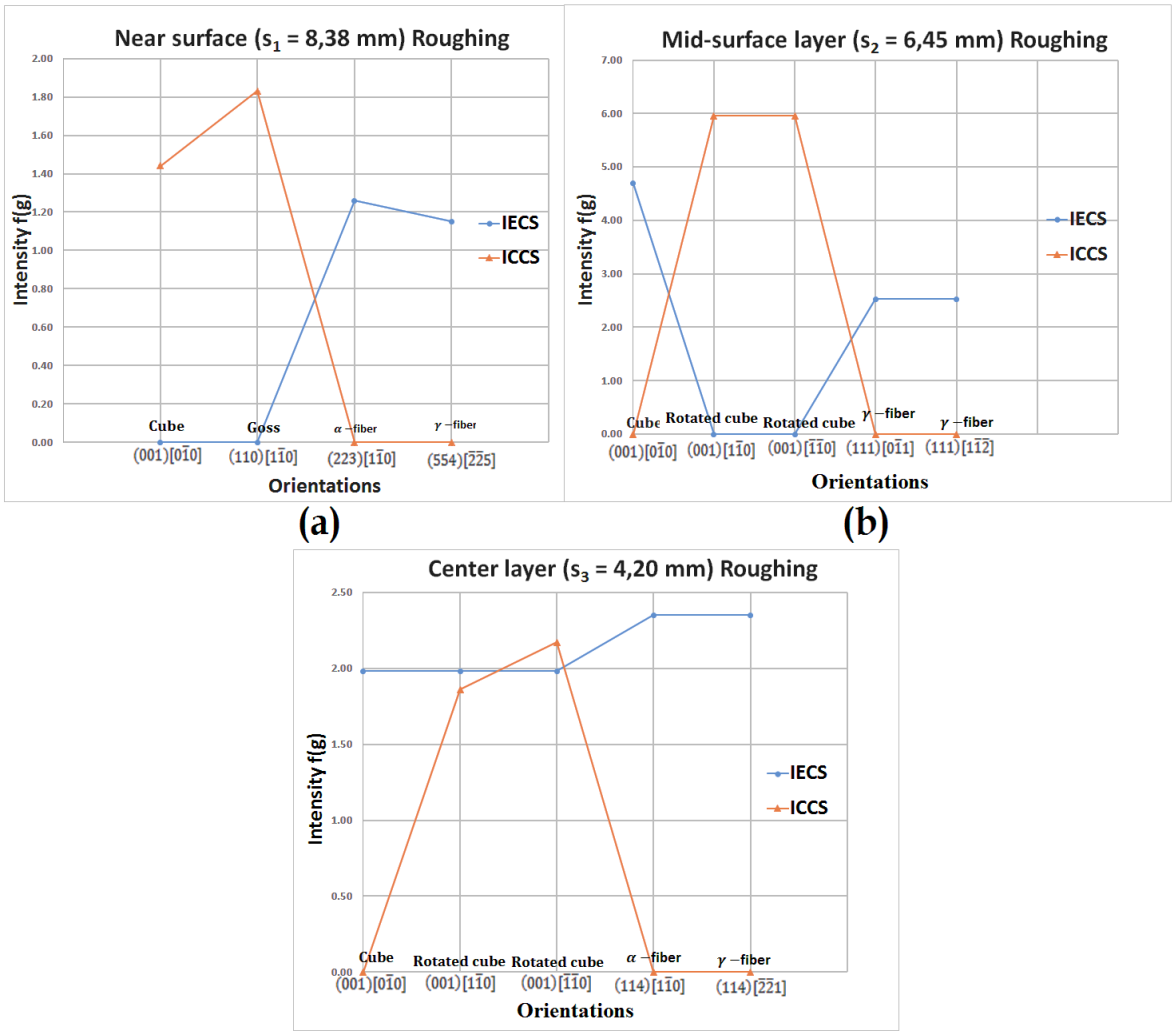

Figure 4.3.3: Crystallographic orientation graphs of the texture through-thickness of transfer bars, (a) near-surface layer (s_1), (b) mid-layer (s_2) and (c) near centre layer (s_3) of IECS versus ICCS specimens.

4.3.4. Textures of finish hot rolling (HB) and annealing of hot band (HBA)

For the thinner hot band (HB) and annealed hot band (HBA) strips, the crystallographic texture was scanned on the near-surface (s_1) and centre (s_3) layers. The results for both IECS and ICCS specimens are given in the form of orientation graphs in Fig 4.3.4.

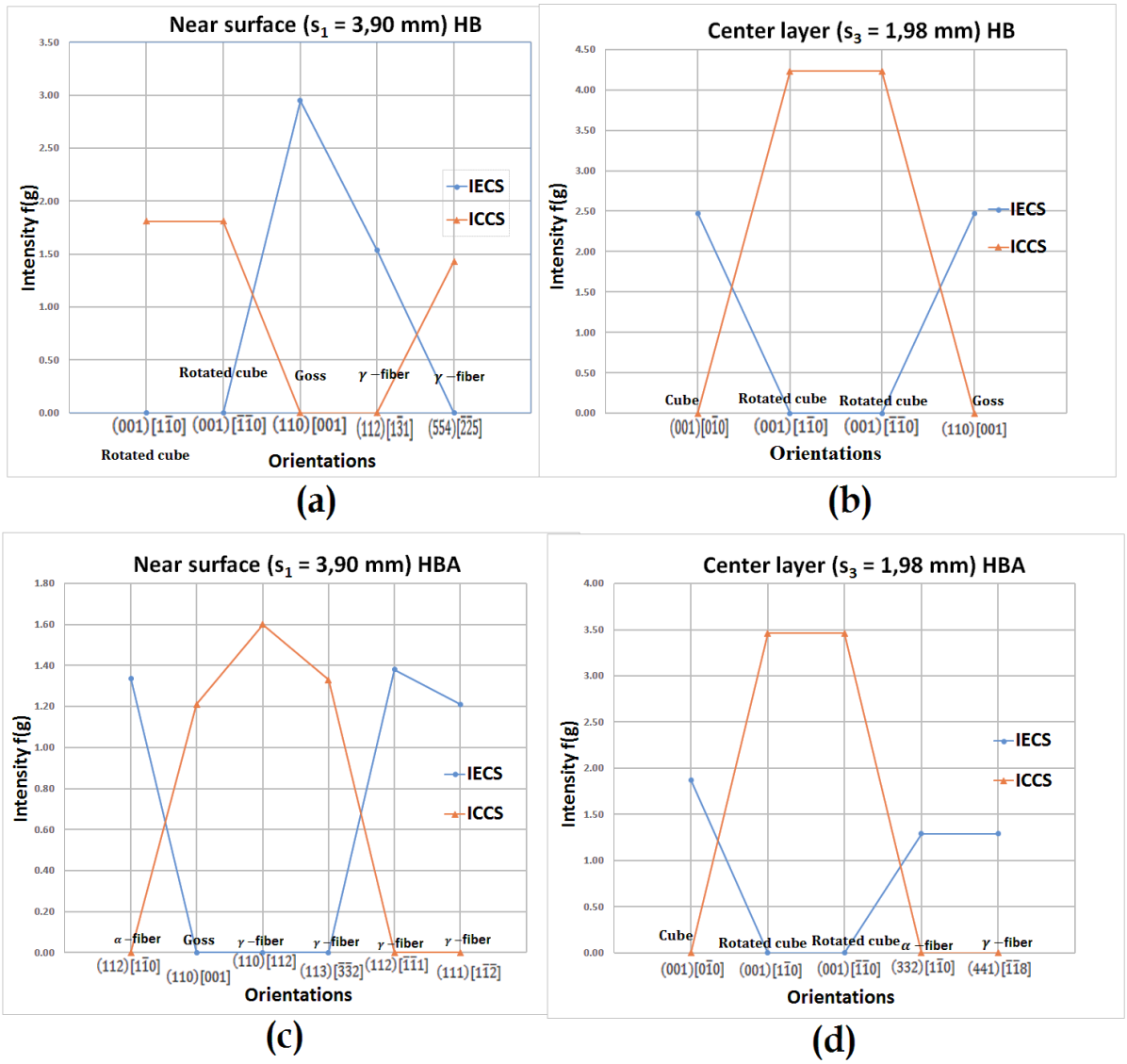

Figure 4.3.4: Crystallographic orientation graphs of texture through-thickness of hot band, (a) HB-s_1, (b) HB-s_3, (c) HBA-s_1 and (d) HBA-s_3 of IECS versus ICCS specimens.

As may be seen at the near-surface in Fig 4.3.4 (a), the texture in the IECS material is characterized by the Goss texture $(110)[001]$ component and the γ –fiber component of $(112)(1\bar{3}1]$ orientation with intensity values of 2.95 and 1.54 respectively. The ICCS material is characterized by the rotated Cube texture $(001)[1\bar{1}0]$ $(001)[\bar{1}\bar{1}0]$ orientations and γ –fiber $(554)[\bar{2}\bar{2}5]$ with intensity values of 1.18, 1.18 and 1.43 respectively. It is evident that the near surface texture of IECS and ICCS hot band materials emerged differently except for the common γ –fiber.

Due to the limitation of hot band thickness, only the center texture not mid-layer texture was examined and presented in Fig 4.3.4 (b) above. Cube $(001)[0\bar{1}0]$ and Goss $(110)[001]$ texture components with equal intensity values of 2.47 emerged at the center layer of IECS hot band material

whereas ICCS material exhibited only rotated Cube texture $(001)[1\bar{1}0]$ and $(001)[\bar{1}\bar{1}0]$ orientations at an equal peak intensity value of 4.23.

A comparison between surface and centre textures in both HB materials confirms that texture gradients exist between surface and centre and that the evolution of texture in general is different in these two starting materials, i.e. the notorious Cube texture is persistent in the ICCS material even after "Steckel Mill" simulated finish hot rolling.

The annealed hot band results are presented in Fig 4.3.4 (c) and (d) above. After annealing the HB, it was noted that the near-surface and center layers recrystallized into different texture components from the HB texture in both materials, Fig 4.3.4 (a) and (b). However, some HB texture components survived the recrystallization annealing process such as the near-surface Goss texture in IECS material, i.e. the $(110)[001]$ texture simply transformed to $(110)[112]$ after recrystallization annealing. In ICCS annealed HB, the near-surface texture was characterized by $(110)[112]$, $(113)[\bar{3}\bar{3}2]$ and $(112)[1\bar{1}0]$ orientations and their intensities were found to be 1.60, 1.33 and 1.21 respectively, which were not observed in the hot band near-surface texture. At the center, the ICCS material's texture components remained unchanged after annealing the HB except for their intensities which decreased slightly, see Fig 4.3.4 (b) and (d). Once again, texture gradients were observed between the surface and centre layers of both materials. These results are discussed in detail in the discussion chapter.

4.3.5. Textures of cold rolled (HB-CR and HBA-CR) and annealed (HB-CRA and HBA-CRA) strips

The HB and HBA materials were cold worked to 1.5 mm from 3.95 mm thickness, i.e. 62 percent cold reduction, and annealed under similar conditions. Since these were thin strips, texture was only measured at the near center and presented in crystallographic orientation graphs given in Fig 4.3.5.

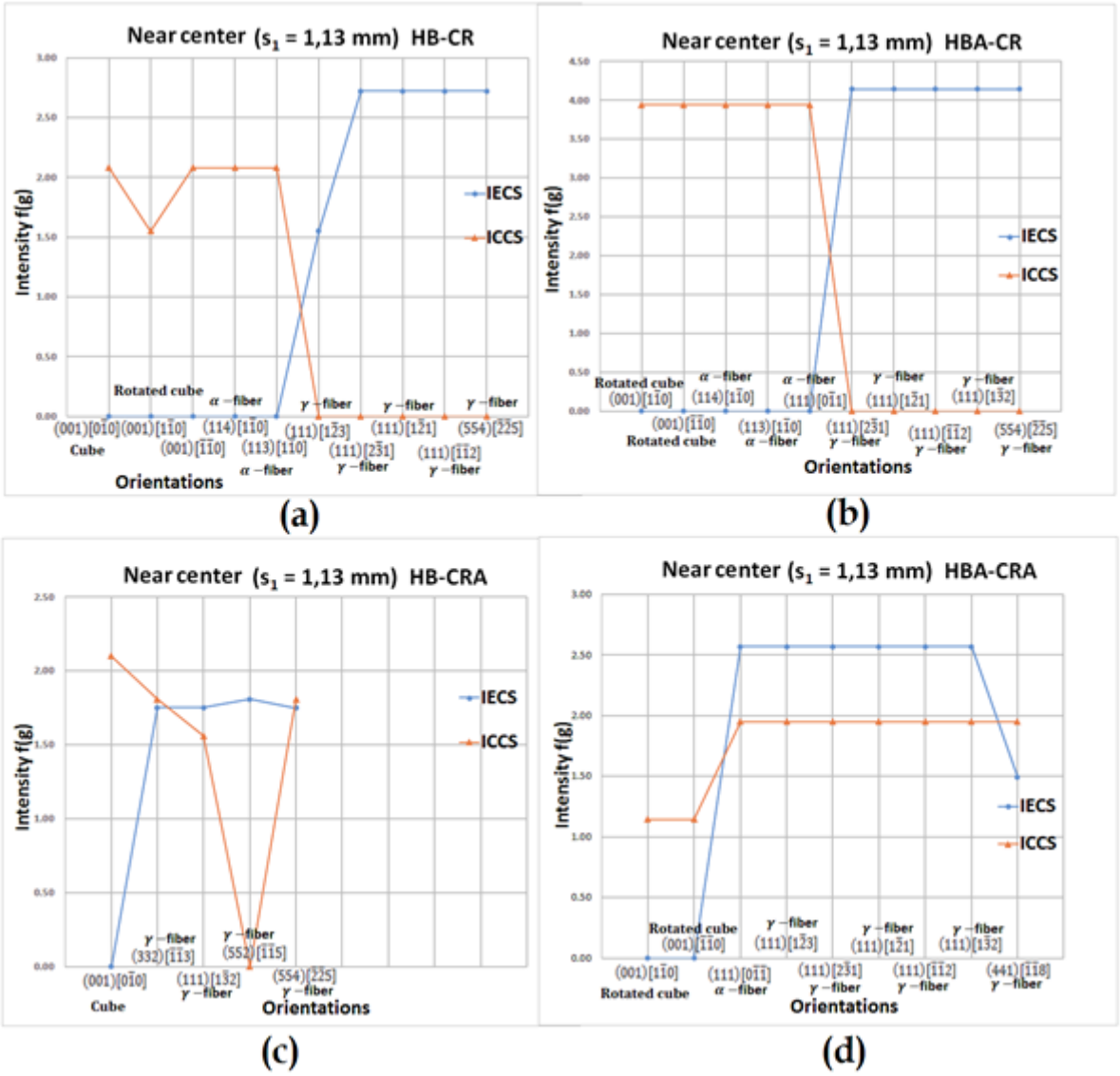

Figure 4.3.5: Crystallographic orientation graphs for the texture of cold rolled and annealed strips at near-centre (s_3), the (a) HB-CR, (b) HBA-CR, (c) HB-CRA and (d) HBA-CRA materials.

After cold working, both the HB-CR and HBA-CR materials were characterized by similar texture components but in different intensities in both IECS and ICCS cold band strips, see Fig 4.3.5 (a) and (b). Fig 4.3.5 (a) shows orientation graphs of HB-CR (cold worked hot band) at the near-centre for IECS whereby four γ −fiber components emerged at equal intensities of 2.72. These results suggest that a strong homogenous texture emerged during cold working of the IECS hot band sample. On the contrary, the ICCS cold band was characterized by various texture components namely: Cube texture $(001)[0\bar{1}0]$ with an intensity value of 2.08, rotated Cube texture components $(001)[1\bar{1}0]$ and $(001)[\bar{1}\bar{1}0]$ with intensity values of 1.55 and 2.08 respectively, α −fiber components $(114)[1\bar{1}0]$ and $(113)[1\bar{1}0]$ both with intensity values of 2.08 and a γ −fiber component $(111)[123]$ with an

intensity value of 2.08, see Fig 4.3.5 (a). It is therefore evident that ICCS material is characterized by texture heterogeneity after cold rolling.

The HBA-CR material's texture was characterized by only γ –fibre components with a maximum of 4.14 intensity around $(111)[2\bar{3}1]$, $(111)[1\bar{2}1]$, $(111)[1\bar{3}2]$, $(111)[\bar{1}\bar{1}2]$ and $(554)[\bar{2}\bar{2}5]$ orientations as shown in Fig 4.3.5 (b) above. This is evidence that the cold working in HBA IECS material promoted a stronger homogenous γ –fibre texture distribution than in the HB of which the γ –fibre texture intensity was only 2.72. However, their texture components emerged at a similar locations, i.e. the annealing of the HB promoted intensity of the γ –fibre texture components.

In contrast to the HBA IECS material, the HBA ICCS material was characterized by mainly α –fiber and rotated Cube texture components with a strong intensity value of 3.94. The α –fiber components that emerged are $(111)[0\bar{1}1]$ $(114)[1\bar{1}0]$ $(113)[1\bar{1}0]$ and the rotated Cube texture components are $(001)[\bar{1}\bar{1}0]$, $(001)[1\bar{1}0]$ orientations. The ICCS HBA material's texture components are almost similar to those of the HB-CR components. The difference lies only in their intensity values whereby the HB-CR material exhibits 2.08 for the α –fiber components and 1.55 for the rotated Cube while the HBA-CR material exhibits 3.94 for both α –fiber and rotated cube texture components.

Annealing of the HB-CR IECS sample promoted the recrystallization of γ –fibre texture components; see Fig 4.3.5 (c) above. The components are $(111)[1\bar{3}2]$, $(554)[\bar{2}\bar{2}5]$ and $(332)[\bar{1}\bar{1}3]$ orientations. The first two orientations were also observed in the HB-CR texture. However, their intensities were at lower values as compared to the HB-CR condition, which decreased from 2.72 to 1.75. As opposed to IECS material, the ICCS material was characterized by both the γ –fibre and Cube texture components at different texture intensity values. The γ –fibre components $(554)[\bar{2}\bar{2}5]$, $(332)[\bar{1}\bar{1}3]$ and $(552)[\bar{1}\bar{1}5]$ were all at an intensity value of 1.81, $(111)[1\bar{3}2]$ at around 1.56 while the Cube texture $(001)[0\bar{1}0]$ emerged with 2.10 intensity. It was therefore evident that the final HB-CRA ICCS material was characterized by the Cube, γ – and α – fibre heterogeneous texture while the final HB-CRA IECS material was characterized by a homogenous γ –fibre texture distribution. A similar trend was also observed in HBA-CRA material, see Fig 4.3.5 (d). However, the γ –fibre texture components were enhanced by the annealing of the hot band before cold rolling, see Fig 4.3.5 (c) and (d).

4.4. Effect of the initial as-cast structures on surface roughening/roping in 433

Optical micrographs of the surface after subjected to a tensile strain of 10 percent are given in Fig 4.4.1. Ridges and valleys parallel to the applied strain axis can be observed in the macrographs, see roping marks indicated by white arrows in Fig 4.4.1. These ridges and valleys are elongated at ranges between 1 to 5 mm along the RD, particularly in the ICCS material. The present observation defines the existence of roping on tensile strained sample surfaces. The degree of roping is found to be higher in ICCS material than in IECS material's surface, see Fig 4.4.1. This proves that the IECS material was more resistant to surface roughening than the ICCS material. The roping was then scanned to quantify the surface roughness parameters and to map out the surface roughness profile along the TD. The surface parameters are tabulated in Table 3. As expected, the ICCS material exhibited higher roughness values, which can be attributed to texture heterogeneity as observed in section 4.3.5.

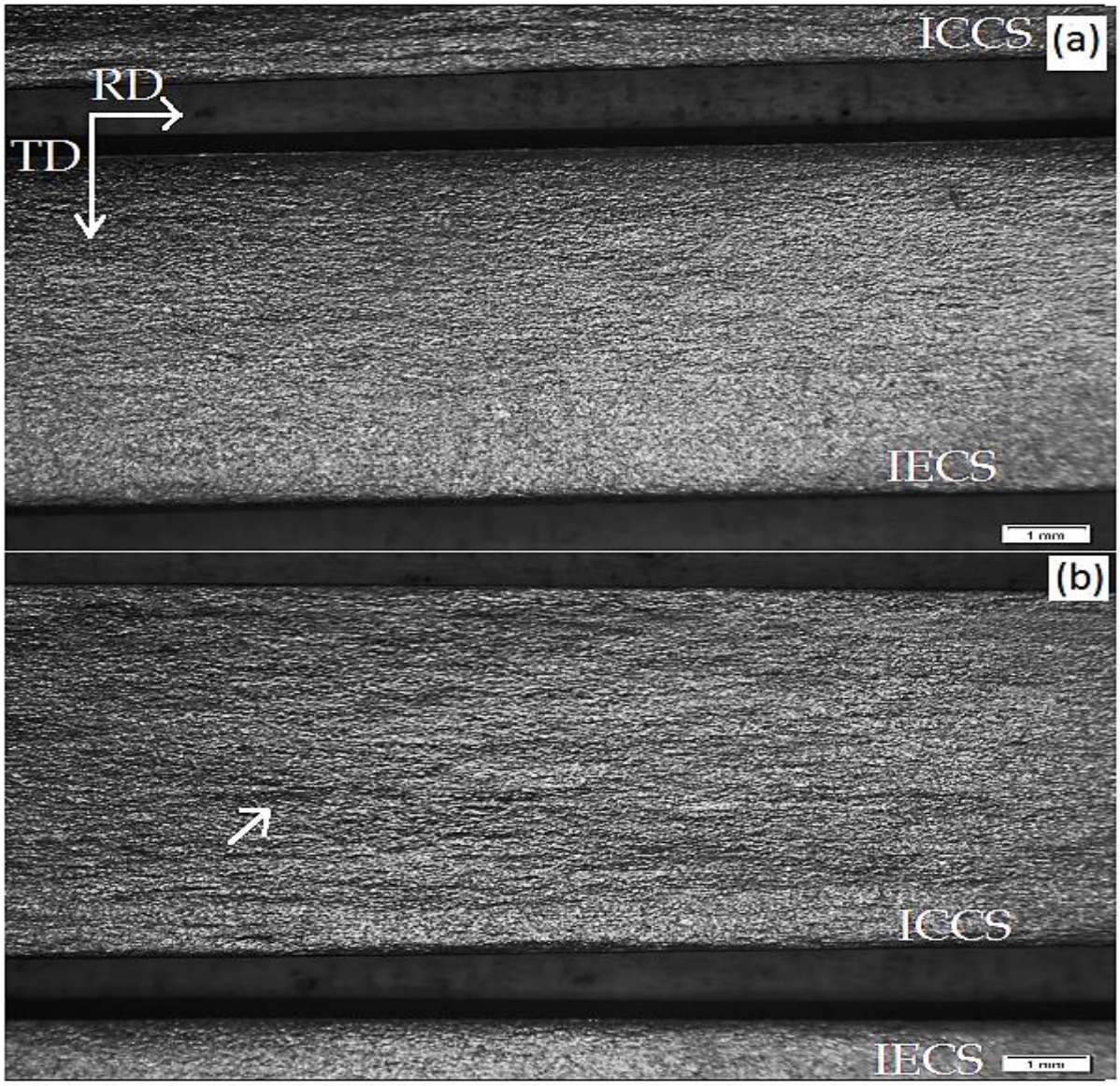

Figure 4.4.1 Optical macrographs of surface topography of HB-CRA samples after 10 percent tensile strain along RD: (a) IECS material, (b) ICCS material; the scale bar is 1mm.

Table 3: Comparative surface roughness of IECS and ICCS materials

Surface Parameters (μm)	**IECS** material	**Benchmark (IECS+ICCS)** material	**ICCS** material	**(%) difference** $\left\lvert\frac{100\% * (\mathbf{ICCS} - \mathbf{IECS})}{\mathbf{ICCS}}\right\rvert$
$\mathbf{R_a}$ Av. deviation	0.52 ± 0.04	0.58 ± 0.037	0.73 ± 0.05	30
$\mathbf{R_z}$ Mean profile height	3.10 ± 0.28	3.86 ± 0.37	3.93 ± 0.89	21
$\mathbf{R_t}$ Max profile height	3.56 ± 0.42	4.04 ± 0.42	4.75 ± 1.37	25
Rsm Mean width of profile elements	232.77 ± 16.64	241.33 ± 12.63	278.68 ± 17.38	16

As may be seen from Table 3, the R_a-value of the IECS material's sample is 0.52 ± 0.04 μm while that of the ICCS material's sample is 0.73 ± 0.05μm, amounting to a 30 % deficit in favour of the IECS material compared to the ICCS material's R_a-value. Similarly, the maximum height of the roughness profile (R_t-value) was measured to be 3.56 ± 0.42 μm in the IECS material vs 4.75 ± 1.37 μm in the ICCS sample, which gives the IECS sample a comparative advantage of 25 %. All of the IECS material's surface parameters were lower than that of their ICCS counterparts. This proves that the IECS material's properties are generally more resistant to surface roughening than that of the ICCS equivalent, except that the R_a-values are lower than 1 μm, which shows that the materials (IECS and ICCS) were less affected by surface roughness when viewed in practical application, see table 3 above.

The surface roughness resistance of IECS material is attributed to the desired homogeneous γ –fibre texture components and the topographic arrangement of grains that manifest in the IECS material after recrystallisation (HB-CRA). The distribution of heterogeneous texture components with a dominant Cube and α, γ –fibre texture, evidenced by the ICCS material after annealing recrystallisation (HB-CRA), detracted the surface roughening resistance of the ICCS material; see Fig 4.4.1 and Table 3 above.

4.5. Effect of cast structures on mechanical properties of 433

Fig 4.5.1 shows the true stress-strain curve of IECS and ICCS materials after subjection to similar treatments of HB-CRA Thermo-Mechanical-Processes (TMP), both strained along the RD. It can be observed that within experimental error, the two starting materials behaved almost in a similar manner, *i.e.* both HB-CRA IECS and ICCS materials exhibited approximately the same yield and ultimate tensile strength along the RD, see table below.

Table 4: Mechanical properties of IECS and ICCS samples at HB-CRA condition

Samples			**IECS**				
Properties			**1**	**2**	**3**	**Average**	**Std. Dev.**
Elongation	e_f	%	36.03	36.88	37.74	38.59	0.86
Reduction area	Z	%	43.63	43.72	43.82	43.92	0.10
Yield strength	S_0	MPa	264.39	265.45	266.52	267.59	1.07
Tensile strength	S_u	MPa	452.21	451.60	450.99	450.38	0.61
			ICCS				
Elongation	e_f	%	36.42	33.58	33.88	34.63	1.56
Reduction area	Z	%	37.68	48.36	43.07	43.04	5.34
Yield strength	S_0	MPa	261.36	251.51	258.54	257.14	5.07
Tensile strength	S_u	MPa	447.28	440.63	439.98	442.63	4.04

Although their recrystallization texture patterns were different and with the only small difference that of the elongation for the IECS material that was slightly higher. The difference in elongation is attributed to differences in texture. The homogeneously distributed recrystallized γ-fibre texture grains in the IECS material contributed to the improved total elongation.

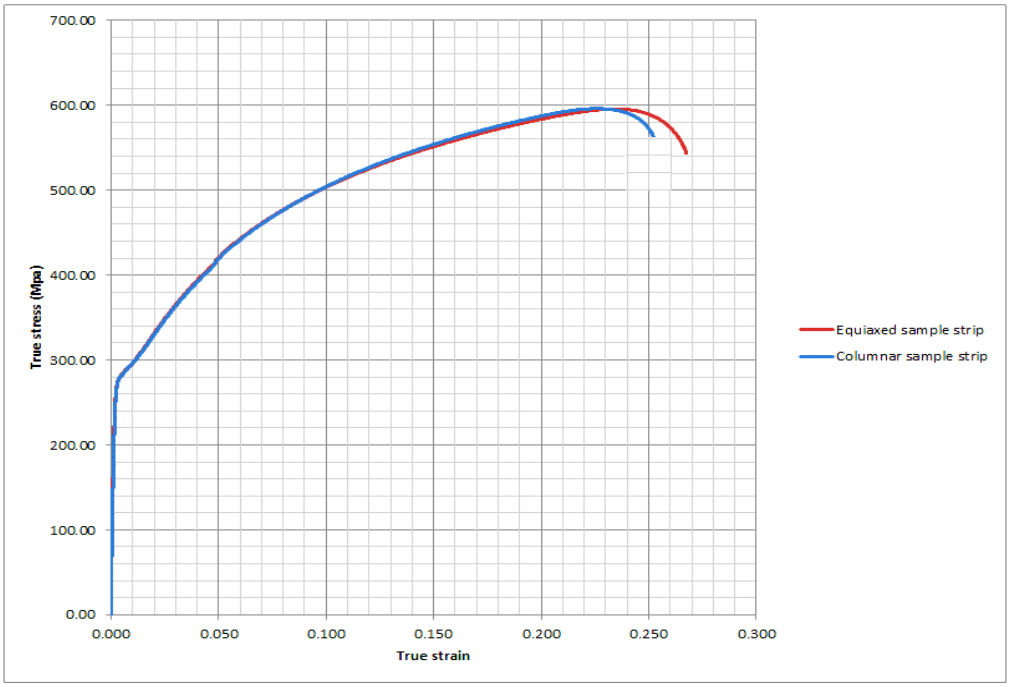

Figure 4.5.1: Typical true stress vs true strain curve of IECS and ICCS materials post-HB-CRA measured along the RD.

Chapter 5: Analysis and Discussion

5.1. Introduction

This chapter is divided into two main sections, to be discussed in detail. The sections are:

- Effects of thermo-mechanical processes on the microstructural and crystallographic texture evolution of 433 stainless steel
- The effect of IECS and ICCS material's respective recrystallization textures (HB-CRA) on roping resistance.

5.2. Effects of Thermo-Mechanical-Processes (TMP) on the microstructural and crystallographic texture evolution of 433 stainless steel

Crystallographic texture studies were carried out after each rolling and annealing stage of the TMP. Texture characterisation in the through-thickness of steel samples was done to understand texture variations through the thickness of the rolled and annealed samples. Blandford [8] observed that surface and centre layers of hot band deform differently during hot rolling. The surface deforms through a shear strain from surface friction between the surface of rolls and work piece while the centre layer deforms by a plane strain compression. These deformation modes induced texture variations from the surface to the centre during hot deformation. In addition, cold rolling is merely a plane strain deformation only, surface friction from the rolls and work piece can be reduced by lubricants and using the smaller pass strains.

The rolling and recrystallisation texture results show that the solidification structures do influence microstructural and texture evolution during TMP. IECS and ICCS material's solidification structures exhibited variations in their microstructure and texture evolution after treatment under the same simulated TMP rolling schedule. For purposes of discussion and analysis of the effect of initial solidification structures on microstructural and texture evolution, each will be discussed per rolling stage to avoid confusion. Discussion and analysis will proceed in the following sequence:

5.2.1. Rough hot rolling band microstructure and texture.
5.2.2. Hot (HB) and annealed hot bands (HBA) microstructure and texture.
5.2.3. Cold rolling bands (for both HB-CR and HBA-CR) microstructure and texture.
5.2.4. Annealing of cold rolled bands (for both HB-CRA and HBA-CRA) microstructure and texture.

5.2.1. Rough hot rolling band microstructure and texture

The effect of the initial solidification structures on the texture evolution was studied on the near-surface (s_1), mid-layer (s_2) and center layers (s_3) of simulated transfer bars. The current study found that s_1, s_2 and s_3 layers were characterized by different microstructural and texture features through the thickness of IECS and ICCS material's transfer bars. Thus, microstructural and textural gradients exist through the thickness of the transfer bars. The microstructures at the s_1 layer of IECS and ICCS materials underwent partial dynamic recrystallization (DRX). The GBCD graphs supported these observations since the fraction of LAGB is greater than that of the HAGB in both transfer bar samples see Fig 4.2.2. This is attributed to the effective high stacking fault energy in ferritic steels which allows them to rapidly recover before recrystallization sets in. However, the IECS material presents a better-recrystallized grain structure than that of the ICCS material, see their IPFs in Fig 4.2.2 (a) of IECS

material and Fig 4.2.2 (b) of ICCS material and their corresponding GBCD graphs given in Fig 4.2.2 (c) and Fig 4.2.2 (d) respectively. Tsuji *et al.* argue that columnar grains exhibit less recrystallization than equiaxed grains during the hot rolling process [81]. In addition, the lesser recrystallization of ICCS material's grain structures might be attributed to (001)<110> oriented grains, which are an inheritance of the initial as-cast texture {001}<uv0> of columnar crystals. These texture components have a low Taylor factor (TF) and in turn store less deformation energy than other orientation components [27]. Since IECS material has an initial random texture while ICCS material has a {001} <uv0> texture, this could be an explanation for the improved recrystallization observed in the IECS material.

The structure of grains at the s_3 layer appeared slightly different from what was observed at the s_1 layer in both materials. The recrystallization was less intense if compared to the s_1 layer. This can be observed from a comparison of the fraction of HAGB between s_3 and s_1, where s_1 has a higher fraction than s_3 and by the microstructure of grains, i.e. s_1 has a mixture of different grain sizes and structures for ICCS material versus uniform grain size and structure for IECS material. During hot rolling, the center layer deforms by plane strain, which promotes DRV and not DRX and retains most of the α –fiber texture components [79]. However, the strain is lower in the center as compared with near the surface that deforms by shear strain during hot rolling; near surface grains tend to experience high DRX while center layer grains received high DRV, which resulted in texture gradient through a hot band thickness during hot rolling.

Engler *et al*. [2] studied the texture gradient through the thickness of hot band in FSS and it was found that the surface and centre of the hot band deform by two different deformation modes, i.e. on the surface with shear strain deformation and in the centre with plane strain deformation. These deformation modes induce differences in microstructure and texture development between the surface and the centre of the hot band. The present results support this observation made by these authors in terms of differences in microstructures and their orientations on near surface and the center of transfer bars. However, recrystallization at the surface was not strong. As expected, this might be due to a lesser amount of deformation energy introduced into material system.

Fig 4.3.3 depicts ODFs texture in graphical format. Surprisingly, unlike ICCS material, no shear/Goss texture, which is caused by shear deformation, was observed in the IECS material's near-surface but primarily α –fibre and γ –fibre texture components. The center exhibited Cube, rotated Cube, α –fibre and γ –fibre texture components. As already mentioned above, the latter is attributed to the plane strain deformation, which promotes Cube and α –fibre texture components during hot deformation [2, 8]. The Cube texture components observed in ICCS material in the near-surface proved that the columnar {001}<uv0> solidification structure still has more influence on hot rolling texture than the shear deformation mode which promotes the Goss texture [2,8, 49]. The center layer of ICCS material was dominated by rotated Cube texture components and this was due to both the as-cast Cube texture and the plane strain deformation mode.

In brief, the results suggested that differences between IECS and ICCS material's s_1 textures exist but both have texture inhomogeneity at s_1 and s_3. Texture and microstructure gradients through both IECS and ICCS material's transfer bars existed differently. This implies that initial solidification structures influence the microstructure and texture differently, i.e. both IECS and ICCS materials developed different texture patterns on the surface and center. However, IECS materials promoted formation of the γ –fibre components in all examined layers while ICCS material promoted the cube and α –fibre texture components.

5.2.2. Hot and annealed hot bands microstructure and texture

Fig 4.2.4 presents the hot rolled microstructures at s_1 with equiaxed structures of grains that were partially recrystallized during hot rolling. This might be attributed to the domination of DRV over DRX which is confirmed by the GBCD graphs, see Fig 4.2.4 (c) and Fig 4.2.4 (d) for IECS and ICCS material's respectively, i.e. the fraction of LAGB is greater than the fraction of HAGB. The DRV is a result of the high stacking fault energy (SFE) [72], which leads to the loss of driving force for DRX. However, the fraction of HAGB in the IECS material is slightly higher than that in the ICCS material, which implies that IECS material partially recrystallized more than the ICCS material. This is observed from the finer and random grain structure distributed across the matrix of the IECS material.

It is evident that recrystallization hardly took place at the center layer of both hot bands; see Fig 4.2.5 (a) and Fig 4.2.5 (b) of IECS and ICCS materials respectively. This can be derived from the poorly formed structure of grains and the fact that grains remained elongated in the RD as seen in the IPFs. With the aid of the GBCD figures, the DRV might have suppressed the DRX during hot rolling or alternatively, the strain was not high enough to induced DRX, see Fig 4.2.5 (c) and Fig 4.2.5 (d). This is in agreement with what other workers have found that a rapid DRV renders FSS material difficult to recrystallize during hot rolling, especially the at the center of hot bands [55].

At s_1, the IECS HB material was predominantly characterised by a strong shear/Goss $(110)[001]$ texture component, followed by the $(112)[1\bar{3}1]$ γ –fibre texture components as graphically presented in Fig 4.3.4 (a) and depicted in Appendix B, Fig 2.4B (a) in ODF format. The ICCS HB material's s_1 texture was made up of rotated Cube and $(554)[\bar{2}\bar{2}5]$ γ –fibre texture components, see Fig 4.3.4 (a) and Appendix B, Fig 2.4B (b). At s_3, the IECS material exhibited Cube and Goss texture while the ICCS material attained predominantly rotated Cube texture. As previously mentioned, the variation in texture between the surface and center of a HB is attributed to the differences in deformation modes and starting as-cast structures [8, 39]. The ICCS material on both s_1 and s_3 levels exhibited predominantly Cube texture while the IECS material formed a Goss texture at s_1 and a mixture of Cube and Goss texture components at s_3. This is in agreement with what Hamada *et al* [73] observed during their studies, it was found that columnar grains with the $\{001\} < \mathrm{uv0} >$ initial texture had a strong rotated Cube texture ($\{001\} < 110 >$) after hot rolling. Grain colonies of $\{001\} < 110 >$ and $\{112\} < 110 >$ orientations were also identified after cold rolling and annealing. In other words, the ICCS material's hot band texture in particular, could be attributed to the inheritance of an initial as cast texture which survived the hot rolling as Cube and α –fibre components as a result of the combined effects of plane strain and DRV during hot rolling [80].

Annealing of hot band is normally done to mitigate texture gradients in the through-thickness of hot band in order to improve its ridging resistance of final cold rolled and annealed strip [79]. In both cases of IECS and ICCS materials, the annealed hot band at s_1 recrystallized into equiaxed grain structures and the texture emerged differently from the hot band without annealing. The grain structure at s_3 was partially recrystallized with a texture almost similar to that of the hot band without annealing (HB) except for a slightly increase in texture intensities.

In HBA IECS material's s_1, the grains were equiaxed, uniform and (111) and (110)-oriented. The former hot band (HB) (111)-oriented grains served as nucleation sites for (111)-oriented grains which grew at the expense of the other oriented grains. It had been reported that (111)-oriented grains exhibit a strong recrystallization rate that makes it possible for them to nucleate earlier and grow by consuming other oriented grains [73]. As may be seen in Fig 4.2.6 (a) and (b), the grain size of ICCS material at s_1 was coarser than that of the equivalent IECS material. The coarser ICCS material's grains are attributed to the initial as cast columnar grains, which exhibit a slower recrystallization rate than the equiaxed grains [81]. At s_3, there was no significant change in texture before and after annealing the hot band

in both cases of ICCS and IECS materials. This is attributed to less preserved deformation energy resulting from plane strain at the center of the material during hot rolling.

5.2.3. Cold rolling bands (HB-CR and HBA-CR) microstructure and texture

The IPFs given in Fig 4.2.9-10 revealed that the hot band grain structures were destroyed during cold working. That can be inferred from the elongated grain structure along the RD and complemented by the cold worked GBCD graphs, where the LAGB fraction was found to be larger than the HAGB fraction in both of the IECS and ICCS materials. The IECS material promoted (111)-oriented grains after cold rolling of both HB and HBA. The (001)-oriented grains apparently emerged with a weak intensity. The strongly emerged (111)-oriented grains could be attributed to the pre-existing hot band (111)orientation since it harbours a large store of deformation energy than any other orientation and influenced the neighbouring grains to gravitate towards the (111)-orientation [43, 44, 55]. It has been observed that the pre-existence of cold worked (111)-grains could enhance the nucleation of recrystallization texture by intensifying the (111)-textures in the final sheet [45]. The recrystallization texture was attributed to the large amount of deformation energy stored in the (111)-grains, which caused them to recrystallize first during annealing and grow at the expense of the other grain orientations, including the α-fibre texture components.

Contrary to the IECS material, the ICCS material's cold band exhibited a mixture of (001) and (111)-oriented grains that emerged strongly in both of the HBA-CR and HB-CR conditions. The (001)-orientation was presumably inherited from the columnar dendrites with an initial (100)<uv0> as-cast texture, and which survived the hot rolling and intermediate annealing as (001)<110> components. Shin *et al* reported that the ND//<001> orientation of the columnar grains, rotates to the $\{001\} < 110 >$ orientation after plane strain compression [75]. The transformation of $\{001\} < 110 >$ to $\{111\} < 112 >$ orientation is difficult because the $\{001\} < 110 >$ component has a low Taylor factor and in turn contains low stored deformation energy, which leads to a slow transformation rate and therefore, preserved the $\{001\} < 110 >$ orientation during the cold rolling stage. This could explain the domination of (001)-oriented grains in the ICCS specimen during the hot and cold rolling stages.

The cold band textures at s_3 are summarized in Fig 4.3.5 (a) and (b), for HB-CR and HBA-CR materials respectively. The annealing of the hot band only increased the intensity of the texture components but did not change their pattern after cold rolling on both of the IECS and ICCS material's cold bands. Ray *et al* note that if the starting cold-rolling texture contains γ −fibre texture components, the components tend to intensify by influencing neighbouring grains to gravitate towards the $\{111\}$ −orientation because of its large storage of deformation energy [76]. That could explain why the HBA-CR texture exhibited a higher intensity of γ −fibre texture components than the HB-CR material. The orientation graphs revealed that the IECS material promoted a homogenous distribution of γ −fibre components in both of the HB-CR and HBA-CR conditions. To the contrary, ICCS material promoted a heterogeneous texture distribution that was made up of rotated Cube and α −fibre components after cold rolling. As expected, these differences influenced the texture after the recrystallization annealing process.

The influence of IECS and ICCS materials on the cold rolling texture was noted. It was observed that IECS material promoted a sharp texture of γ −fibre components while ICCS material supported rotated Cube and α −fibre components after cold rolling and this in agreement with what previous authors found in related steels [73, 79, 80, 81].

5.2.4. Annealing bands (HB-CRA and HBA-CRA) microstructure and texture

In general, the extent of recrystallization of the HBA-CRA material was less than that of the HB-CRA material, see Fig 4.2.10 and 4.2.11 respectively. This can be observed from the GBCD graphs, where the HAGB fraction was more than the LAGB fraction under the HB-CRA material's condition and in the HBA-CRA material's condition, this only holds in the ICCS material. This could be attributed to the reduced stored deformation energy during annealing of the hot band, i.e. compared to hot band without annealing that recrystallized more. The recrystallized IECS material was characterized by homogenously distributed (111)-oriented grains while the ICCS material exhibited clusters of (111) and (001)-oriented grains, especially in the HBA-CRA condition. Recrystallization nucleation prefers HAGBs within a matrix of deformed grains, as the new grains nucleate at HAGB of deformed grains, and will then grow by consuming deformed grains while retaining the orientations of the former grain orientation where from it nucleated [73]. In addition, grains with an orientation that has a high recrystallization rate, such as (111), will nucleate first by adopting that orientation and grow at the expense of other deformed grains with orientations different from (111). However, (100)-orientations are difficult to recrystallize because of their low stored deformation energy, and then prevail during recrystallization and survive scavenging of (111)-oriented grains while other oriented grains are consumed [8]. This could be an explanation for the formation of (111) and (100)–oriented grains after recrystallization in the HBA-CRA condition. The HBA-CR material contained mostly (111) and (100)-oriented grains and these prior textures influenced the subsequent recrystallization orientations with a shift towards more (111)-oriented grains at the expense of the (100)-oriented grains. In contrast, the HB-CRA (both IECS and ICCS materials) recrystallized more than the HBA-CRA material. This is deduced from the well-defined grain structures and recrystallization trends of GBCD graphs, see Fig 4.2.11.

As may be seen in Fig 4.3.5 (d), that the recrystallized texture of both IECS HBA-CRA and ICCS HBA-CRA materials retained most of the cold band texture components; see in Fig 4.3.5 (b). After annealing, the homogenous γ –fibre texture components were enhanced. It is well known that the recrystallization of γ –fibre texture components improves formability and the surface roughness resistance of FSS strips. However if other texture components co-existed equally with the γ –fibre texture components intensities after recrystallization, it affects forming properties negatively [2, 4]. This is what happened in the ICCS material after annealing, i.e. two main texture components emerged, namely the Cube and γ – fiber texture components resulting in texture heterogeneity. The observed Cube texture in ICCS material after annealing is attributed to (100)-oriented grains that were observed in the cold band and were hard to recrystallize. In other words, the Cube texture components were inherited from the initial as-cast (100)[uv0]-oriented columnar grains [73]. This has a negative effect on forming properties of FSS [7, 8, 39]. During tensile straining or deep drawing of strip along the RD, the (111)-oriented grain colonies tend to stretch less than the matrix if the matrix is made up of different grain's orientation and the opposite is the case in which the (100)-oriented grain colonies embedded on the (111)-oriented ferrite grain matrix [3, 30, 39]. This phenomenon will manifest itself as surface roughness.

Knutsen and Wittridge identified a localised anisotropic plastic deformation behaviour at a scale greater than the average grain size on the ND, which was induced by differential orientation clusters or texture heterogeneity [9]. Apart from the differences in texture, the other striking difference was the clustering of small grains notably in ICCS in both HBA-CRA and HB-CRA conditions; see Fig 4.2.10 (b) and Fig 4.2.11 (b) respectively. This may also lead to heterogeneities in response to plastic deformation, which may lead to surface roughening.

5.3. Relationship between formability and the IECS and ICCS materials in the HB-CRA condition

It was found that both IECS and ICCS material's sheets exhibited approximately similar values of yield strength (YS) and ultimate tensile strength (UTS) (see Fig 4.5.1), but their elongation differed by 10 % (IECS material 39 %, ICCS material 35 %), when strained along the RD. The 10 % difference, which is not significant, might be attributed to the differences in the recrystallization texture patterns and the slight difference in grain size. Unlike the elongation, both the yield and ultimate tensile strength were found to be the same, i.e. these were not affected by texture. Strength is an anisotropic property, i.e. the same as elongation; therefore, texture should have an effect on it. Nafisi *et al.* and Yang *et al*. argue that the (001)<110> rotated cube components are responsible for the anisotropy in the strength of steel, strongly in the 45° and 90° than in the direction 0° of the RD [82, 83]. It was found that rotated Cube components provide planes that facilitate crack nucleation and propagation. Therefore, these could explain the observed strengths that appeared equal in both materials. Observation is that the tensile tests were only done at 0° angle of RD.

Unfortunately, the strengths at 45° and 90° of RD were not measured due to material limitation; hence, the effect of the IECS and ICCS material's textures in strength is still unclear. However, Hamada *et al.* [68] note that annealed FSS sheets with a prominently γ –fibre texture exhibit higher R-values, and that texture inhomogeneity with orientations other than $\{111\}$ –texture lower the R-values. The ductility of IECS material in this study is consistent with the findings of Hamada *et al.* [68] since the co-existence of Cube texture with γ –fibre texture components in ICCS material seems to negatively affect the elongation.

5.4. Comparison of surface roughening between IECS and ICCS materials in the HB-CRA condition.

After studying the comparative evolution of texture in IECS and ICCS materials during hot rolling, cold rolling and annealing, the materials in the HB-CRA condition were analysed for resistance to surface roughening and the results are given in Fig 4.4.1. The IECS material was found to be better in terms of resistance to surface roughening. The fact that a homogeneous γ −fibre texture promotes surface roughening resistance has been established. However, this study reveals that when a Cube texture evolves at equal intensity together with the γ −fibre texture, it reduces the intensity of the γ −fibre texture, and therefore adversely affects surface roughening resistance. Lee *et al.* [71] established that a difference in the deformation behaviour of $(001)[110]$ and $(111)[110]$ grain colonies, which are α −fibre texture components, can be ascribed to differences in their plastic strain ratio during cold forming operations, thereby causing surface roughness.

Although the roughness was at the sub-micron level, i.e. not significant at practical applications, especially R_a-value, (see Table 3 in the results chapter), it has been reported by plant trails that 433 performs better than the 430 on practical level in terms of resistance to surface roughness. However, the surface roughness of the ICCS material was still higher than that of the IECS material in the HB-CRA condition. In other words, the R_a-value of the IECS material was found to be 30% less than that of the ICCS material. This is attributed to differences in texture patterns and their distribution, i.e. homogeneous γ −fibre texture components in the IECS material and inhomogeneous γ −fibre and Cube texture components in the ICCS material. The clustering of grain colonies of similar orientations, in this case Cube and γ −fibre texture components during rolling and annealing processes in the ICCS material, led to a reduction in roughening resistance during stretching. As already mentioned above, these $\{001\}$ −oriented colonies of grains undergo more deformation than the matrix along the ND, which therefore leads to trough formation on the sheet surface, while colonies of $\{111\}$ −oriented grains deform less than the matrix along the ND, which therefore favours surface ridges, thus leading to surface roughness formation [39, 65].

When a mixture of IECS and ICCS material structures (benchmark sample from the plant production) were rolled together as starting material, they resulted in a R_a-value higher than that of the IECS material but lower than that of the ICCS material. This proves that a strip with further lower R_a-values can be obtained by using a cast with a domination of equiaxed structure. However, when the volume fraction of equiaxed grains is less than that of columnar grains in a cast structure as an initial rolling material, the surface roughness as measured by the R_a-value will be worse than that of wholly IECS material after hot rolling, cold rolling and annealing processes. Note that this observation it excludes other property parameters, such as tensile properties at 45º and 90º.

Chapter 6: Conclusions

To sum up this study, significant observations emanating from the investigation of the effects of the initial grain structure in as-cast 443 FSS material, can be summarised as follows:

- IECS and ICCS materials affect the crystallographic texture evolution differently during thermo-mechanical, cold rolling and annealing processes. The IECS material promotes development of a homogeneous γ –fibre texture while ICCS material encourages an inhomogeneous texture distribution in which Cube and γ –fibre texture components are predominant after rolling and annealing processes. In other words, unlike IECS material, the as cast Cube texture was more persistent in ICCS material during all stages of rolling and annealing and eventually adversely affected the resistance to surface roughening during stretching.

- Despite the differences in the starting cast structure, the surface roughness as measured by the R_a-value remained in the sub-micron level, i.e. it was found to be insignificant in practical terms. This may be attributed to the Al addition (subject to further investigation) in both IECS and ICCS samples since it has a positive influence on texture development and subsequent forming properties.

- It has been confirmed that IECS material enhanced the formation of γ-fibre texture and leads to less roughening while ICCS material alone results in inhomogeneous texture components and more roughening in this FSS 433. In other words, it was found that it is not the mixture of as-cast structure but the presence of {001}<uv0> as-cast columnar grains that cause inhomogeneity in the final product due to their resilience during processing.

Chapter 7: Recommendations

The following items could be considered for further investigation in 433 FSS:

- Optimisation of the Al addition to promote equiaxed nucleation attributable to the high melting point of the Al_2O_3 fine inclusions that act as nucleants.
- The influence of inclusions on texture through particle stimulated nucleation (PSN) of new grains during the annealing process after cold working.
- The role of AlN in the evolution of texture during hot rolling and annealing after cold working.

References

1. NAKAMACHI, E., AND XIE, C.L. 2002. Investigations of formability of BCC steel sheets by using crystalline plasticity finite element analysis. *Material and Design 23 (2002) 59-68*.
2. ENGLER, O., AND HUH, M.Y. 2001. Effect of intermediate annealing on texture, formability and ridging of 17% Cr ferritic stainless steel sheet. *Material Science and Engineering A308 (2001) 74-87.*
3. LIOYD, D.J., HUANG, Y., AND WU, P.D. 2006. Correlation of ridging and texture in ferritic stainless steel sheet*. Material Science and Engineering, A 427(2006) 241-245.*
4. LIU, H., LIU, Z., AND WANG, G. 2009.Texture development and formability of strip Cast 17% Cr Ferritic stainless Steel. *ISIJ International, Vol,48(2009), No.6, pp 890-896*.
5. WARREN, J.P., ANDWEINBERG, F. 1998. Observation of columnar to equiaxed transition in stainless steels*. Metallurgical and Materials transactions A, volume 29A, pp 855-861.*
6. RAABE, D. 1991.Overview of basic types of hot rolling texture of steels*. Material technology, Max-Planck-Institut fur Eisenforschung, Dusseldorf, Germany.*
7. LIOYD, D.J., JIN, H., AND WU, P.D. 2006.Analysis of ridging in ferritic stainless steel sheet. *Material Science and Engineering A 423 (2006) 300-305*.
8. BLANDFORD, P. 1989. Through thickness inhomogeneity of steel-sheet texture and its effect on material properties*. A thesis submitted to the Faculty of Graduate Studies and Research in Partial Fulfilment of the requirements for the degree of Masters of Engineering, Department of Mining and Metallurgical Engineering, McGill University, Montreal Canada, November 1989.*
9. KNUTSEN, R.D., AND WITTRIDGE, N.J. 2002. Modelling surface ridging in ferritic stainless steel. *Material Science Technology, Volume 18, No 11, pp 1279-1285.*
10. Nickel, 2012, The magazine devoted to nickel and its applications. *Special edition May 2012, pp 5-20*.
11. Introduction to stainless steels. *Alloy digests sourcebook: stainless steel (#06940G), pp 1-7*.
12. Columbus stainless, website http://www.columbus.co.za
13. LEFFLER, B. Stainless-stainless steel and their properties, *pp 4-45*.
14. International Stainless Steel Forum (ISSF) document, 2007, "*The ferritic solution/ The essential guide of ferritic stainless steel*".
15. Stainless steel history and its applications.
16. HUDD, R.C., AND LIEWELLYN, D.T.1998. Steel metallurgy and applications, 3 rd Edition. *pp 169-240*.
17. STUMPF, W.E. 2011. Chapter 2: Dislocations and Deformations. *Mechanical metallurgy NMM 700 course notes, University of Pretoria, page 2.8-4.*
18. BRITISH STAINLESS STEEL ASSOCIATION. 200. Classification of stainless steel types. *SSAS information sheet, no 1.2, issue 01, 01 May 2000, pp 1-2.*
19. CUNART, P.J. 2004. Alloying elements in stainless steel and other chromium containing alloys. *Euro Inox 2004. www. Euroinox.org.*
20. MAALEKIAN, M.2007. The effects of alloying elements on the steel at early stages of precipitation (I).*Christian Doppler Laboratory, October 2007, pp 4-8.*
21. CUNHA, M.A., GONCAVES,. AND OLIVEIRA, T.R. Improving the ridging in AISI 430 ferritic stainless steel stabilized with niobium*, Arcelo-MittalInox Brasil S.A (ex. Acesita S.A), Brazil*.
22. http://www.northamericanstainless.com/quality/NAS Flat Products Process
23. Sassda, December 2013. Fundamentals of stainless steel, Manufacturing of stainless steels module 5. Version 1 pp1-31.
24. LIEWELLYN, D.T. 1994.Steels: Metallurgy and applications 1994. *Butterworth-Heinemann Ltd. 14-22.*
25. VERHOEVEN, JOHN.D. *Fundamentals of Physical Metallurgy*. New York, 1975. pp 282-293.

26. SPITTLE, J.A. 2006. Columnar to equiaxed grain transition in as solidified alloy. *Institute of materials, minerals and mining and asm international. International reviews, vol 51, no 4, pp 247-272.*
27. HU, X., LIU, S., LUO, X., AND SHAN, Y. 2011. Mechanism of Solidification Structure improvement of Ultra-Pure 17 wt%Cr Ferritic Stainless Steel by Ti, Nb addition. *Journal Material Science and Technology, 2011, 27(4), pp 352-358*
28. FAN, L., LI, J., JIANG, L., XIAO, X., XU, Y., AND ZHANG, X. 2015. Effect of Aluminium on microstructure, mechanical properties and pitting corrosion resistance of ultra-pure 429 ferritic stainless steels. *Material and Design 65 (2015), pp 682-389.*
29. LOUHENKILPI, S. 2014. Chapter 1.8. Continuous casting of steel. *Department of Material Science and Engineering, Aalt University School of Chemical Technology, Espoo, Finland. Treatise on Process Metallurgy, Volume 3, 201 Elsevier, pp 373-434*.
30. LIU, H.T., LIU, Z.Y., QIU, Y.Q., CAO, G.M., LI, C.G. AND WANG, G.D. 2009. Characterization of solidification structure and texture development of ferritic stainless steel produced by twin roll strip casting. *Material characterization 60, pp 79-82.*
31. HOU, Z, JIANG. F, and CHENG, G. 2012. Solidification structure and compactness degree of central equiaxed grain zone in continuous casting of billet using cellular automation finite element methods. *ISIJ International, Vol. 52 (2012), No. 7, pp. 1301-1309.*
32. BRIMACOMBE, J.K., HLADY, C.O., KUMAR, S., AND SAMARASEKERA, I.V. 1992. The continuous casting of stainless steels. *Centre for Metallurgical Process Engineering, University of British Columbia, Canada. INFACON 6, Proceedings of the 1st International Chromium Steel and Alloy Congress Cape Town, Volume 2. Johannesburg, SAIMM, 1992. Pp.7-23.*
33. TARSHIS, L.A., WALKER, J.L., AND RUTTER, J.W. 1971. *Metall, Trans, 1971, 2, 2589.*
34. LIN, X., LI, Y., WANG, M., FENG, L., CHEN, J., AND HUANG, W. 2003. Columnar to equiaxed transition during alloy solidification. *Science in CHINA (series E), vol 46, no 5, pp 475-489.*
35. HUNT, J.D. 1984. Steady state columnar to equiaxed growth of dendrites and eutectic. *Materials science and engineering, 65 (1984), pp 75-83.*
36. PORTER. D. A., and EASTERLING. K.E. 1992. Phase transformation in metal and alloys, second edition, London. *Chapman and Hall.*
37. FUKUOKYA, T, KANKI, T., KITTAKA, S., AND MARUKI, Y. 2003, Nippon steel strand electro-magnetic stirrer "S-EMS" for slab caster, *Nippon Steel Technical Report no 87*.
38. KANKI, T., KITTAKA, S., MIURA, Y, AND WATANABE, K. 2002, Nippon steel in-mould electro-magnetic stirrer "M-EMS" for slab caster. *Nippon Steel Technical Report no:86, July 2002*.
39. HUH, M.Y., ENGLER, O., LEE, J.H., PARK, S.H., RAABE, D., AND YOUNG, M. 2005. Effect of through-thickness macro and micro texture gradients on ridging of 17%Cr ferritic stainless steel sheet*, Material Technology-Stainless Steels*.
40. ABB power and productivity for better world.2012. *ABB's strand electromagnetic stirrer for slab casting*, slab SEMS; ensure high quality ferritic stainless steel at Outokumpu Tornio Works.
41. ELANDERS.2008.Slab SEMS, *slab strand electromagnetic stirrer for ferritic stainless and silicon steels*.
42. ANNA, A.K., SIYASIYA, C.W., AND STUMPF, E.W. 2013. Effect of hot working characteristics on texture development in AISI 430 and AISI 433 ferritic stainless steel*. Master of Science degree, Department of Material Science and Metallurgical Engineering, Faculty of Engineering, Built Environment and Information technology, University of Pretoria, Republic of South Africa, November 2013, page 3.*
43. PATRA, S AND SINGHAL, L.K. 2013. Influence of hot band annealing and cold rolling on texture and ridging of 430 stainless steel containing aluminium. *Material sciences and applications, volume 4, pp 70-76.*
44. WATANABE. R. 2006. Possible slip system in body centred cubic iron. *Materials Transactions, Vol. 47, No. 8 (2006), pp 1886-1889.*

45. ZHANG, C., LIU, Z., AND WANG, G. 2011. Effect of hot rolled shear bands on formability and surface ridging of an ultra-purified 21%Cr ferritic stainless steel. *Journal of material processing technology 211 (2011), pp 1051-1059.*
46. HAITO, Y., HONGYUN, B., XIN, L., AND ZHOU, X. 2009. Microstructure, texture and grain boundaries character distribution evolution of ferritic stainless steel during rolling process. *Journal of material processing technology 209(2009) 2627-2631.*
47. HILL, G. 1981. The physical Metallurgy of steel. Material Science and Engineering Series. *London Hemisphere Publishing Corporation.*
48. STUMPF, W.E. 2011. Chapter 5: Static and Dynamic Recrystallization. *Phase transformations in metals and their alloys, page 5.13-1 to page 5.13-16, NFM 700, (2011) University of Pretoria.*
49. ZHANG, C., LIU, Z., AND WANG, G. 2011. Effect of hot rolled shear bands on formability and surface ridging of an ultra-purified 21%Cr ferritic stainless steel. *Journal of material processing technology 211 (2011), pp 1051-1059.*
50. INDACOCHEA, E.J. Work hardening and annealing. University of Illinois at Chicago, pp 1-44.
51. FERRY, M., AND HUNTER, A. 2002.Texture enhancement by inoculation during casting of ferritic stainless steel strip. *Metallurgical and Material Trans A, 2002, 33:1499-507.*
52. RAABE, D. 1994. Texture of the strip cast and hot rolled ferritic and austenitic stainless steels. *Material science, The institute of materials, The Institute of materials, Manuscript received 24 February 1994, final form in 16 May 1994, The institute of Metallkunde and Metallphysik, RWTH Aachen, Aachen Germany.*
53. FERRY, M AND HUNTER, A. 2002. Texture enhancement by inoculation during casting of ferritic stainless steel, M *Metallurgical and material transactions A*, volume 33A, May 2002, pp 1499-1507.
54. LUCKE, K., AND RAABE, D.1993.Texture of ferritic stainless steel. *The Institute of materials, Manuscript received 27 April 1992, final form in 21 August 1993, The institute of Metallkunde and Metallphysik, RWTH Aachen, Aachen Germany.*
55. MARUMA, M.G., SIYASIYA, C.W., AND STUMPF, W.E. 2013.Effect of cold reduction and annealing temperature on texture evolution of AISI 441 ferritic stainless steel. *The journal of Southern African Institute of Mining and Metallurgy volume 113, February 2013*.
56. STUMPF, W.E. 2011. Chapter 5: Static and Dynamic recrystallization. *Phase transformations in metals and their alloys NFM 700 course notes*, University of Pretoria, pp5.1-5.22.
57. BHATTACHARJEE, D., RAY, R.K., AND SAHA, R. 2007. Attaining deep drawability and non-earing properties in Ti+Nb interstitial free steel through double cold rolling and annealing. *India Institute of Technology, Kanpur 208016, India R&D Division, Tata Steel Jamshedpur Jharkhand 831001, India, received 13 December 2006, revised 07 February 2007, accepted 30 March 2007, available 09 May 2007.*
58. SIYASIYA, C.W., MARUMA, G.M., AND STUMPF, W.E. 2015. Influence of chemical composition on the evolution of texture in 441 ferritic stainless steels. *17th international conference on texture of materials (ICOTOM 17), Materials Science and Forum 82(2015) 012040, pp 1-4.*
59. OLIVEIRA, T.R., RAABE, D., SANDIM, H.R.Z., AND SIQUEIRA, R.P. 2011.Composition and orientation effects on the final recrystallization texture of coarse-grained Nb-containing AISI 430 ferritic stainless steels. *Material Science and Engineering A 528 (2011) 3513-3519.*
60. SIQUEIRA. R, SANDIM. H.R.Z, and RAABE. D. 2013. Particle stimulated nucleation in coarse grained ferritic stainless steel. *Metallurgical and Materials transactions A, Volume 44A, January 2013, pp 469-478.*
61. LEWIS, D.B, AND PICKERING, F.B. 1983. Development of recrystallization texture in ferritic stainless steels and their relationship to formability. *Metals Technology, Vol 10, July 1983, pp 264-273.*
62. CHAO, H.C. 1973. Recent studies into mechanism of ridging in FSS. *Metallurgical transaction, Volume 4, April 1973, pp 1183-1186.*

63. CHAO, H.C. 1967. Mechanism of anisotropic lamellar fracture. *Metallurgical transaction, ASM, Volume 60, pp 37-50.*
64. WRIGHT, R.N. 1972. Metallurgical transaction. Volume 3, pp 83-91.
65. ENGLER, O., HUH, M.Y., AND TOME, C. 2005. Crystal-Plasticity analysis of ridging in Ferritic stainless steel sheets. *Metallurgical and Material transaction A, Volume 36 A, November 2005, pp 3127-3139.*
66. KATO, H., NAKAYAMA, T., SUNAMI, T., AND TAKECHI, H. 1967. Mechanism of ridging formation in 17%Cr Ferritic stainless steel sheet. *Transaction journal, Volume 31, pp717-23.*
67. STUMPF, W.E. 2011. Chapter 6: Mechanical property and Microstructure relationship of steels. *Mechanical metallurgy NMM 700 course notes, University of Pretoria, pp 6.1-6.7.*
68. HAMADA. J.I., INOUE. H., AND ONO. N. 2011. Effect of texture on R-value of ferritic stainless steel sheets. *Steel Research Laboratories, Nippon Steel Corporation, 20-1 Shintomi, Futsu, Chiba, 293-8511, Japan, Department of Material Science, Graduate School of Engineering, Osaka Prefecture University, 1-1 Gakuen-Cho, Naka-ku, Sakai, Osaka, 599-8531, Japan.*
69. HOLSCHER. M., KRUPP. S.A., AND STAUBWASSER. L. 1994. Influence of hot band annealing on texture and formability of cold rolled X6Cr17 ferritic stainless steel. *Processes and Materials Innovation in stainless steel products, volume 12 (2) (1994), pp 48-54.*
70. LEACH, K.R. 2014. The measurement of surface texture using stylus instruments. *National physical laboratory (NPL), issue no 2, July 2001, Updated February 2014*.
71. LEE, D.N., PARK, S.H. AND SHIN, H.J. 2003. The effect of texture on ridging of ferritic stainless steel. *Acta-materiala 51 (2003) 4693-4706.*
72. BELYAKOV, A., KAIBYSHEV, R. AND SAKAI, T. 1998. New grain formation during warm deformation of ferritic stainless steel. *Metallurgical and Materials transaction A, Volume 29A, January 1998, pp 161-167.*
73. HAMADA, J., MATSUMOTO, Y, FUDANODEF, AND MAEDA, S. 2003. Effect of initial solidification on ridging phenomenon and texture in type 430 ferritic stainless steel sheets. *ISIJ International, Vol 43, no 12,pp 1989-1998.*
74. LIU, Z., WANG, G., AND ZHANG, C. 2011. Effects of hot rolled shear bands on formability and surface ridging of ultra-purified 21%Cr ferritic stainless steel. *Journal of Material Processing Technology 211 (2011) 1051-1059*.
75. SHIN. H.J, AN. J.K, PARK. S.H, AND LEE. D.N. 2003. The effect of texture on ridging of ferritic stainless steel. *Acta Materialia 51, pp 4693-4706.*
76. RAY, R.K., AND SAHA, R. 2007. Evolution of microstructure, texture and grain boundary character in severely cold rolled Ti+Nb IF steel. *Department of Material Science and Metallurgical Engineering, India, Institute of Technology, Kanpur 208016, India.*
77. HUTCHININSON, W.B., 1984. Development and annealing texture in low carbon steels. *International metals reviews, Vol. 29, No. 1, pp 25-41*
78. LI, S., ZHANG, X., AND CHEN, Z. 1996. Strain-dependence of plastic strain ratio of deep-drawability aluminium killed steel sheet. *Department of material science and engineering, Central South University of technology. Changsha 410083, Vol 6 no 1.*
79. MOLA. J, JUNG. I, PARK. J CHAE, AND DE COOMAN. B. 2012. Ridging control in transformable ferritic stainless steels. *Metallurgical and material transactions A, vol 43A, pp 228-244.*
80. SINGH, C.D. 1996. Effect of annealing on hot band texture of ferritic stainless steel. *Research and development centre for Iron and steel, Steel Authority of India limited Ranchi-83402, India.*
81. TSUJI. N, TSUZAKI. K, AND MAKI. T. 1992 Effect of initial orientation on the cold rolling behaviour of solidified columnar crystals in a 19% Cr Ferritic Stainless Steel. *ISIJ International, Vol. 32 (1992), No.12, ppn1319-1328.*
82. NAFISI. S, ARAFIN. M.A, COLLINS. L, AND SZPUNAR. J. 2012. Texture and mechanical properties of API X100 steel manufactured under various thermos-mechanical cycles. *Material Science and Engineering A 531 (2012), pp 2-11.*

83. ZONG. C, ZHU. G AND MAO. W. 2013. Effect of crystallographic texture on anisotropy of yield strength in API X 100 pipeline steel. *Journal of Iron and Steel research, international 2013, 20(8), pp 66-71.*

Appendix A: XRD - ODFs of rolling and recrystallisation texture

1.1. Roughing hot rolling texture

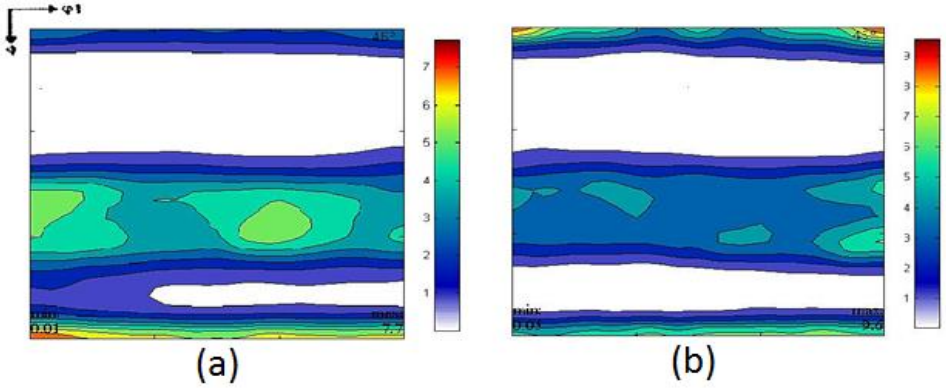

Figure 1.1A: Bunge ODF $\varphi_2 = 45°$ section at near surface-layer in the RD-TD plane after roughing hot rolling (a) IECS and (b) ICCS.

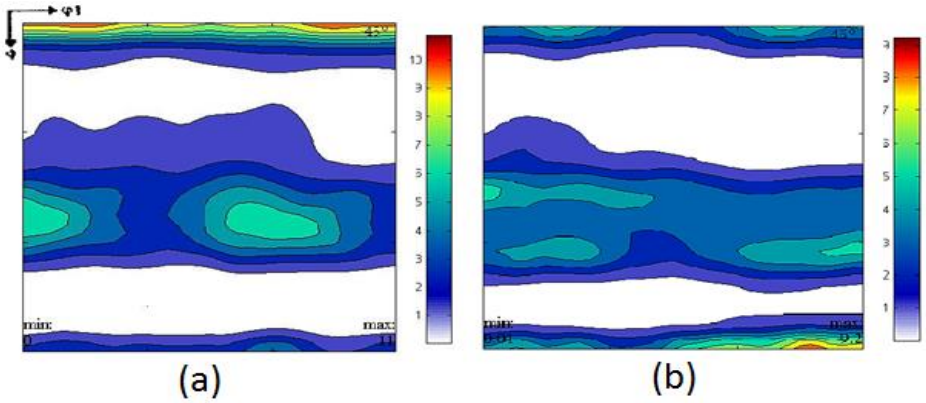

Figure 1.2A: Bunge ODF $\varphi_2 = 45°$ section at mid-layer in the RD-TD plane after roughing hot rolling (a) IECS and (b) ICCS.

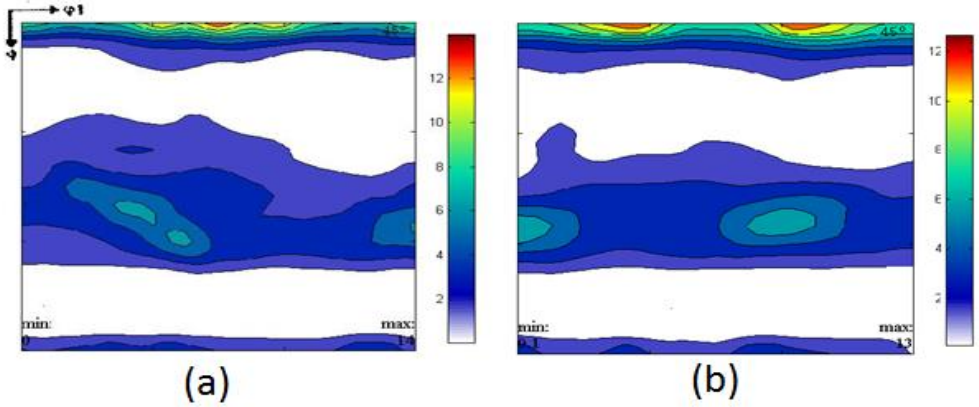

Figure 1.3A: Bunge ODF $\varphi_2 = 45°$ section at near centre-layer in the RD-TD plane after roughing hot rolling (a) IECS and (b) ICCS.

1.2. Steckel hot rolling texture

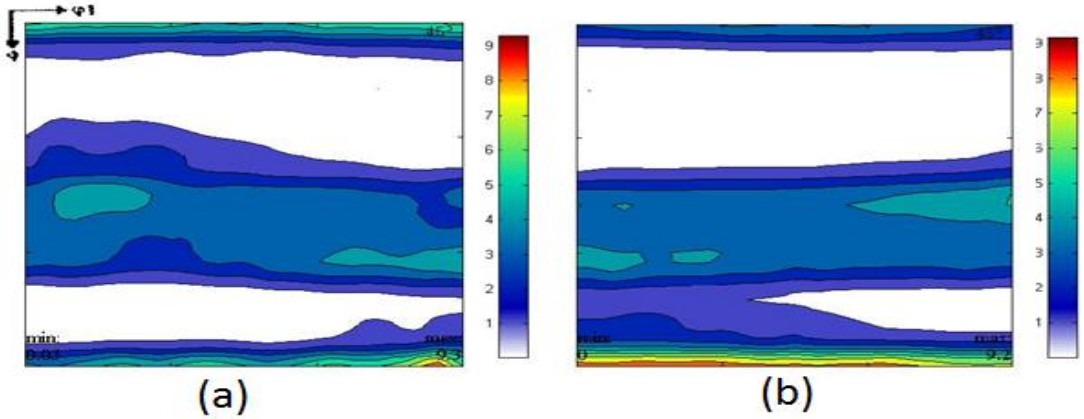

Figure 1.4A: Bunge ODF $\varphi_2 = 45°$ section at near surface-layer in the RD-TD plane after finish hot rolling (a) IECS and (b) ICCS.

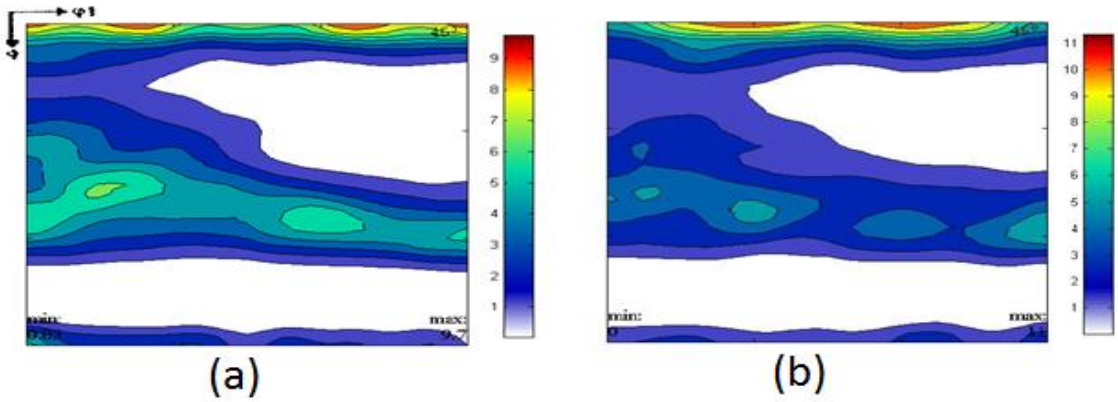

Figure 1.5A: Bunge ODF $\varphi_2 = 45°$ section at near centre-layer in the RD-TD plane after finish hot rolling (a) IECS and (b) ICCS.

1.3. Intermediate annealing texture (HBA texture)

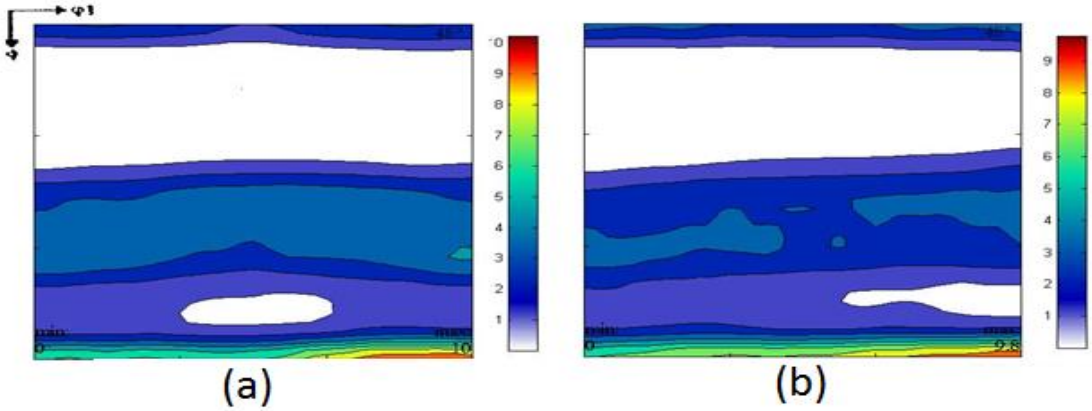

Figure 1.6A: Bunge ODF $\varphi_2 = 45°$ section at near surface-layer in the RD-TD plane after annealing of hot bands (a) IECS and (b) ICCS.

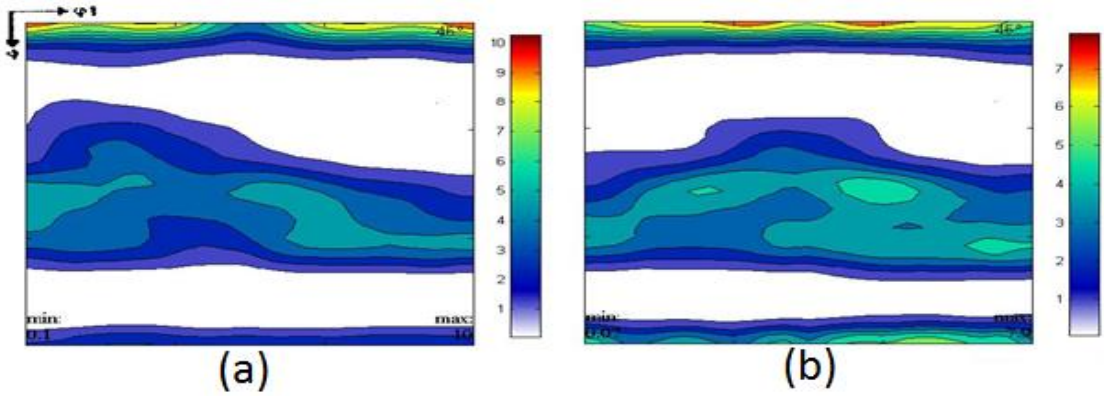

Figure 1.7A: Bunge ODF $\varphi_2 = 45°$ section at centre-layer in the RD-TD plane after finish hot rolling (a) IECS and (b) ICCS.

1.4. Cold rolling texture of Steckel strips (HB-CR texture)

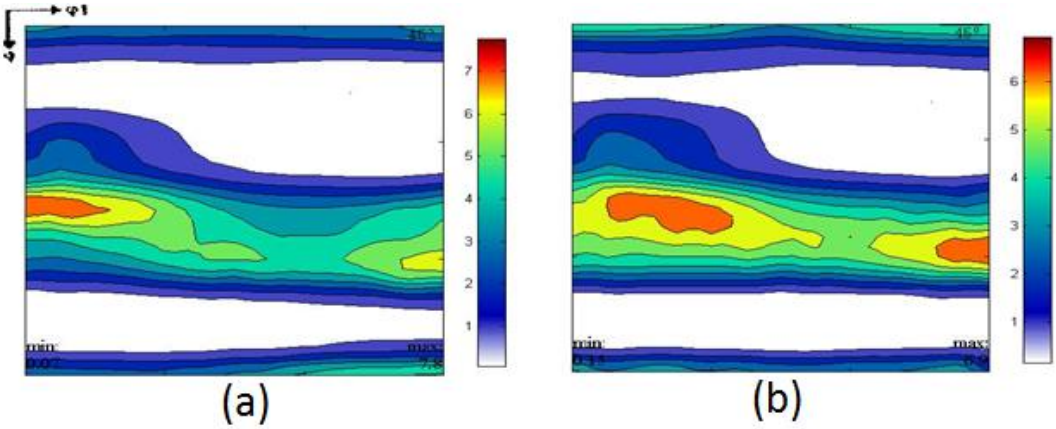

Figure 1.8A: Bunge ODF $\varphi_2 = 45°$ section at near center layer in the RD-TD plane after cold rolling of hot bands (a) IECS and (b) ICCS.

1.5. Cold rolling texture of HBA strips (HBA-CR texture)

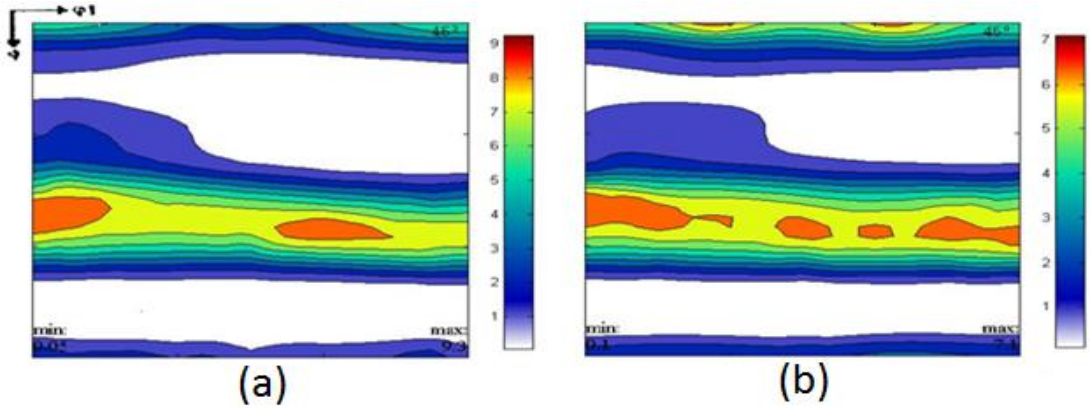

Figure 1.9A: Bunge ODF $\varphi_2 = 45°$ section at near center layer in the RD-TD plane after cold rolling of annealed hot bands (a) IECS and (b) ICCS.

1.6. Annealing of HB-CR texture (HB-CRA texture)

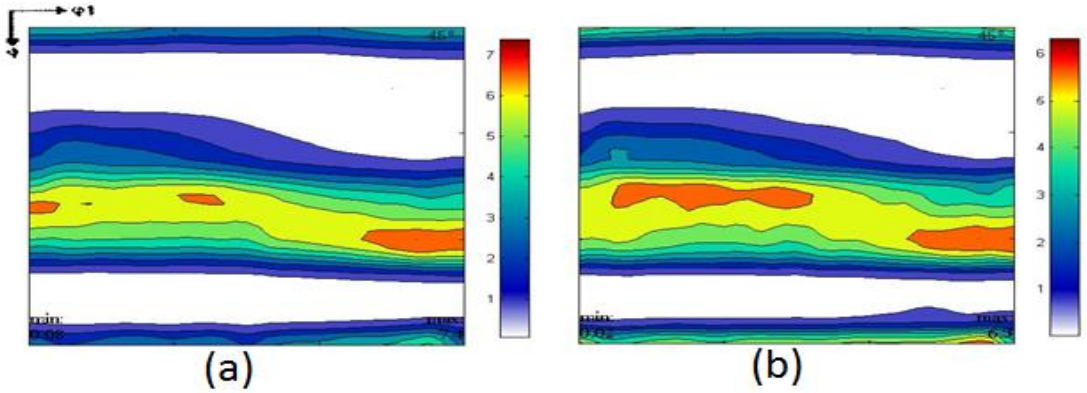

Figure 1.10A: Bunge ODF $\varphi_2 = 45°$ section at near center-layer in the RD-TD plane after annealing of HB-CR bands (a) IECS and (b) ICCS.

1.7. Annealing of HBA-CR texture (HBA-CRA texture)

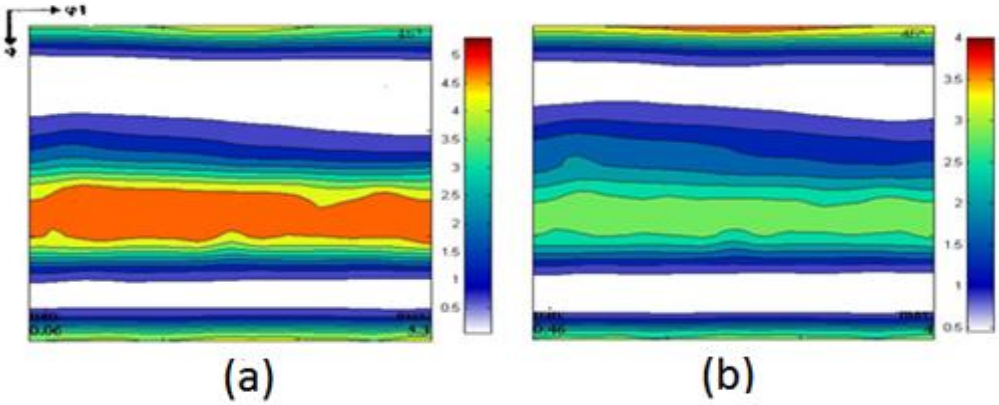

Figure 1.11A: Bunge ODF $\varphi_2 = 45°$ section at near center-layer in the RD-TD plane after cold rolling of annealed hot bands (a) IECS and (b) ICCS.

Appendix B: SEM-EBSD ODFs of rolling and recrystallisation texture

2.1. Roughing hot rolling texture

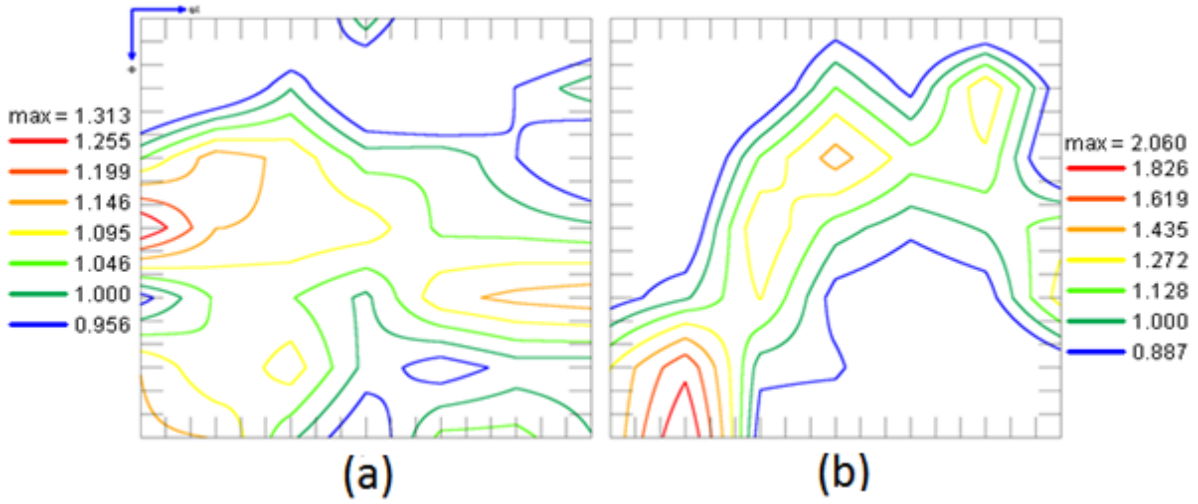

Figure 2.1B: SEM-EBSD Bunge ODFs $\varphi_2 = 45°$ section at near surface-layer in the RD-TD plane where s_1 = 8.38 mm (near surface layer) after roughing hot rolling (a) IECS and (b) ICCS.

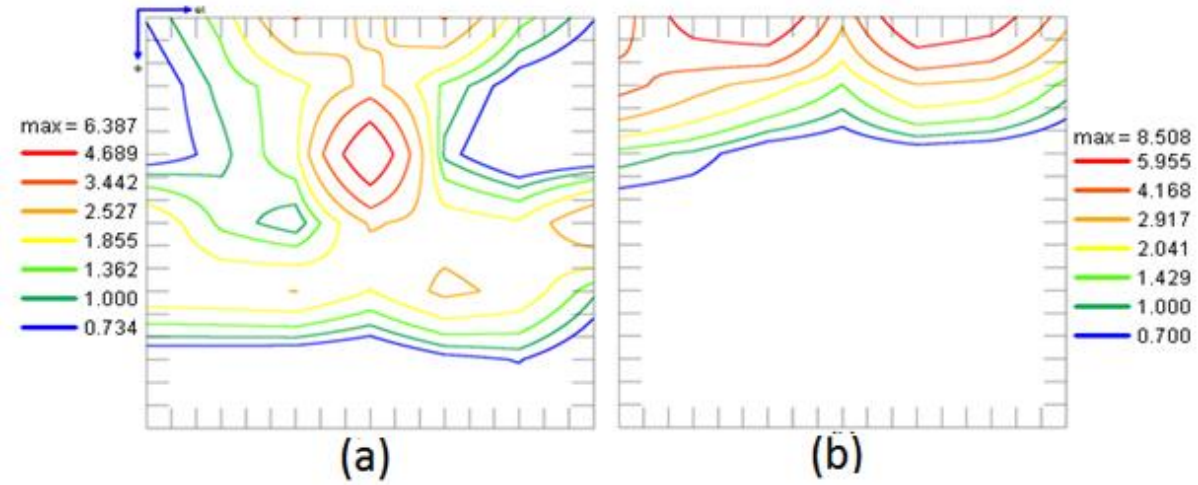

Figure 2.2B: SEM-EBSD Bunge ODFs $\varphi_2 = 45°$ section at mid -layer in the RD-TD plane where s_2 = 6.45 mm (mid-surface layer) after roughing hot rolling (a) IECS and (b) ICCS.

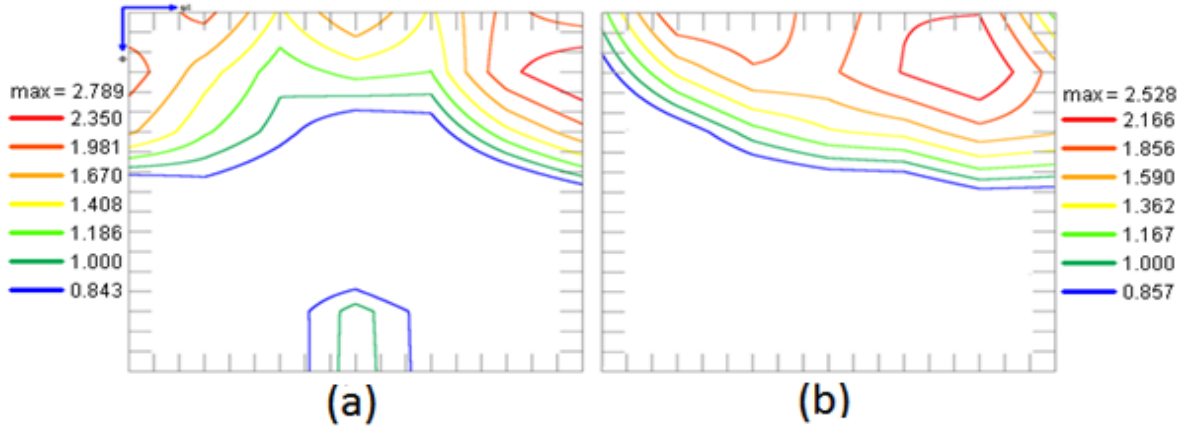

Figure 2.3B: SEM-EBSD Bunge ODFs $\varphi_2 = 45°$ section at near center layer in the RD-TD plane where s_3 = 4.20 mm (centre layer) after roughing hot rolling (a) IECS and (b) ICCS.

2.2. Steckel hot rolling (HB) texture

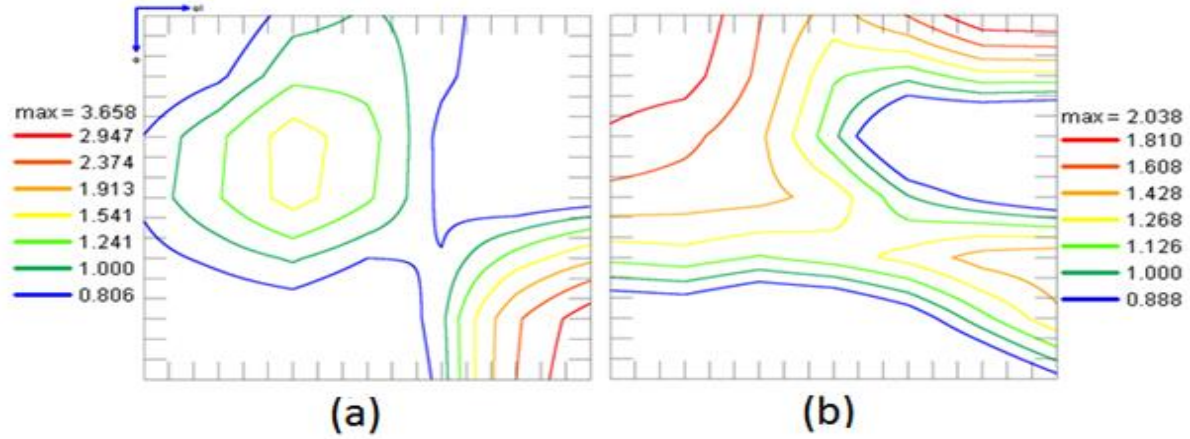

Figure 2.4B: SEM-EBSD Bunge ODFs $\varphi_2 = 45°$ section at near surface-layer in the RD-TD plane where s_1 = 3.90 mm (near surface layer) after finish hot rolling (a) IECS and (b) ICCS.

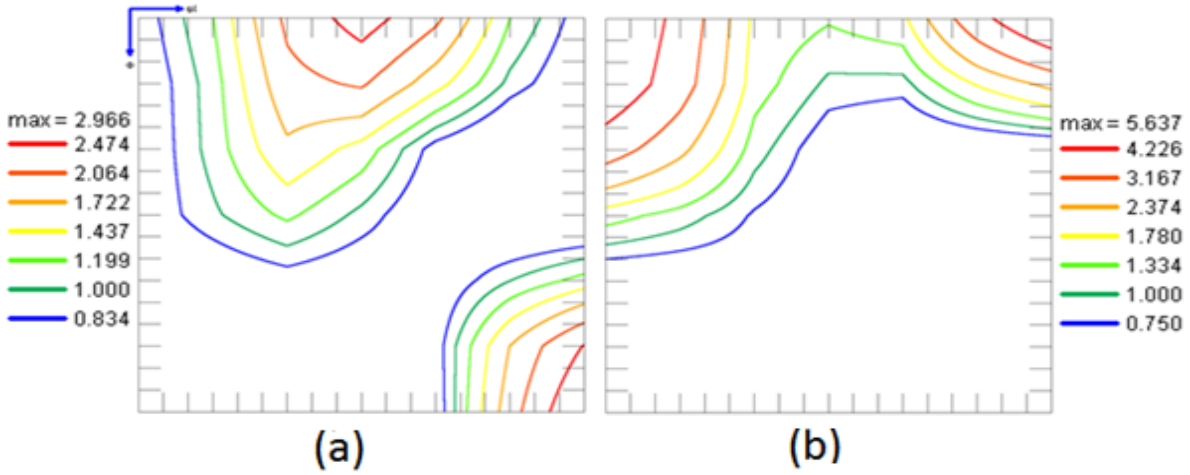

Figure 2.5B: SEM-EBSD Bunge ODFs $\varphi_2 = 45°$ section at near center-layer in the RD-TD plane where s_2 = 1.98 mm (centre layer) after finish hot rolling (a) IECS and (b) ICCS.

2.3. Intermediate annealing texture (HBA texture)

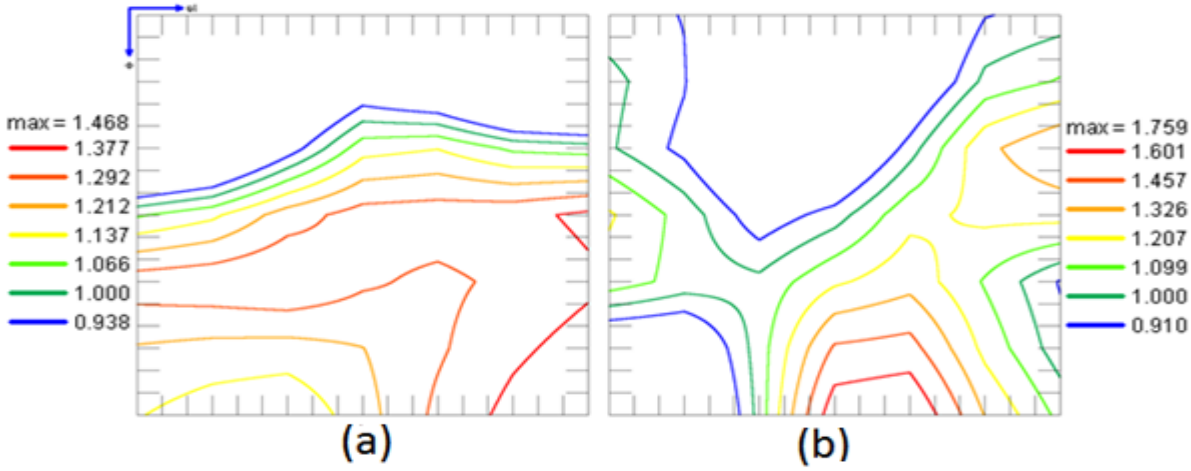

Figure 2.6B: SEM-EBSD Bunge ODFs $\varphi_2 = 45°$ section at near surface-layer in the RD-TD plane where s_1 = 3.90 mm (near surface layer) after intermediate annealing of finish hot rolling (a) IECS and (b) ICCS.

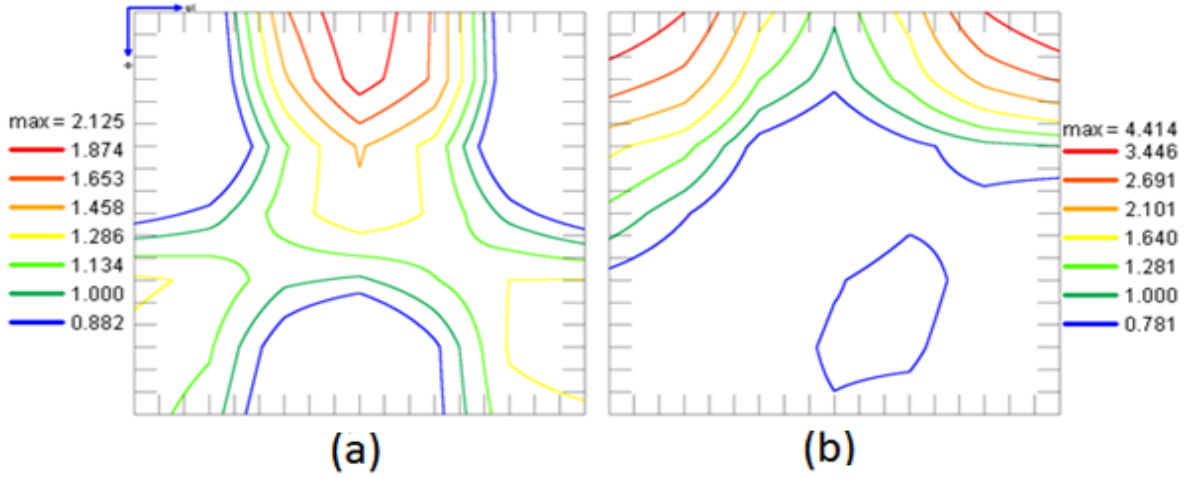

Figure 2.7B: SEM-EBSD Bunge ODFs $\varphi_2 = 45°$ section at near center-layer in the RD-TD plane where s_3 = 1.98 mm (centre layer) after intermediate annealing of finish hot rolling (a) IECS and (b) ICCS.

2.4. Cold rolling texture of HB strips (HB-CR texture)

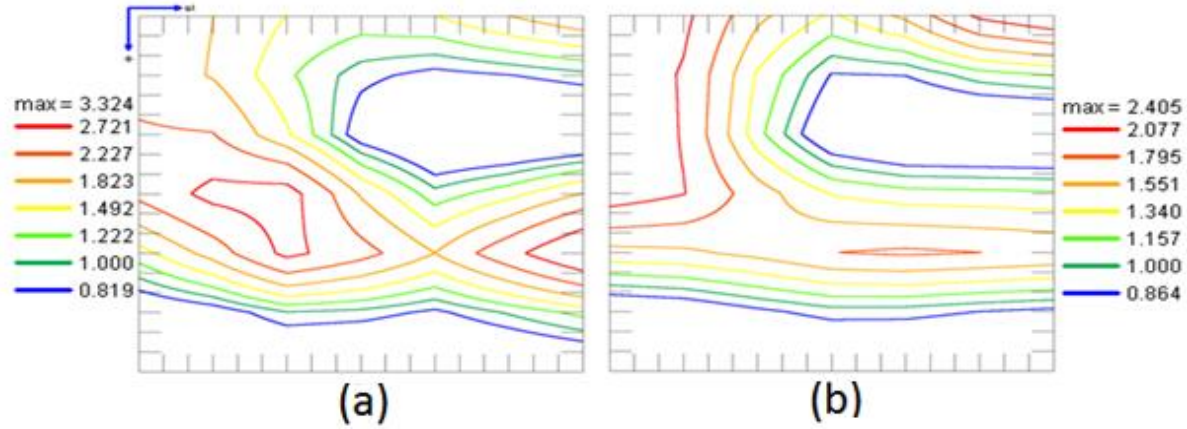

Figure 2.8B: SEM-EBSD Bunge ODFs $\varphi_2 = 45°$ section at near center-layer in the RD-TD plane where s_3 = 1.13 mm (near center layer) after cold rolling of hot band (a) IECS and (b) ICCS.

2.5. Cold rolling texture of HBA strips (HBA-CR texture)

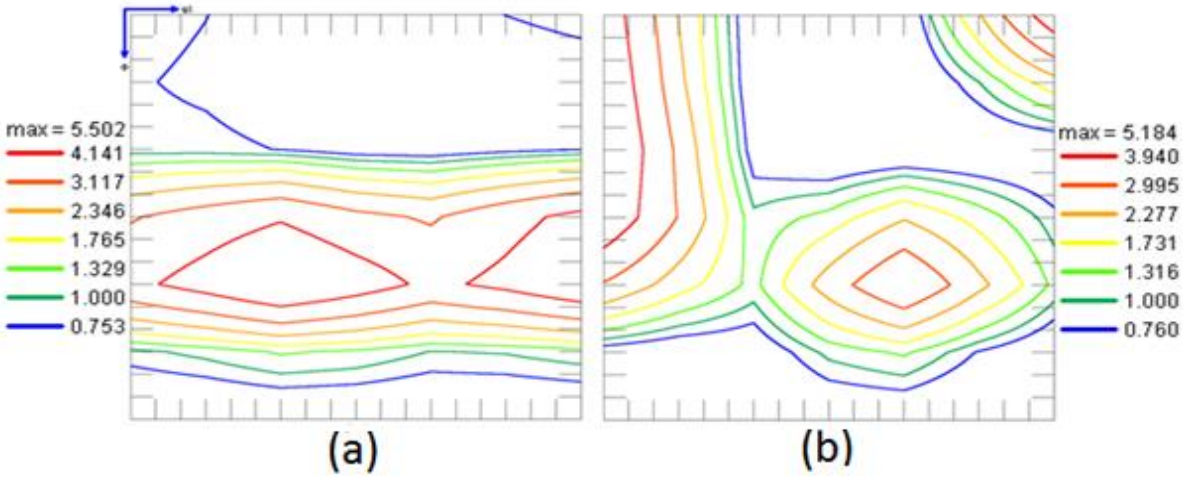

Figure 2.9B: SEM-EBSD Bunge ODFs $\varphi_2 = 45°$ section at near center-layer in the RD-TD plane where s_3 = 1.13 mm (near center layer) after cold rolling of HBA (a) IECS and (b) ICCS.

2.6. Annealing of HB-CR texture (HB-CRA texture)

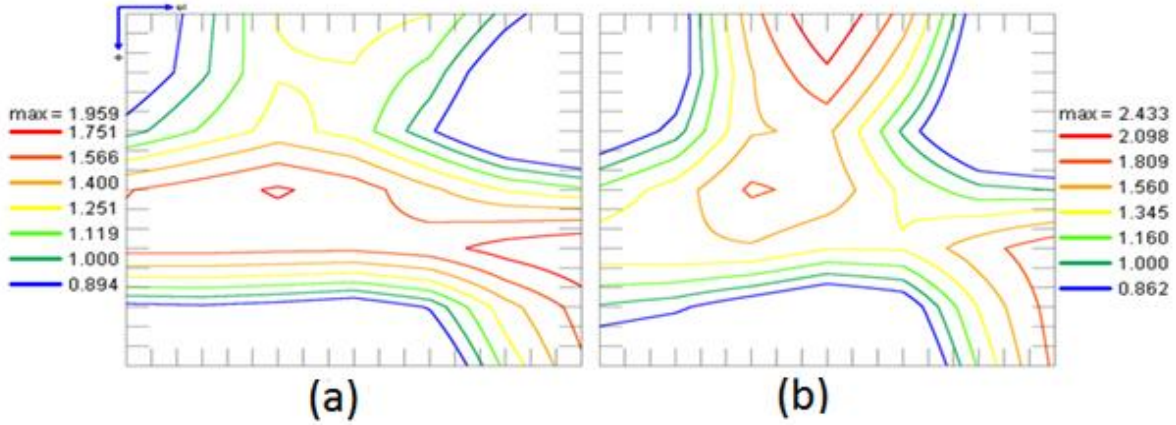

Figure 2.10B: SEM-EBSD Bunge ODFs $\varphi_2 = 45°$ section at near center-layer in the RD-TD plane where s_3 = 1.13 mm (near center layer) after annealing of HB-CR (a) IECS and (b) ICCS.

2.7. Annealing of HBA-CR texture (HBA-CRA texture)

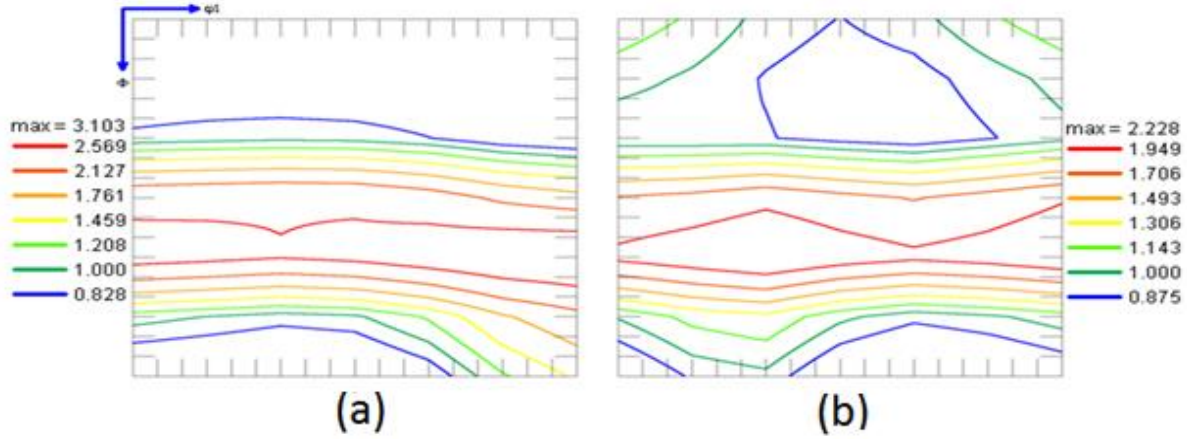

Figure 2.12B: SEM-EBSD Bunge ODFs $\varphi_2 = 45°$ section at near center-layer in the RD-TD plane where s_3 = 1.13 mm (near center layer) after annealing of HBA-CR (a) IECS and (b) ICCS.